MEASUREMENT OF DRAG TORQUE, LIFT OFF SPEED, AND IDENTIFICATION OF FREQUENCY DEPENDENT STIFFNESS AND DAMPING COEFFICIENTS OF A SHIMMED BUMP-TYPE FOIL BEARING

A Thesis

by

JOSHUA DAVID NORSWORTHY

Submitted to the Office of Graduate Studies and Professional Studies of
Texas A&M University
in partial fulfillment of the requirements for the degree of

MASTER OF SCIENCE

Chair of Committee,	Luis San Andrés
Committee Members,	Dara Childs
	Luciana Barroso
Head of Department,	Alan. Pallazollo

December 2014

Major Subject: Mechanical Engineering

ABSTRACT

This thesis presents measurements characterizing the static and dynamic performance of a BFB configured with shims of two thicknesses (30 μm and 50 μm). Parameters of interest include drag torque, rotor lift off speed, and the estimation of force coefficients of a BFB with shims (30 μm and 50 μm thick). The thesis also compares those results to those of the original BFB (without shims).

Drag torque measurements during shaft acceleration tests up to 50 krpm show that the lift off speed of both the original bearing and the shimmed bearing increases linearly with applied unit load ($W/(LD)$). The bearing startup friction factor $f=T/(RW)$ during dry sliding condition for the original bearing (f~0.3) is constant with applied load ($W/(LD)$), while the bearing in shimmed configurations show a larger friction factor that decreases with load ($W/(LD)$). Once airborne, a bearing in all three configurations (shimmed and not shimmed) show a similar low (f~0.05 at $W/(LD)$~ 20 kPa) friction factor that decreases with increasing load.

Bearing dynamic force coefficients are estimated over a frequency range of 200-450 Hz, under a specific load ~14.3 kPa. The shims have an unremarkable effect on the foil bearing direct stiffness coefficients. The shimmed BFB shows increased direct damping coefficients (in particular along the static load direction and at high frequencies) while operating at 50 krpm. The energy dissipated is best characterized with a structural loss factor γ, a function of the bearing elastic (K) properties, and the sliding friction characteristics. Over the narrow arbitrary frequency range from 300-400 Hz and for dynamic motions of amplitude of 20 μm, the bearing without shims offers a $\bar{\gamma}$ 25% larger than the original bearing, demonstrating that the shimmed bearing dissipates more mechanical energy, albeit the standard deviation in the average loss factor of the shimmed bearings is much larger.

Measurements of the turbocharger (TC) shaft vibration conducted as the shaft accelerates toward 50 krpm (833 Hz) show that a shimmed BFB reduced subsynchronous whirl motions of the TC shaft apparent with the original BFB (WFR~0.30). When

supported on a BFB with 50 μm shims, the TC shaft operates free of subsynchronous whirl motions.

Shimming, therefore is a simple, economical way of increasing energy dissipation in BFBs thereby improving their rotordynamic performance. Alas shimming also offers some undesirable characteristics such as higher startup torque requirements. Note however, that once airborne, the drag friction factor of a shimmed BFB is similar to that of the original bearing.

ACKNOWLEDGEMENTS

I thank Dr. Luis San Andrés, my committee chair and advisor, for accepting me into the Tribology Group at Texas A&M University Turbomachinery Laboratory. I am truly grateful for his guidance and support, as well as for his prompt response and numerous revisions of my graduate work output (reports and thesis).

I thank Dr. Dara Childs for his valuable comments, and Dr. Luciana Barroso for reviewing my graduate work and serving on my thesis committee.

I acknowledge the Turbomachinery Research Consortium at Texas A&M University for their interest and financial support.

Thanks to the staff of the Turbomachinery Laboratory for their technical assistance and advice. Finally, I thank the graduate students of the Turbomachinery Laboratory, and in particular Travis Cable and Jennifer Gaines, for their encouragement, camaraderie and friendship.

NOMENCLATURE

$a_{\underline{X}(t)}, a_{\underline{Y}(t)}$	Bearing accelerations along $\underline{X}$ and $\underline{Y}$ directions [m/s^2]
$\bar{A}_{\underline{X}(\omega)}, \bar{A}_{\underline{Y}(\omega)}$	DFT of $\underline{X}$ and $\underline{Y}$ bearing accelerations [m/s^2]
$C_{\alpha\beta}$	Equivalent viscous damping coefficients; $\alpha, \beta = X, Y$ [Ns/m]
c_{nom}	Nominal radial clearance [m]
D	Top foil (bearing) diameter, D=2xR[m]
D_A	Inner diameter of the assembled bearing [mm]
D_o	Bearing cartridge outer diameter [mm]
D_I	Bearing cartridge inner diameter [mm]
D_s	Shaft outer diameter [mm]
E	Top foil elastic modulus [Pa] or [N/ m^2]
f	*T/(RW).* Bearing sliding (drag) friction factor [-]
F_i^j , $i,j=\underline{X},\underline{Y}$	DFT amplitdues of the excitation forces [N]
F_o	Excitation force at the lowest excitation frequency [N/s]
F_s	Applied static load [N]
ΔF	Time rate of change in the excitation force [N]
$\{H_{\alpha\beta}\}_{\alpha\beta=X,Y}$	$K_{\alpha\beta}+j\omega\, C_{\alpha\beta}$. Bearing impedances [N/m]
h	Gas film thickness [m]
i	Imaginary unit, $\sqrt{-1}$
$\{K_{S\beta}\}_{\beta=\underline{X},\underline{Y}}$	Squirrel cage stiffness coefficients [N/m]
$K_{\alpha\beta}$	Stiffness coefficients; $\alpha, \beta = X, Y$ [N/m]
L	Bearing axial width [mm]
L_T	Torque lever arm [mm]
M_B	Mass of the bearing [kg]
M_s	Estimated system mass (Bearing + squirrel cage) [kg]
N_B	Number of bumps [-]

P	Hydrodynamic pressure in gas film [Pa]
P_a	Ambient pressure [Pa]
P_r	Contact pressure [Pa]
R	Rotor radius [m]
r_g	Expansion in the shaft due to centrifugal forces [m]
T	$\delta K_s L$. Drag torque [Nmm],
$T_{\text{breakaway}}$	Breakaway drag torque [Nmm]
t	Time [s]
t_t	Top (thin) foil thickness [m]
W	F_s-W_B. Net static load [N]
W_B	Bearing weight [N]
X,Y and $\underline{X}$,$\underline{Y}$	Coordinate system for the inertial axes [m]
x', y'	Bearing displacements relative to the journal [m]
$\bar{x}'_{(\omega)}, \bar{y}'_{(\omega)}$	DFT of bearing $\underline{X}$,$\underline{Y}$ displacements relative to the journal [m]
σ	Standard deviation
γ	$\omega(C_{XX}+ C_{YY})/K_{XX}+ K_{YY.}$ Bearing loss factor [-]
$\bar{\gamma}$	Frequency averaged loss factor [-]
θ	Top foil angular coordinate [rad]
θ_p	Angular distance between shims [rad]
μ	Gas viscosity [Pa-s]
υ	Poisson's ratio [-]
τ	Shear stress [N/m^2]
φ	Angle of rotation from X to $\underline{X}$ axes
Ω	Rotor speed [krpm]
ω	Excitation frequency [rad/s]

ACRONYMS

ACM	Air Cycle Machine
DFT	Discrete Fourier Transform Operator
EOM	Equation of Motion

ACM	Air cycle machine
BFB	Bump type gas foil bearing
RBS	Rotor-bearing system
ROT	Rule of Thumb
TC	Turbocharger
TS	Torque screwdriver

TABLE OF CONTENTS

Page

LIST OF FIGURES

Page

LIST OF TABLES

Page

CHAPTER I

INTRODUCTION

Gas foil bearings (GFBs), in particular bump type foil bearings, provide reliable, low friction support to high-speed micro turbomachinery (<400 kW) [1]. Figure 1 presents a schematic view of a typical bump type foil bearing (BFB) comprised of one or more bump foil strip layers, a top foil, and a bearing cartridge. A spinning rotor pulls gas by viscous shearing into the wedge formed by the rotor outer diameter and the bearing inner surface thus generating a hydrodynamic pressure field that lifts the rotor from contact with the bearing. The thin gas film prevents wear on the rotor and inherently offers lower drag power than oil lubricated bearings due to the low viscosity of the working gas. The load support is due to reaction forces provided by the gas film and are transmitted to the bump foil structure. Adequate mechanical energy dissipation, arising from the dry friction from the relative motion of the bump foil strip with both the top foil and the bearing cartridge, is critical for the stable operation of a rotor-bearing system (RBS).

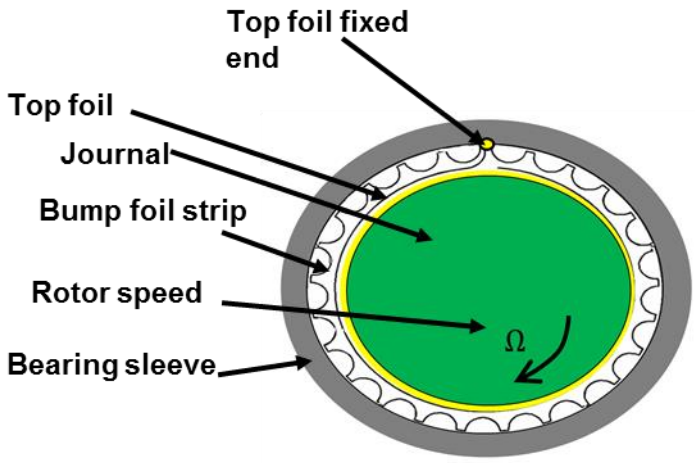

Figure 1. Schematic representation of a first generation bump-type foil bearing.

BFBs typically come in three variations termed generation I, II, and III bearings[1]. Chen *et al*. [2] and DellaCorte *et al.* [3] detail the manufacturing procedures for the construction of the bump foil strip and top foil of generation I and II BFBs The simplest BFB, a generation I type, contains a single bump foil strip as depicted in Figure 1. A generation II bearing contains various separate bump foil strips that line around the bearing inner surface. Multiple bump foil strips create axially and circumferentially varying stiffness and damping characteristics. Generation III GFBs include complex arrangements of multiple bump foil strips along and around the bearing inner surface to further tailor the bearing stiffness and damping characteristics[2].

BFBs are applied routinely in aircraft Air Cycle Machines (ACMs). In a more recent laboratory setting, gas foil bearings have proven reliable support elements for automotive turbochargers [4,5]. Low drag power loss, tolerance to misalignment, and reliable high temperature operation are advantages that GFBs offer to microturbomachinery [1]. However, rotors supported on BFBs are known to display large subharmonic motions [6].

The stiffness and damping coefficients of the elastic bump foil strips largely determine the rotordynamic performance and stability of a rotor supported on gas bearings. As shown in Refs.[4,6]; mechanical preload, through the placement of metal shim strips axially along the interior of the bearing, effectively increases the onset rotor speed of instability and decreases the magnitude of subsynchronous vibrations in BFB supported rotors. Shimming is a simple and low cost technique.

The present work will advance prior research by characterizing the performance of shimmed BFBs through the identification of rotor lift off and shut down events as well as the identification of frequency dependent force coefficients while airborne (with journal rotation).

---

[1] The design of generation III BFBs is patented, and in many situations, remains proprietary information.

[2] Gas lubricant leaking from the edges of the bearing reduces the hydrodynamic pressure leading to a lower load capacity and bearing stiffness [1]. Modifying the bump foil structure allows the bearing design to maintain an adequate minimum film thickness throughout its operation, while minimizing gas leakage from the edges of the bearing, thereby improving the bearing stiffness and load capacity [1]

Literature review

Background

Designers and manufactures of advanced turbomachinery seek operation at increasingly higher speeds, with lighter and more compact units with increased reliability (fewer moving parts), thus making gas film lubrication preferable over traditional oil lubrication. The low viscosity of a gas inherently reduces the load capacity of gas lubricated bearings when compared to oil lubricated bearings. However, the advantage of eliminating an oil supply system and the ensuing lower drag power losses make gas bearings a desirable alternative in lightly load turbomachinery [1].

Block and Van Rossum [7] introduced the first compliant surface (foil) bearing in 1953. Note that the first foil bearing does not contain an elastic "bump" undestructure; it simply contains a top foil. The bearing compliance aided in solving issues related to high temperature and high speed operation by tolerating thermal and centrifugal expansion of a rotor. By tolerating misalignment and allowing larger film thicknesses, the compliant support also offered an improved load capacity and reliability over that of a fixed arc bearing.

The static and dynamic forced performance of BFBs encompasses the bearing load capacity, drag torque, rotor lift off speed, as well as the force coefficients (stiffness and damping); all of which are affected by the physical properties and geometry of the bump foil complaint understructure. The bump foil strip, usually a corrugated plate, is idealized as discrete elastic spring elements. The analysis of GFBs is complicated due to the interaction between the fluid film, and the deformation of the compliant foils (solid mechanics), plus the complex nature of dry friction systems. Currently, computational models of GFBs are capable of reliable and accurate predictions; however, the actual implementation of GFB is limited and relies upon extensive trials.

A critical review of the recent experimental work seeking to characterize and predict the performance of gas foil bearing (GFB) technology follows. The first section reviews the literature that pertains to the effects of environmental conditions (pressure, temperature, lubricant density, etc.) on BFB load capacity. The second section details

literature pertaining to foil bearing rotordynamic force coefficients (with and without journal speed). The third section discusses the literature pertaining to transient rotor start up events, i.e., drag torque and lift off and shut down events. Finally, the fourth section details the performance characteristics of rotors supported on gas foil bearings.

The load capacity of bump foil bearings

The structural properties of the spring structure greatly affect the BFB static and dynamic forced performance. Parameters affecting the bearing load capacity include the bump foil geometry and materials, as well as the environment temperature and pressure.

In 1982 Heshmat *et al*. [8] showed that the bump foil of a BFB can be tailored to enhance its load capacity and rotordynamic stability. The bump foil strip layer of a generation I foil bearing is split into multiple strips axially that stretch circumferentially, effectively turning a generation I bearing into a generation II bearing. The bearing top foil is also sputter coated with a thin layer of copper and then heat treated. Splitting the bump foil strip layer allows for axially varying stiffness characteristics while coating the bearing with copper increases the damping properties. The generation II bearing shows a 60% increase in load capacity over an uncoated bearing.

In 1994 Heshmat [9] measured the load capacity and static load-deflection behavior of a generation II bearing (L=31mm, D=35mm). The static load versus deflection behavior is highly nonlinear with hysteresis loops evidencing mechanical energy dissipation. Alas, the dissipated mechanical energy is not quantified. The author reports that the bearing with an axially varying stiffness (generation II) can support a load of 727 N (673 kPa specific load) at a rotor speed of 132 krpm, which is a two-fold improvement over generation I bearings. The introduction of axially and circumferentially varying stiffness characteristics marks a dramatic step in the evolution of BFBs.

Environmental conditions, such as temperature and pressure, affect the physical properties of a bump foil strip and the top foil. Also note that temperature and pressure also alter the density and viscosity of the gas lubricant. Bruckner and Puleo [10] investigate the effects of temperature and pressure on the load capacity of a 35 mm

diameter by 27 mm length generation III foil bearing. The test pressure range is 0.1- 2.5 atm and the temperature increases up to 500°C. Note that the bearing inner surface is uncoated however the shaft surface has a proprietary coating. The bearing load capacity is found to increase with increasing gas pressure, and to decrease with an increasing gas temperature. Note that an increase in temperature causes an increase in the gas lubricant viscosity. Since the hydrodynamic gas film pressure is proportional to lubricant viscosity, the bearing load capacity should increase with temperature.

The observed behavior of the load capacity with respect to increasing temperature reported in Ref.[10] is attributed to a softening effect observed in the bump foil layer at high (~500°C) temperatures. Below 0.5 atm (a mild vacuum) the load capacity drops steeply, indicating a "starved" gas bearing, i.e., when the lubricant density is too low (too few gas molecules) for the bearing to support a load. Ref. [10] demonstrates that GFBs fail to provide adequate load support when operating at pressures below ambient.

In an effort to encourage the implementation of gas foil bearings, DellaCorte [11] presents a "Rule of Thumb" (ROT) for the prediction of BFB load capacity. The ROT, $W=D_o\,(L \text{ x } D)(\,D \text{ x } \Omega)$, relates the bearing load capacity (W) to the bearing projected area (L x D), and (two times) the surface velocity (D x Ω). D_o is an experimentally determined load capacity coefficient. For example a generation III bearing has a load capacity coefficient (D_o) four times larger than that of a similarly sized generation I BFB operating at the same shaft speed. The ROT is based on extensive empirical evidence from many types of BFBs (generations I, II, and III), as well as multileaf type gas journal bearings. However, the ROT is over ten years old, and ignores critical bearing operating conditions including the environmental pressure, and temperature.

Despite the advances and steady improvements in static load capacity, BFBs still remain a highly specialized technology with few applications. As designers of advanced turbomachinery seek to support larger loads at higher shaft speeds, some of the characteristics of foil bearings present challenges. Each bump foil bearing is highly engineered, not a ready off the shelf item, and leads to scalability issues. DellaCorte and Bruckner [12] discuss the current state of the art and future challenges for oil free

turbomachinery. While the operating minimum film thickness increases with rotor speed and decreases with applied load, the authors argue about practical upper and lower bounds to the film thickness. The viscous drag power loss in BFBs is dissipated as heat; a fraction is carried by the gas film, and the rest is conducted into to the rotor and top foil. The bearing top foil, being thin, is susceptible to thermal distortions brought on by increasing the shaft speed and static load, thus eventually causing rubbing. This is the lower bound of the film thickness, i.e., the smallest film thickness that is maintained for operation without contact, at a given speed and load.

Remarkably, there exists an upper limit to the film thickness or a maximum film thickness. Recall that a minimum film thickness is needed to lift the rotor. DellaCorte and Bruckner [12] note a maximum film thickness as that above which the gas lubricant leaks from the bearing edges, effectively reducing the hydrodynamic pressure that keeps the rotor afloat. DellaCorte and Bruckner [12] report experimental results for a generation I BFB identifying the upper and lower bounds to the film thickness in as 25 μm and 5μm, respectively.

According to the DellaCorte's ROT for bearing load capacity [11], gas foil bearings can support business jet class turbofan engines and (with increases in bearing diameter) large size compressors (with rotors weighing ~ 2400-9800N). The author notes that the load capacity does not truly limit the implementation of gas foil bearing technology. The authors suggest the limiting factors for the scaling of gas foil bearings are the bearing structural properties (stiffness, damping), and the stresses and strains on the rotor due to high shaft speeds (which cause rotor growth and distortions). Ultimately, Ref. [12] suggests hybrid bearings as the next step in the evolution of the BFB. Hybrid bearings would utilize air pressurization or electromagnetic technology as a means of increasing damping (when crossing critical speeds), and eliminating rotor wear from rubbing during start and stop.

Bump foil bearing force coefficients

Structural force coefficients (no journal rotation)

Bearing force coefficients, stiffness and damping, are critical mechanical parameters that determine its ability to control rotor vibrations. Note that each BFB is custom built and, as a result, even similar sized BFBs may show different stiffness and damping properties as well as load capacity [1]. The variability in BFB performance complicates the bearing selection process, making BFB implementation, based solely on predictions and design guidelines, unlikely to succeed. In actuality, the successful implementation of GFBs relies on the use of design guidelines and ROTs, in conjunction with extensive experimentation. DellaCorte *et al*. [1] introduces a simple, empirically derived "rules of thumb" or guidelines for the prediction of stiffness and damping in BFBs, as they did in Ref. [9]. A BFB's stiffness (K) ranging from 683-2050 (L x D) MN/m^3 and damping C~ 27-273 (L x D) kN/m/m^2 respectively. Note that these ROTs are not a function of surface speed, like the ROT for load capacity [10]. This shows one of the inadequacies of the ROT, as the stiffness and damping properties of a BFB change greatly with the operating rotor speed and the excitation frequency. In actuality, radial bearings are two degrees of freedom mechanical elements best characterized by four stiffness and four damping coefficients, all depending on the excitation frequency, rotor speed and whirl (excitation) frequency, as well as the rotor displacement amplitude [1,8,12,13].

Kim *et al*. and San Andrés *et al.* [13-16] identify the frequency dependent force coefficients of the BFB understructure without journal rotation. Kim *et al.* [12] investigate the effects of temperature and excitation frequency on the structural force coefficients of a generation II BFB. The structure of the BFB contains multiple arcuate bump strips that line the inner surface of the bearing cartridge. Dynamic load tests, conducted with single frequency load excitations, show that the BFB structural stiffness increases (up to 57%) with increasing excitation frequency (~40-200Hz) and dynamic load amplitude (~13-31N) and decreases (by 58%) with an increasing operating temperature (~22-188°C). The increase in stiffness is due to the bumps sticking during loading (regions where the bump displacement does not change under changes in load,

which is typical of systems with dry friction). The stiffness of the BFB decreases with an increase in temperature due to an increase in the radial clearance. The damping coefficients decrease significantly with increasing excitation frequency and shaft temperature.

Rubio and San Andrés [14, 15] conduct an extensive investigation on the structure of BFBs (without journal rotation). Ref. [14] evaluates the effects of bump geometry, preload, bearing angular orientation and dry friction coefficients on the structural stiffness of a generation II BFB. Increasing the shaft diameter (via shafts machined with larger diameters) effectively introduces a mechanical preload into the bearing. Experimental results show that bearing structural stiffness increases nonlinearly with shaft deflection and mechanical preload (shaft diameter). A simple predictive tool, based on Iordanoff's equations for bump stiffness [16] and neglecting the interaction of adjacent bumps, delivers predictions that agree with the experimental results. Note also that increases in the dry friction coefficient cause the bump structural stiffness to increase.

Ref. [15] reports measurements of the BFB structural stiffness and equivalent viscous damping coefficient, or its equivalent dry friction coefficient, for operation under dynamic loads and at moderate temperature. Mechanical energy dissipation or damping is critical for rotor bearing systems to safely traverse critical speeds (system natural frequencies). Coulomb dry friction, or viscous type damping, or structural type damping are models used to characterize the mechanical energy dissipated in a BFB structure.

Test results in Ref. [15] show that the equivalent viscous damping coefficient in a generation II BFB is strongly dependent (inversely proportional) on the excitation frequency and load amplitude. For load excitations well above the system natural frequency the test results show small viscous damping. The estimated dry friction force increases as the natural frequency is approached and also with dynamic load amplitude (up to 20 N). The bearing dry friction coefficient ranges from 0.05 to 0.2 for the applied load range, and remains uniform for excitation frequencies below the natural frequency.

Above the natural frequency, the dry friction coefficient decreases at a steep rate due to dramatic reductions in the excitation load amplitude. Recall from linear vibrations theory that at the system natural frequency small loads can cause large displacements. Also note that a resonance around the natural frequency greatly affects the measurements, making the identification of viscous damping and or dry friction in this region unreliable.
The authors note that the mechanical energy dissipation in a BFB, a combination of hysteretic damping and dry friction, is best quantified by a structural loss factor (γ).

San Andrés and Norsworthy [17] investigate the structural stiffness of a BFB with shims. Three shims of two thicknesses (50 μm and 100 μm) are adhered 120° apart from each other under the bump foil strip. Results from static load tests (up to 1.43 bar specific load) show that the structural stiffness of the shimmed BFB is significantly higher (in particular at large bump deflections, ~50 μm). At large bump deflections (>50 μm), the BFB with 50 μm shims has a stiffness twice as large as that of the original bearing. However, at low bump deflections (30 μm) the structural stiffness of the original bearing and the BFB with 50 μm shims differ by less than 10%. The BFB with 100 μm shims (which introduces an interference fit) shows a structural stiffness up to four times larger than that of the original bearing. The mechanical energy dissipation capability of a bump foil bearing, a combination of dry friction and viscous damping (when airborne) effects is best quantified by a loss factor (for static load tests, $\gamma=E_{dis}/(\pi K_{eq}X^2)$ [18], where E_{dis} is the energy dissipated, X is the amplitude of bump deflection and K_{eq} is an equivalent bearing stiffness). The bearing loss factor (γ), evidencing mechanical energy dissipation, for the original bearing is very small (γ~0.07). The BFB with 50 μm shims has a larger loss factor, γ~0.20, than that of the original bearing. The BFB with 100 μm shims has approximately the same loss factor as that of the original bearing. It is speculated that the interference fit installed by the 100 μm shims hinders the motion of the bump foil leading to a similar amount of energy dissipation as that of the original bearing.

Rotordynamic force coefficients (GFB operating with journal rotation)

During operation (journal rotation enabling lift off) the compliant bump foil understructure is in series with the gas film; which, thin by necessity, does contribute stiffness and damping force coefficients.

Matta *et al.* [19] describe a test rig for the identification of frequency dependent dynamic force coefficients (stiffness and damping) of BFBs (L=D=30 mm) operating with journal rotation i.e., rotordynamic force coefficients. This test rig features an electric spindle which drives a shaft (30 mm) up to 60 krpm. Hybrid (hydrodynamic and hydrostatic) journal bearings support the shaft. The test bearing floats atop an overhung section of the test rotor and is supported by a soft elastic structure known as a "squirrel cage". The squirrel cage enables proper position of bearing on the journal. The mass and stiffness of the squirrel cage are estimated prior to dynamic load tests. Two orthogonally positioned electromagnetic shakers, suspended from a metal frame, apply dynamic loads while a spring is used to apply static loads. Typically dynamic load excitations containing a single frequency are employed in parameter identification; however, tests to cover a large frequency range can be time consuming and arduous. Other alternatives include sine sweep load excitations, a sinusoidal waveform containing a successive frequency range, and pseudorandom excitations containing equal amplitude sine waves of different frequencies. Matta *et al.* employ pseudorandom excitations (50-450Hz) in their dynamic load tests. The parameter identification consists of a nonlinear minimization of the first order transfer function (X/F i.e., displacement/force). In general results show that the bearing direct stiffness increases with excitation frequency (50-450 Hz), static load (15 N, 20 N), and speed (15-25 krpm). The damping coefficients are largely unaffected by static load but also decrease with excitation frequency and journal speed. In a subsequent paper, Rudloff *et al*. [20] also use two shakers to excite a floating bearing. The study is quite comprehensive and shows that the force coefficients in generation I BFBs are strong functions of the excitation frequency (100-600 Hz); however, the magnitude of the force coefficients is largely unaffected by rotor speed.

Chirathadam and San Andrés [21] report rotordynamic force coefficients (direct and cross coupled coefficients as well as the bearing loss factor) for a first generation BFB (L= 38.0 mm, D=36.5 mm) operating over a higher frequency range than in Ref. [15] (200-400 Hz). Orthogonally mounted shakers excite a test bearing floating on a turbocharger driven rig. Measurements are conducted with a journal speed of 50 krpm (833 Hz). The bearing motion amplitude is 25 μm and the bearing clearance is 0.11 mm. The direct stiffness coefficients of the BFB increase significantly with excitation frequency while the cross coupled stiffness coefficients are small (~0). The stiffness is higher in the Y-direction than the X-direction indicating some circumferential non uniformity in the bearing bump structure. The direct equivalent viscous damping coefficients also increase with excitation frequency. The authors note that the large magnitude forces applied to the bearing may play a role on the observed behavior. The cross coupled damping coefficients are also small. The bearing loss factor (for dynamic load tests, $\gamma=\omega(C_{XX}+C_{YY})/(K_{XX}+K_{YY})$ ~ 0.2-0.4, is largely independent of frequency. The loss factor (γ) is slightly higher when there is journal rotation than without.

Conlon *et al.* [22] compare the load capacity and force coefficients of similarly sized (L=D=70 mm) generation I and II bearings. A static load [$W/(LD)$~714 kPa] and dynamic loads [($W/(LD)$)~ 91 kPa] are applied to both bearings. For static loads (with no journal rotation) the generation I bearing demonstrates higher structural stiffness coefficients than a generation II bearing. The freely moving bump foil strips of a generation II bearing are less constrained than the single bump foil strip of a generation I bearing, which leads to the lower structural stiffness shown in the generation II BFB. Load capacity tests ($W/(LD)$~41 kPa to 142 kPa) confirm that friction (power) losses increase with both static load and rotor speed. In general, the generation II BFB demonstrates a load capacity twice as high as the generation I BFB due to an improved pressure generation capability. While the static stiffness of the generation II bearing is lower than the generation I, the dynamic force coefficients (stiffness and damping) are significantly larger than those of the generation I bearing. The authors attribute this

result to a higher degree of nonlinearity in the force coefficients (stiffness and damping) of the generation II.

Measurements of drag torque

During rotor start up and shut down, due to the lack of a gas film, the rotor rubs on its bearings thus generating both heat and wear of components. Reducing the amount of time the rotor and bearing are in contact is important for the health of the rotor-bearing system. Rudloff *et al*. [20] report measurements of bearing start up torque and lift off shaft speed for a generation I BFB. Drag torque measurements are carried out for increasing specific loads ($W/(LD)$~7-35 kPa) and for increasing shaft speeds (15.6 krpm-35 krpm). There are two distinct regions of high drag torque, one associated with the rotor lift off and the other with touch-down. These regions have the highest drag torque due to the contact of the rotor with the bearing inner surface. Note that the drag torque upon either rotor start up or shut down is due to friction (between the rotor and bearing surfaces), while drag torque during operation is due to the viscous shearing of the gas film. The shaft lift off speed, typically between 2.7 krpm and 5 krpm, increases for increasing static loads.

Chirathadam and San Andrés [21] demonstrate that the drag power loss of a BFB (L/D~1) increases with rotor speed as well as increasing static load. Also Ref. [21] shows that the peak startup drag torque increases significantly with increasing static load. This result is not surprising given that static loads increase the friction force by increasing the contact pressure on the bearing inner surface.

Radil *et al.* [23] state that, in general, foil bearing failure is due in large part to thermal gradients brought on by a large viscous power loss. The authors present a 3D performance for a generation III BFB (L=35mm, D=27mm). The map relates the power loss, static load (max. 12 kPa), and operating speed (max. 55krpm) to aid in the design and selection of BFBs that operate away from thermal gradients that could lead to thermal runaway and ultimately bearing failure. The performance map is divided into two regions; one dominated by high loads and low shaft speeds (highly loaded region), and a lightly loaded region dominated by low loads and high shaft speeds. The authors

suggest designing foil bearings to operate in the "lightly loaded" region of the performance map. The lightly loaded region is a landscape where the film thickness supports the desired load while maintaining a low viscous drag power loss. Increasing the static load or decreasing shaft speed transitions the bearing to the highly loaded region and exposes the bearing to large increases in drag power loss. Foil bearings are susceptible to thermal runaway if operating in the highly loaded region. Ultimately, the performance map presents a tool for assessing if a generation III BFB is operating in a thermally safe region, and for determining a safety margin (allowable deviations in load or shaft speed) for the bearing to operate without risking failure.

Characteristics of rotors supported on foil bearings

Research also focuses on studying the rotordynamic response of rotors supported on BFBs. Rotors supported on BFBs often show large and potentially catastrophic subharmonic whirl motions that may synchronize with the shaft speed or lock at a system resonant frequency misleadingly termed a rotordynamic instability [24, 25]. What follows is a brief review of the research pertaining to the persistence of subsynchronous whirl motions in BFB supported rotors.

Rubio and San Andrés [4] demonstrate that an increase in air feed pressurization reduces the amplitude of subsynchronous whirl motions in a rotor supported on BFBs and while it crosses system natural frequencies. External pressurization has no effect on the rotor synchronous motion amplitude response for operation well above critical speeds. A model of GFBs with side pressurization advanced in Ref. [4] predicts increased direct stiffness and damping coefficients as well as reduced cross-coupled stiffness coefficients as the feed pressure rises. Decreased cross-coupled stiffnesses increase the stability of rotor-bearing systems (RBS). Ref. [4] thus reports a method to reduce subsynchronous whirl motion amplitudes, thereby improving the stability of a RBS.

Kim and San Andrés [24] observe large amplitude (56 μm) subharmonic motions in speed coast down measurements of a rotor supported on BFBs. The whirl motions have a frequency equal to 1/2 and 1/3 of the synchronous speed. Subsynchronous vibrations are

ascribed to the nonlinear stiffness characteristics of the FB structure and are exacerbated by the presence of rotor imbalance. Kim and San Andrés note that the performance of RBS is largely dependent on the underspring structural characteristics and that foil bearings implementation into a RBS requires careful design with the entire system in consideration. Ref. [25] reviews the prior literature giving many more examples of RBSs displaying subsynchronous motion responses.

Heshmat *et al.* [8] propose a "three-pad" bearing as a means enhancing the stability of BFBs operating at high speeds (<100krpm). The "three pad" bearing consists of three separate (equal length) sections of bump and top foils, each welded to the inner surface of the bearing cartridge. These sections featured bumps of varying pitch such that the stiffness increasing toward the weld location, thereby improving convergence and enhancing the generation of hydrodynamic film pressure. A rotor supported on a pair of three-pad bearings shows stable operation up to 120 krpm with only small subsynchronous vibration components.

Kim and San Andrés [4] investigate the dynamic response of a rotor supported on mechanically preloaded (shimmed) foil bearings. The preload, introduced by affixing metal shims to the inner surface of the bearing cartridge, effectively introduces a hydrodynamic wedge that increases the hydrodynamic film pressure, leading to an increase in load capacity. The shims also create an angular stiffness gradient similar to that of the "three pad" bearing discussed above [9]. Rotor coast down responses are obtained for a rotor supported on BFBs with and without shims. The response of a rotor supported on bearings without shims shows large amplitudes subsynchronous whirl motion (50 μm) for rotor speeds ranging from 27 krpm and 50 krpm with low feed pressure (0.35 bar). Under the same test conditions, the rotor supported on shimmed bearings shows smaller subsynchronous whirl amplitudes (20 μm) over a smaller shaft speed range (38 krpm to 50 krpm). The tests results in Ref. [4] demonstrate that mechanical preload reduces the severity of rotor subsynchronous whirl motions as well as delays their onset. This information has the potential to extend the life of high-speed rotating machinery.

In Ref. [6] a pressurized air driven TC is revamped to incorporate one test BFB and a thrust foil bearing. Rotor speed coast down experiments (from 82 krpm) were conducted for bearings with and without shims. Rotor response data from waterfall plots demonstrate that a shimmed foil bearing delays the onset speed of subsynchronous whirl motions and attenuates their amplitude in the TC. The authors note that TC rotor speed versus diesel engine speed data evidences that shimmed BFBs may have slightly higher drag power losses.

Sim *et al*. [26] in a follow up paper discuss the effects of mechanical preload on the rotordynamic performance of a rotor supported on a pair of three-pad BFBs assembled with large radial clearance (~ 150 μm). The bearing features 120° top foil and bump foil strips and mechanical preloads (of various magnitudes) machined into the bearing cartridge. The mechanical preload of the three-pad (or lobed) bearing is defined as the distance between a pad (or lobe) arc and the center of the bearing. Rotor speed up and coast down tests show that as the mechanical preload increases (from 0 to 100 μm) the onset speed of instability increases from 62 krpm (for a cylindrical bearing) to 70 krpm (with a 70 μm preload), until there is no sub synchronous motion (with a 100 μm preload). Note also that the magnitude of both the synchronous and subsynchronous whirl motions decreases with an increasing preload. The sub synchronous whirl motions, occurring between 120 Hz and 190 Hz, are noted to occur near a system critical speed. The subsychronous whirl motion are attributed to nonlinearities in the BFB elastic structure. The rotordynamic performance of the three pad bearing is compared to a similarly sized single pad BFB (with a 100 μm preload). The single pad (360°) BFB shows the lowest onset speed of instability of all the tests bearings and preload conditions, and therefore has the least favorable performance. The authors predict the bearing force coefficients based on the computational model and show a strong stiffening effect with an increasing preload and rotor speed.

Schiffmann and Spakovsky [27] investigate (numerically) the role of underspring stiffness, structural damping, and static load on the rotordynamic stability of a rigid rotor supported on first generation BFBs. Schiffmann and Spakovsky [27] reports that

decreasing the bearing underspring compliance (increasing its stiffness) and increasing the static load can significantly improve the RBS stability (critical mass) and increase the onset speed of instability while damping has only a marginal effect. The authors note that an increased static load affects the fluid film thickness and the pressure distribution such that the ratio of cross-coupled and direct force coefficients (stiffness and damping) decreases thereby improving stability. The authors conjecture that tailoring the fluid film pressure profile by introducing shims at specific circumferential locations (selective shimming) is a means to increase the system onset speed of instability. Furthermore, Schiffman and Spakovsky produce design guidelines and optimum shim patterns (a certain set of shims, varying in thickness, at discrete angular locations) for improved FB stability. While these optimum shim patterns promise improved rotordynamic stability for BFB supported rotors, a single shim pattern requires shims of thickness ranging from 50% to 90% of the bearing clearance[3]. The availability of shims of very particular thickness is limited, making the shim patterns rather impractical.

Statement of work

There is limited experimental data on the force coefficients and transient startup and shut down performance of shimmed BFBs. The main objective of the research is to experimentally measure the transient rotor start up and shut down events, drag torque, and the frequency dependent force coefficients of shimmed bump-type foil bearings. The present research will determine the stiffness and damping coefficients of shimmed BFBs while airborne as well as their operating drag torque.

[3] Note that an optimization process determines the thickness and location of each shim that comprises the shim pattern in Ref. [27]. As a result, each shim pattern is customized for the particular bearing and its operating conditions.

CHAPTER II

TEST BUMP FOIL BEARING*

Two types of measurements are conducted on a generation I test BFB described below: (a) drag torque measurements during the rotor speed startup, speed shut down, and while operating at a constant speed (50 krpm) and (b) dynamic load tests to identify force coefficients.

A mechanical preload is added to the BFB structure by inserting shims of known thickness between the bearing cartridge and the bump foil. Figure 2 presents a schematic view of a typical BFB and a BFB with shims added at discrete circumferential locations.

Table 1 shows the dimensions of the test bearing, test shaft, and the metal shims and Figure 3 shows a photograph of a bump foil bearing with a metal shim inserted between the bearing cartridge and the bump foil layers. During loading, the bumps atop a shim are compressed before other bumps since a shim pushes the bumps toward the rotor.

The BFB[4] consists of a top foil and a single underspring layer with 26 bumps. Both foils, made of Inconel X750, are uncoated. The bearing fits into a steel cartridge that also hosts instrumentation.

---

* Reprinted with permission from " Measurement of drag torque and lift off speed and rotordynamic force coefficients in a shimmed BFB," by San Andrés, L., and Norsworthy, J., 2014, (Pennacchi P (Ed.): Proceedings of the 9th International Conference on Rotordynamics, Copyright (2015) Springer. All rights reserved).

[4]The Korean Institute of Science and Technology (KIST) manufactured the BFB.

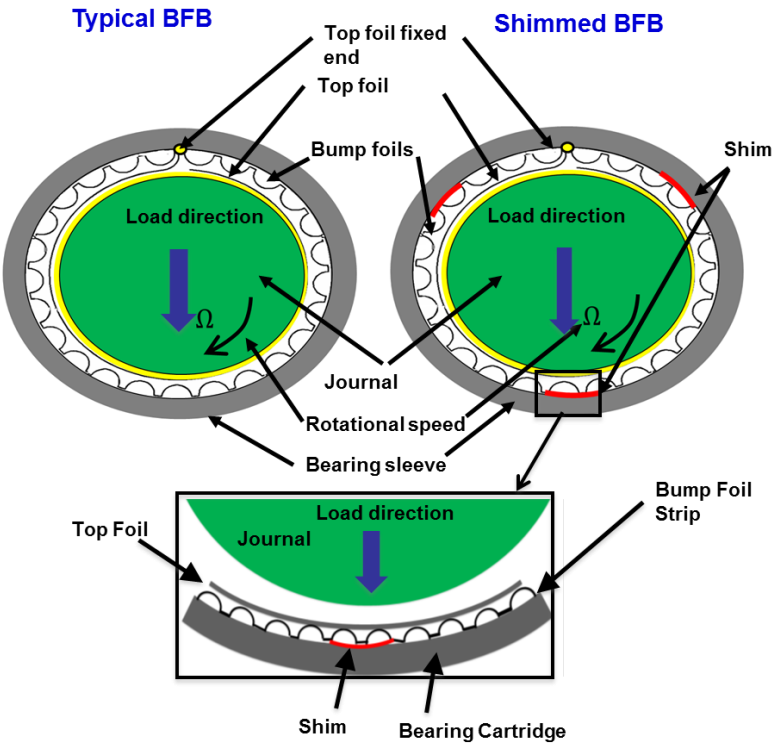

Figure 2. Schematic representation of a typical first generation bump-type foil bearing and a shimmed BFB. Inset shows a zoomed in view of the area around a shim.

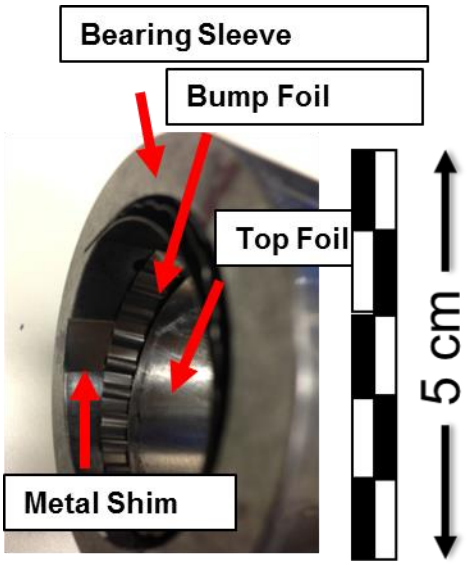

(a)

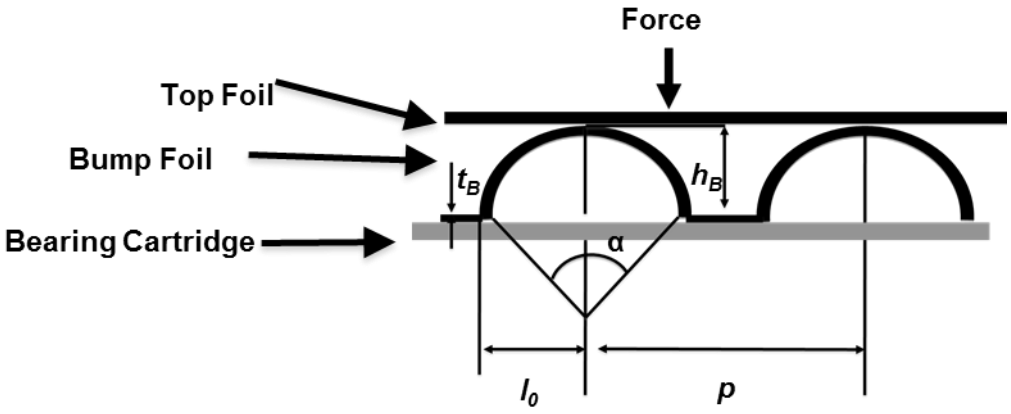

(b)

Figure 3. (a) Schematic view of a bump foil and geometric parameters, and (b) a photograph of a BFB with a metal shim layered axially through the bearing [5].

Table 1 Nominal dimensions of the test foil bearing and metal shims.

Parameters	**Magnitude**
Bearing cartridge outer diameter, D_O	50.74 mm
Bearing cartridge inner diameter, D_I	37.98 mm
Shaft diameter, D_s (includes coating thickness)	36.5 mm
Bearing axial length, L	38.10 mm
Top foil thickness (Inconel X750), t_T	0.1 mm
Foil length , $2\pi D_\mathrm{I}$	110 mm
Elastic modulus, E	209 GPa
Poisson's ratio, v	0.29
Number of bumps, N_B	25
Bump foil (Inconel X750)	
Thickness, t_B	0.112 mm
Pitch, s_0	4.5 mm
Length, l_B	2.1 mm
Height, h	0.50 mm
Elastic modulus, E	209 GPa
Poisson's ratio, v	0.29
Shim (AISI 4140)	
Length	38.1 mm
Thickness, t_s	0.050, 0.030 mm
Width	7.87 mm
Angular extent	11.8°
Elastic modulus, E	209 GPa
Poisson's ratio, v	0.29
Measured inner diameter of the FB (assembled), D_A	36.74 mm
Nominal FB radial clearance[5], c_{nom}	0.120 mm
Weight of test bearing and outer cartridge, W_B	10 N

[5] Determined from the bearing dimensions as $c_{nom} = 0.5\left(D_A - D_s\right)$ where D_A is the measured inner diameter of the bearing once assembled.

Figure 4 shows, for increasing shim thicknesses, the predicted bearing radial clearance relative to the nominal radial clearance (c_{nom}~120 μm) versus angular location. The clearance profile in a bearing with three equally spaced shims of known thickness, t_s, and nominal clearance, c_{nom}, is [4]

$$c_{(\theta)} = \left(1 - \frac{t_s}{2c_{nom}}\right) c_{nom} - \frac{1}{2} t_s \cos\left[\left(N_S\left(\theta - \theta_1 - \theta_p\right)\right)\right] \quad (1)$$

where θ is an arbitrary angular location, θ_1 is the angular location of the middle of a first shim (counter clockwise direction), N_s is the number of shims, and θ_p (~120°) is the angular space between shims. Figure 4 shows the bearing radial clearance relative to the nominal radial clearance (c_{nom}=120 μm) versus the angular location (θ) for instances two shim thicknesses (30 μm and 50 μm). The clearance in a bearing with shims is periodic resembling that in a tri-lobe bearing. For a bearing with both 30 μm shims and 50 μm shims, the clearance at the location of the shims reduces by 20% and 40%, respectively. The addition of increasingly thicker shims eventually would lead to a condition of interference fit of the bearing top foil with the rotor.

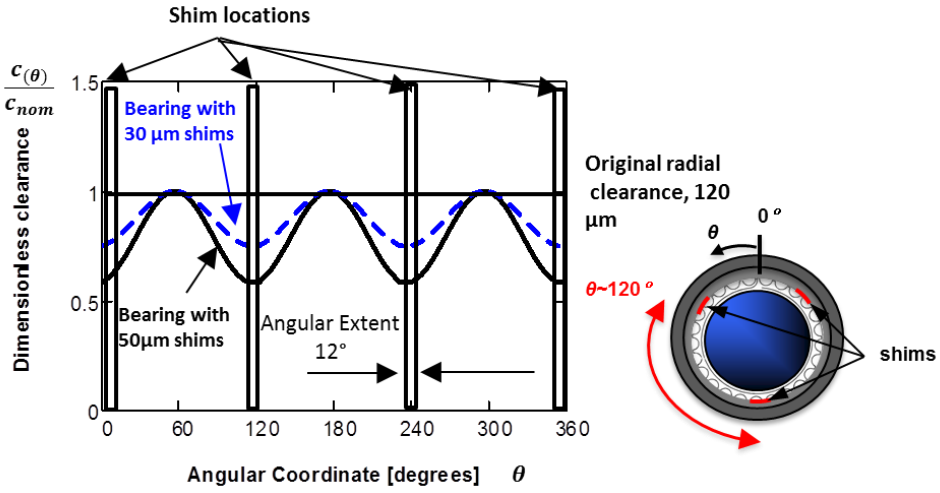

Figure 4. Dimensionless clearance profile of a bump foil bearing versus angular coordinates (θ) for two shim thicknesses (30 μm and 50 μm). Nominal radial clearance is 120 μm.

CHAPTER III

MEASUREMENT OF THE DRAG TORQUE IN A BFB*

During rotor speed startup and shut down, BFBs exhibit high drag torque due to rubbing contact with the rotor surface. Drag torque measurements aim to assess the effect of an applied static load (*W/(LD)*), and shim thickness (t_s), on the test element drag torque, friction factor, and bearing lift off speed. The drag torque is measured for two operating regimes; rotor speed startup (where dry friction sliding is prevalent) to rotor lift off, and airborne operation at a constant shaft speed.

Measurement of BFB breakaway torque

This section details the measurement of the torque needed to overcome the static friction due to contact between the rotor and bearing surfaces via a simple torque screwdriver (without journal speed). This torque is termed as breakaway torque. Figure 5 shows a photograph of the test setup used to measure the breakaway torque of the BFB. The bearing is rigidly held by a threaded steel rod, and the rotor is manually rotated toward the top foil free end. An ad-hoc setup is assembled to apply vertical loads onto the BFB.

* Portions reprinted with permission from " Measurement of drag torque and lift off speed and rotordynamic force coefficients in a shimmed BFB," by San Andrés, L., and Norsworthy, J., 2014, (Pennacchi P (Ed.): Proceedings of the 9th International Conference on Rotordynamics, Copyright (2015) Springer. All rights reserved.)

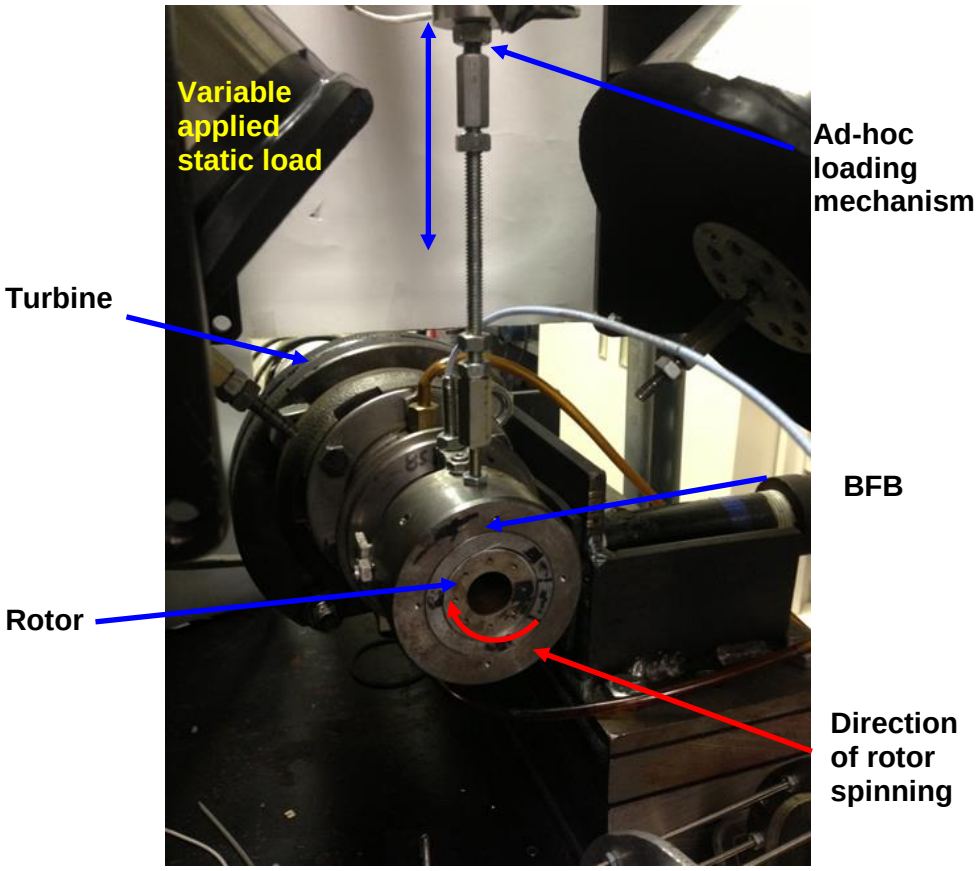

Figure 5. Photograph of the test setup to measure breakaway torque in a BFB.

Figures 5 and 6 present schematic views of the BFB upon journal rotation. The vertical static load (W) pulls the rotor into contact with the bearing thus generating a contact pressure (P_r) on the bearing surface; ($W = \iint P_r R\cos(\theta) d\theta dz$). Note that θ is an angular coordinate around the surface of the circumference of the bearing, and z is a coordinate stretching axially. Also note that only one component of the contact pressure opposes the applied vertical load ($P_r\cos(\theta)$), while ($P_r\sin(\theta)$) when integrated over the bearing surface area equals zero i.e., $\iint P_r R\sin(\theta) d\theta dz = 0$.

Drag shear stresses (τ) arise when the journal turns. The shear stress ($\tau \sim P_r$)[6] is prortional to the contact pressure (P_r), and when integrated over the bearing surface are, gives a drag torque ($T = \iint \tau R^2 d\theta dz$). Note that the local contact pressure (P_r), and shear stresses (τ) are vector quantities with directions as represented in Figure 7.

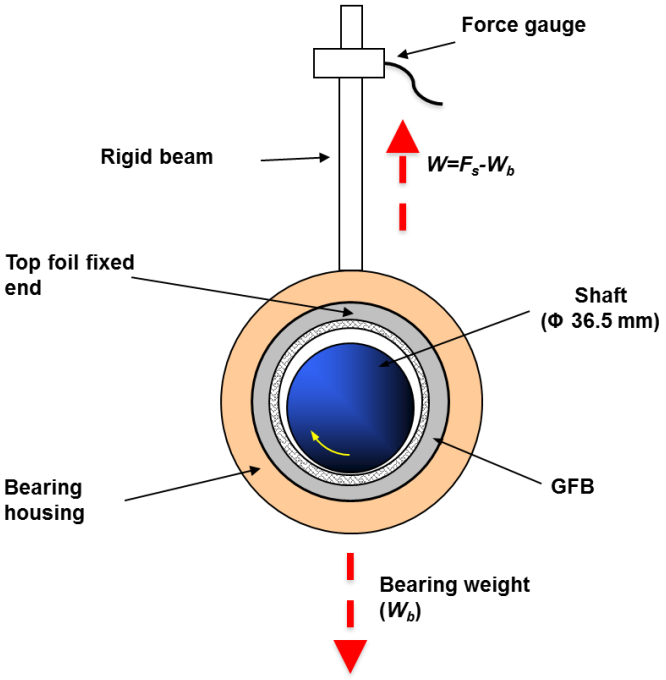

Figure 6. Schematic view of the test setup used to measure the breakaway drag torque of a BFB.

[6] Upon journal rotation (prior to journal lift off), the shear stress (τ) is due to friction between the shaft and the bearing inner surface. $\tau = \frac{F_s}{A} = \mu_f P_r$ where μ_f is a coefficient of dry friction, F_s is a shear force, and A is the area over which the shear stress acts.

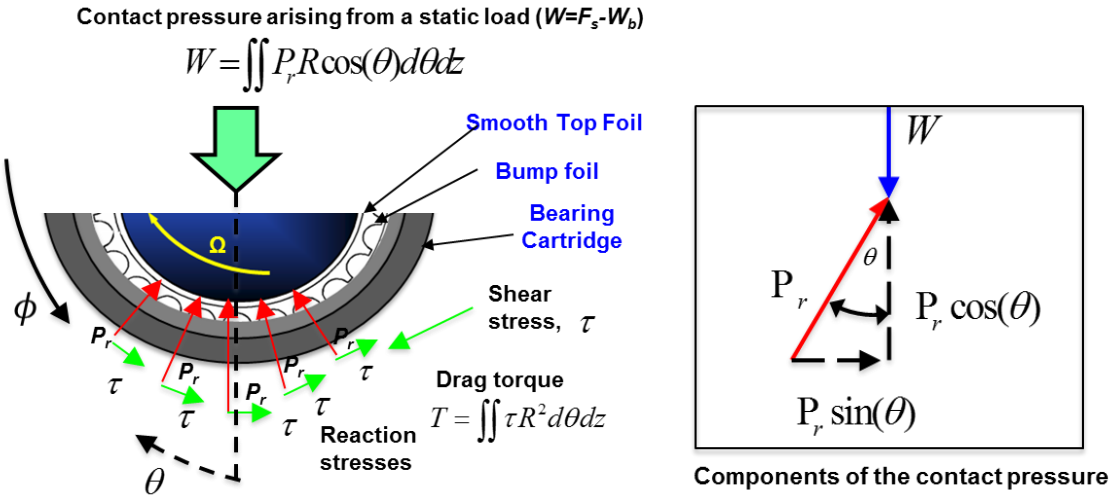

Figure 7. Schematic view of the components of the contact pressure and shear stresses reacting on the BFB understructure during loading and journal rotation.

A torque screwdriver (TS) (graduations: 56 N-mm, uncertainty: 28 N-mm), shown in Figure 8, is used to manually apply and measure the torque applied to the turbocharger (TC) shaft.

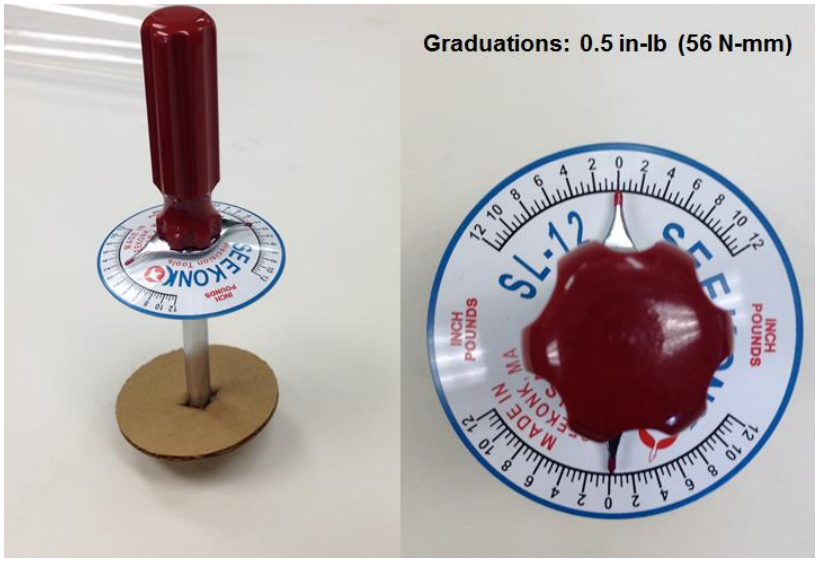

Figure 8. Photograph of the torque screwdriver.

The manually applied torque is increased until the journal turns inside the bearing. The torque is identified as a breakaway torque ($T_{\text{breakaway}}$). Note that the TC rotor is supported by oil lubricated ball bearings which provide an additional residual drag torque. However, this torque is small < 10 N-mm. Consult Appendix A for details.

Note from Figure 7 that the net static vertical load ($W=F_s-W_b$) is the applied static load (F_s) minus the bearing weight (W_b); while the applied torque (T_a) equals a dry-friction shear torque (T_{drag}) from the frictional contact between the BFB and the shaft. Note also that the bearing foils are uncoated while the rotor surface is coated (25 μm thick) with thin dense chrome (TDC). Shims are introduced to the BFB, as discussed above, to add mechanical preload. The bearing clearance (without shims), as estimated from the bearing geometry, is ~ 120 μm (~4.7 mil) radially.

On the breakaway friction factor of the original and the shimmed bearing

Figure 9 shows the friction factor ($f=T/(RW)$) derived from measurements of the breakaway torque via a torque screwdriver, versus specific load ($W/(LD)$) for a bearing without shims and with shims of thickness 30 μm and 50 μm. Note that for loads below 10 kPa, the bearing friction factor decreases with load, and then is subsequently constant. The friction factor increases with shim thickness. The bearing with 50 μm shims has a friction factor approximately 30% higher than the original bearing (i.e., without shims). Increasing the mechanical preload increases the breakaway friction factor ($f=T/(RW)$) by increasing the local shear stress ($\tau \sim \mu P_r$), and the area of contact between the rotor and the bearing.

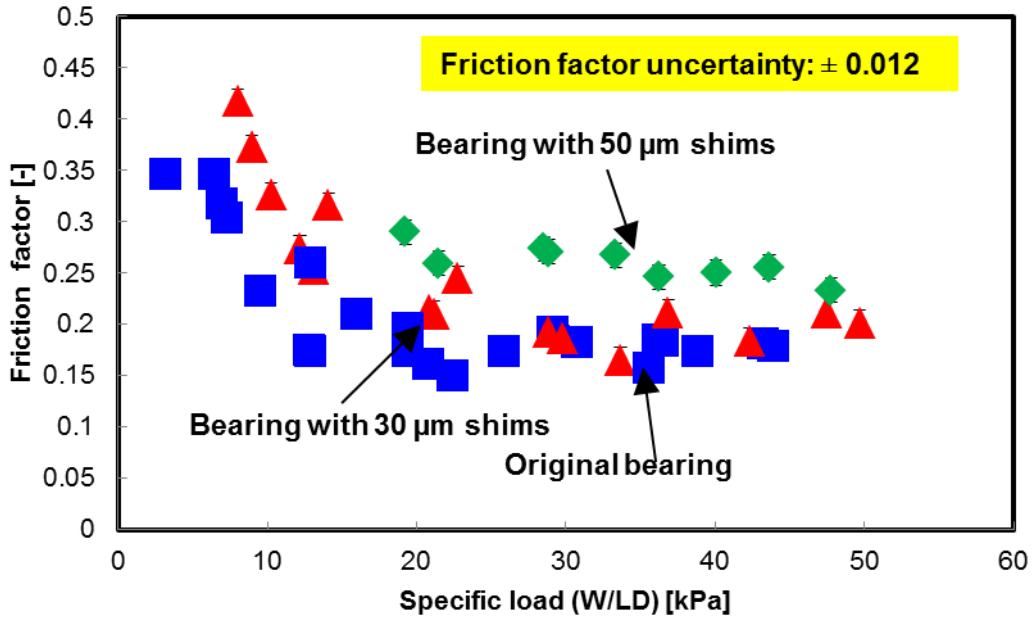

Figure 9. Friction factor (*f=T/(WR)*) derived from the breakaway drag torque versus specific load (*W/(LD)*) for the original bearing and a bearing with shims of thickness 30 µm and 50 µm. Stationary journal.

Test rig to measure the drag torque of a BFB during TC operation (with journal rotation)

Figure 10 presents a schematic view of the test rig used to measure the drag torque of a generation I BFB operating at various rotor speeds. An ad-hoc apparatus featuring a series of ties wrapped around the bearing cartridge is assembled to apply vertical loads to the BFB. The net static load (W) equals the applied static load (F_s) minus the weight of the bearing (W_B~8.9 N), i.e., ($W=F_s-W_B$). Loads ($W/(LD)$) equaling to 6 kPa, 12 kPa, and 20 kPa are applied to the test bearing. Journal rotation causes the lever arm to compress a calibrated spring. An eddy current sensor and an optical tachometer measure the journal rotational speed (Ω) and deflection of spring (δ), respectively. The bearing drag torque is $T=\delta\, K_s\, L$, with, $K_s \sim 5.9$ N/mm as the stiffness of the spring (uncertainty ±0.33 N/mm), and L_T (~152 mm) is the length of the lever arm. The raw drag torque data

is rather noisy, thus every four torque data points are averaged to reduce scatter and smooth the results.

Oil (ISO VG 46) is continuously supplied (at 22° C) to the TC ball bearings throughout the tests. The air inlet valve is controlled (opened) to deliver air to the TC turbine and thus accelerating the rotor to a maximum speed of 50 krpm (833 Hz).

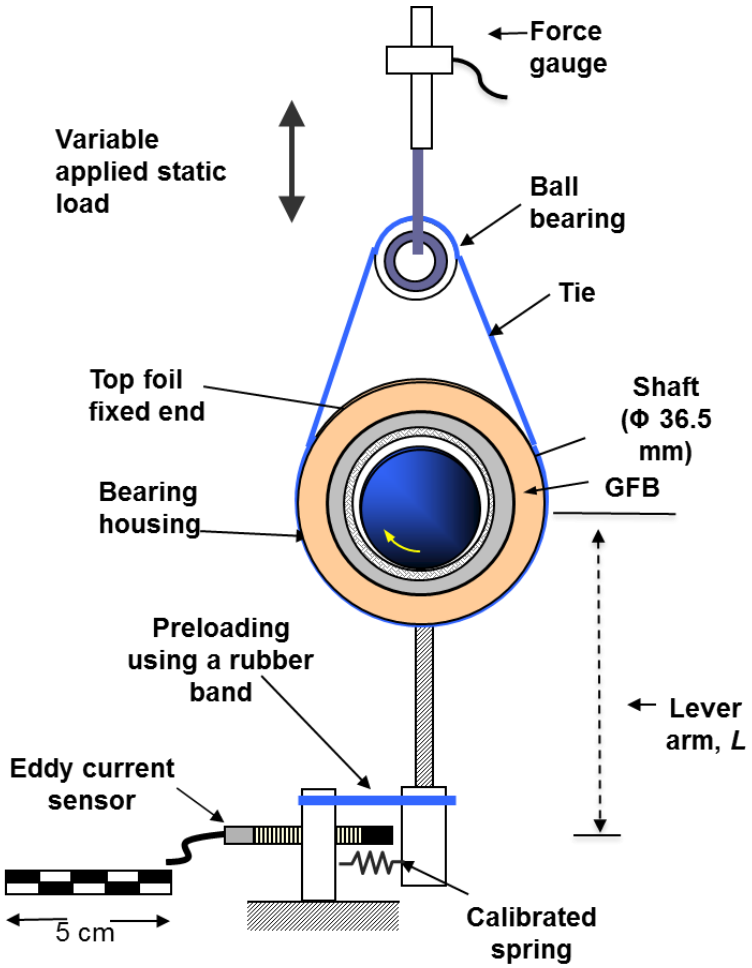

Figure 10. Schematic view of the test rig used to measure bearing drag torque [3].

Drag torque of a BFB without shims

Figure 11 shows the bearing drag torque and rotor speed versus time for the original bearing (without shims) under a specific load *W/(LD)*~0 kPa. Note that there are two regions of large drag torque at low journal speeds; one near the journal speed start up and another at rotor speed shut down. These regions of high drag torque reveal the drag torque required to both overcome dry friction between the bearing and rotor surfaces and then accelerate/decelerate the rotor. The steep drop in drag torque around 20 krpm indicates the rotor lift off rotational speed. The lift off condition denotes the transition to viscous drag as hydrodynamic pressure establishes the gas film separating the journal from the rotor (no contact) [1, 20-21,23]. Note that the drag torque during full film operation, termed as the airborne drag torque (~7 N-mm) is approximately 8% of the peak drag torque (~90 N-mm).

For a bearing (without shims) operating without a static load, *W/(LD)* ~ 0 kPa. Figure 12 shows the bearing drag torque and rotor speed versus elapsed time as zoomed in the rotor speed startup region. The start up[7] torque to overcome static friction, occurs when the rotor begins to turn. Note that the startup torque (~ 40 N-mm) occurs at ~ 3s which corresponds to a torque that is not the max. torque (90 N-mm).

[7] In order to differentiate from the two types of measurements, "startup" refers to torque measurements from experiments with journal rotation and "breakaway" refers to measurements of torque without journal speed via the torque screwdriver.

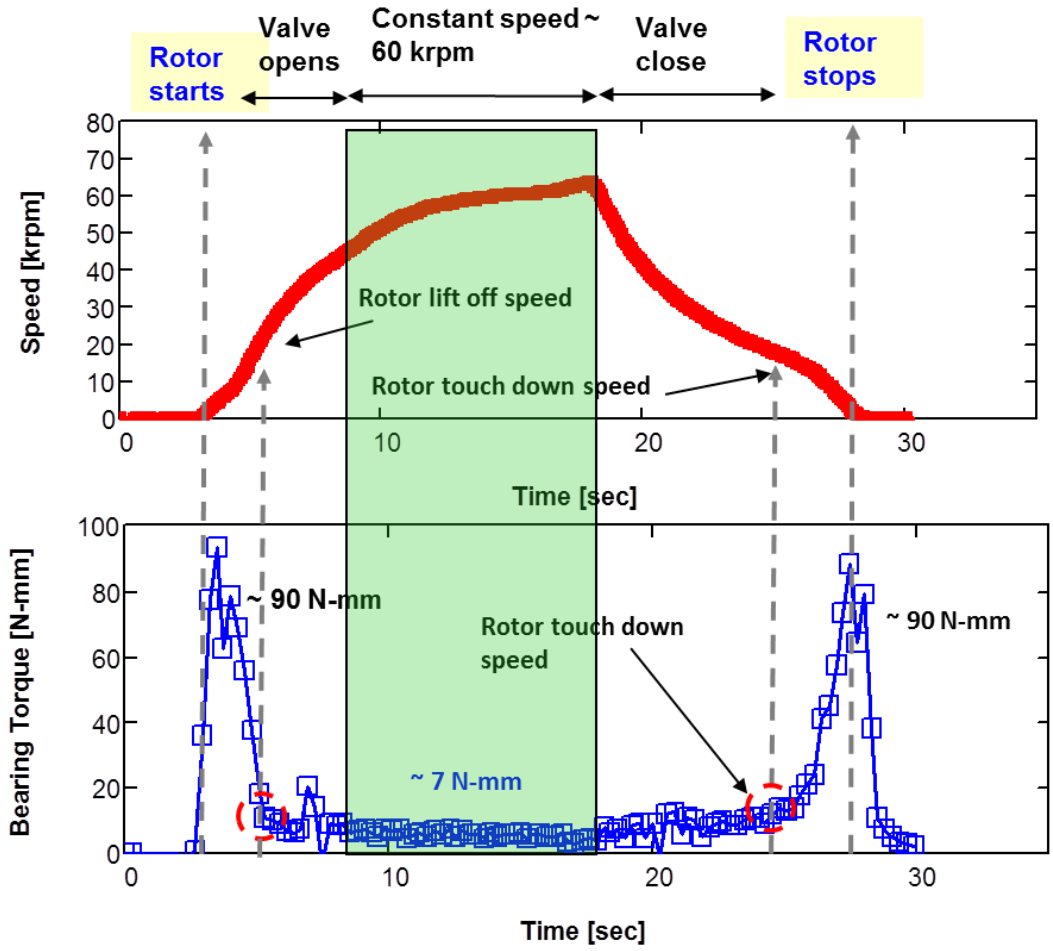

Figure 11. (Top) Bearing drag torque and (bottom) rotor speed versus time for a BFB without shims and for *W/(LD)* ~ 0 kPa.

The further increase in the torque maybe associated to the torque effort required to accelerate the journal while still in contact with bearing (sliding).

Importantly enough, the decrease in torque even as the rotor accelerates (between 4s and 5s in Figure 12) is due to the operator closing the air supply valve, thereby reducing the flow of compressed air supplied to the TC. This action keeps the rotor from reaching excessive speeds (>80 krpm)[8].

[8] To expedite rotor lift off, the valve supplying air to the TC is opened rather wide, thus supplying more than enough flow to turn the turbine and accelerate the rotor. To prevent the shaft speed from reaching ~70 krpm, the valve is closed, thereby reducing the air supplied to the TC.

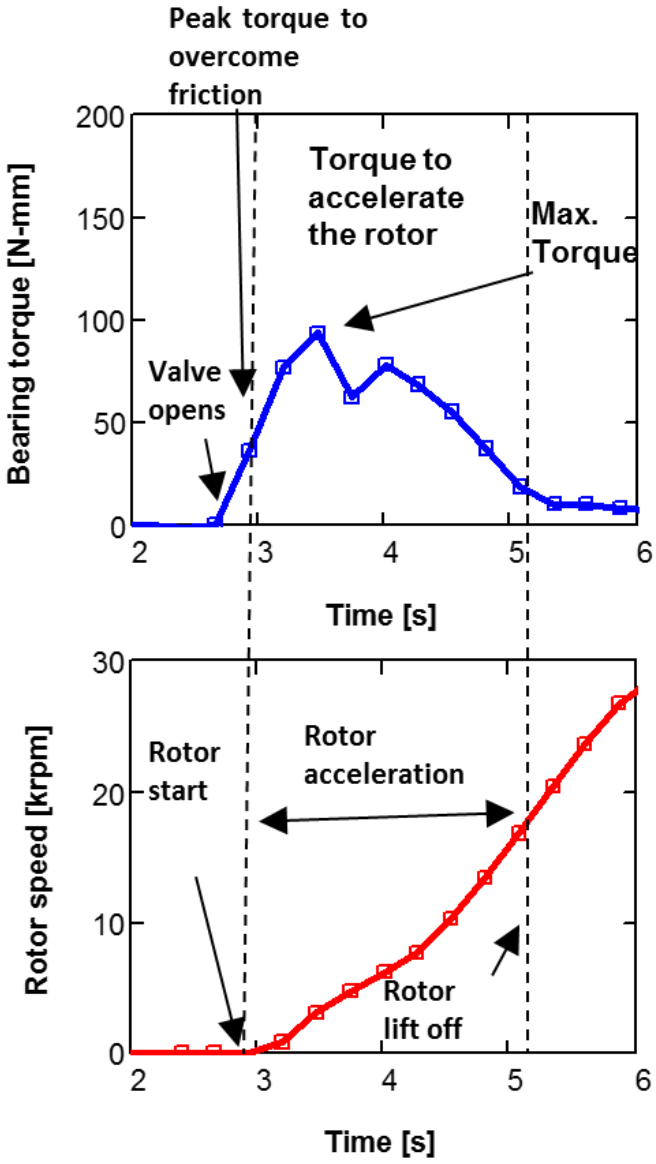

Figure 12. (Top) Bearing drag torque and (bottom) rotor speed versus time for a bearing without shims with *W/(LD)* ~ 0 kPa. Zoomed in on the rotor speed startup region.

Friction factor for a shimmed BFB while airborne (full gas film)

Figure 13 shows the friction factor ($f=T/(RW)$ versus rotor speed for the original bearing without shims and with shims of thickness 30 μm and 50 μm; all operating under various specific loads ($W/(LD)$~ 6 - 20 kPa). During startup, at low shaft speeds, the rotor slides (rub or dry friction condition) on the top foil leading to a large friction factor ($f \geq 0.5$). The large friction factor $f>0.5$ occurring at speeds between 0 krpm and 10 krpm is due to the shaft accelerating while still rubbing against the bearing. The drag torque and derived friction factor to overcome static friction, shown later in Figures 13 and 14, are obtained when the shaft first turns (0 krpm).

The friction factor of the bearing with 30 μm shims is approximately equal to that of the original bearing while the friction factor of the bearing with 50 μm shims is approximately 15% higher than that of the original bearing. While the shaft operates at 50 krpm, the static load significantly affects the friction factor. Specifically f decreases from 0.08 to 0.05 when the load increases from ~ 6 kPa to 20 kPa. Once the rotor lifts, the friction factor changes little with rotor speed. The uncertainty in the friction factor ($f=T/(RW)$) is ±0.008.

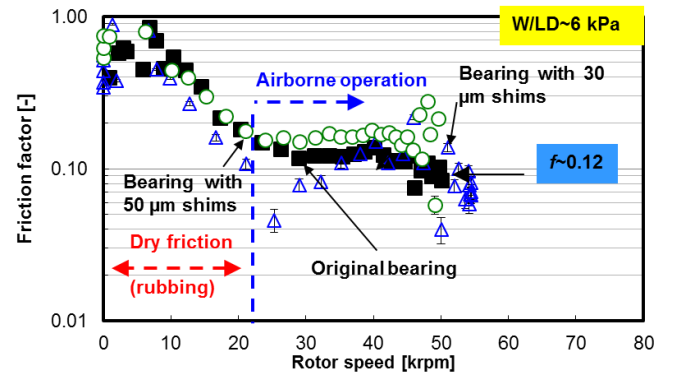

(a) *W/(LD)*~ 6 kPa

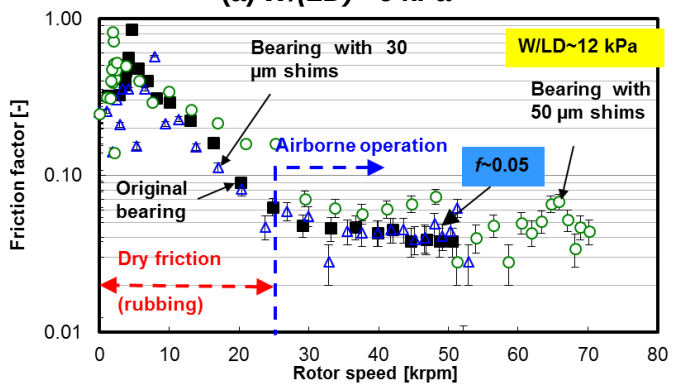

(b) *W/(LD)*~ 12 kPa

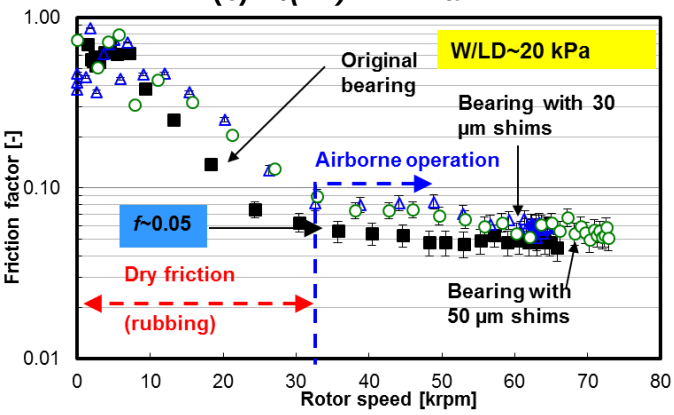

(c) *W/(LD)*~ 20 kPa

Figure 13. Friction factor (*f=T/(RW)* versus rotor speed for the original BFB and bearing with shims of thickness 30 μm and 50 μm. Operation at specific loads (a) *W/(LD)*~6, (b) *W/(LD)*~12 kPa and (c) *W/(LD)*~20 kPa. Measurements during rotor acceleration tests.

Startup drag torque of a shimmed BFB

Metal shims were added to the BFB according to the procedure described in the test bearing description. The metal shims effectively instill a mechanical preload (reduce the clearance and minimum film thickness). This subsection details the effect of shimming on the torque in a generation I BFB during rotor speed startup, constant rotor speed operation, and rotor speed shutdown. The same experimental procedure, described in the section detailing the test rig to measure the airborne drag torque, is followed, and which consists of accelerating the TC journal to ~50 krpm. The test apparatus depicted in Figure 10 is used to record the bearing drag torque.

Figure 14 presents the startup torque (T) and bearing lift off speed versus specific load for a bearing without shims and with shims of thickness 30 μm and 50 μm. The drag torque and derived friction factor to overcome static friction, shown in Figure 14 and 14, are obtained when the shaft first turns (at ~ 0 krpm, immediately prior to the journal turning) (see Figure 13).

The bearing lift off speed is identified as the journal speed at which the bearing drag torque ceases to decrease further indicating that a minimum film thickness is generated, lifting the rotor from contact with the bearing.

The startup torque for the shimmed bearings increases with load and is increased for a bearing with shims. The lift off speed for the original bearing increases (by 37%) with load. As load (*W/(LD)*) increases, the hydrodynamic pressure needed to lift the bearing increases. High rotor speeds (~20 krpm) will generate a hydrodynamic pressure that lifts the rotor from contacting with the bearing, thus effectively creating a gas film thickness. To generate more hydrodynamic pressure the rotor must spin faster requiring a higher lift off speed.

The tests are repeated three times for each static load. The maximum variance in the lift off speed measurements is ±3 krpm. The maximum variance in the lift off speed measurements for the shimmed bearings is ±2.5 krpm (also occurring at the max. specific load). Given the variance in the lift off speed measurement, the bearing with 30 μm shims show a lift off journal speed similar to the original bearing. The maximum variance in the startup torque measurements is 20 N-mm (which occurs at *W/(LD)*~20 kPa), however the average variance is ±5 N-mm (consult Appendix C for details on the uncertainty analysis).

Figure 15 shows the friction factor (*f=T/(RW)*) derived from the startup torque versus specific load for a bearing with two shim configurations. The original bearing shows a friction coefficient ~ 0.30 that is largely constant with increasing loads. The friction factor for the bearings with shims is higher than the original bearing and increases with shim thickness while decreasing with increasing loads. Note that at *W/(LD)*~20 kPa, the friction factor for the bearing with 50 μm shims is 40% higher than the original bearing.

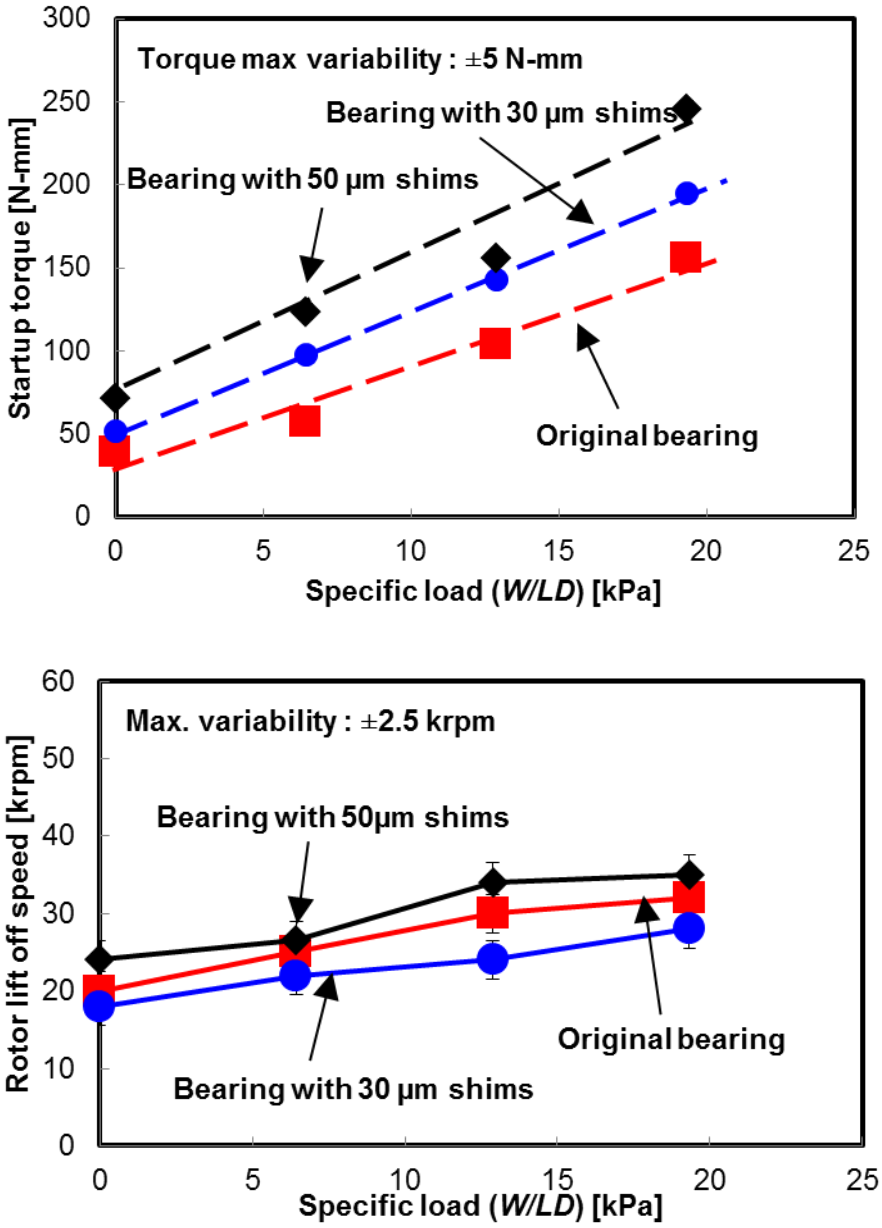

Figure 14. (top) Breakaway torque and (Bottom) lift off speed versus specific load (*W/(LD)*) for original BFB and bearing with shims of thickness 30 µm and 50 µm.

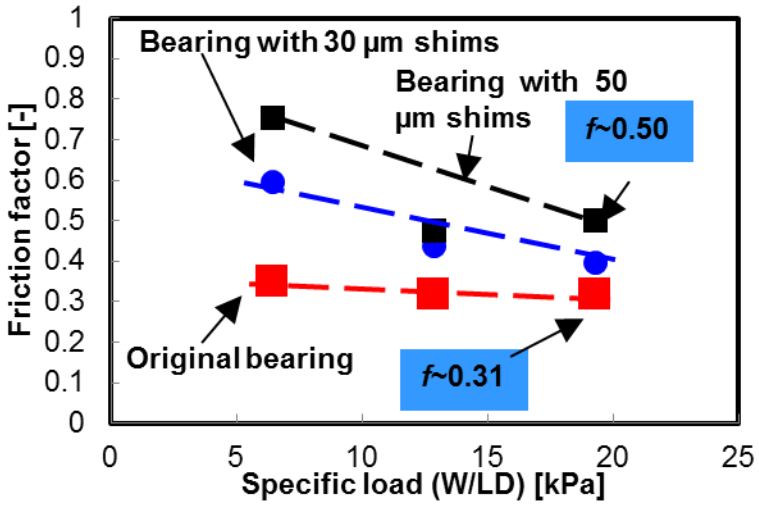

Figure 15. Breakaway dry friction factor versus specific load (W/(LD)) for original BFB and bearing with shims of thickness 30 μm and 50 μm.

Comparison of two methods of identifying the drag torque due to friction (breakaway torque)

Measuring the drag torque (T) during a rotor speed startup test and the breakaway torque ($T_{breakaway}$) via a torque screwdriver presents two methods of identifying the drag torque due to rubbing contact that a bearing experiences. Clearly, recording the breakaway torque with a simple torque screwdriver is simpler and easier than driving the system to spin the rotor.

Figure 16 presents the bearing start up drag torque (T) and breakaway torque ($T_{breakaway}$), and the friction factor from the startup torque and breakaway torque versus specific load for the original bearing (without shims).

The drag torque (T) during a rotor startup and the torque from the torque screwdriver dramatically increase with load ($W/(LD)$). In fact, the startup drag torque (T) at the highest load ($W/(LD)$~20 kPa) is 75% larger than the startup drag torque at $W/(LD)$~0 kPa.

The maximum variance in the torque measurements during rotor speed startup is ±5 N-mm. Interestingly, the startup friction factor ($f=T/(RW)$~0.3) remains constant with respect to specific load.

Note the friction factors identified by each method are quite similar for low loads (<10 kPa); however the difference in the measurements grows with load. At specific loads $W/(LD)$>10 kPa, the friction factor ($f=T/(RW)$) during rotor speed startup is significantly higher (33%) than the breakaway friction factor ($f_{breakaway}=T_{breakaway}/RW$).

Tests with rotor speed at $W/(LD)$~20 kPa occurred after approximately 200 cycles of rotor speed startup and shut down. Post test inspection shows visible wear after only ~ 100 cycles of rotor speed startup and shut down procedures (consult Appendix B for details). Visible surface wear is likely to increase the friction factor. For example, Ref. [28] notes a 40% increase in the drag torque (and friction factor) due to surface wear and loss the of protective MoS2 coating in a (metal mesh) foil bearing.

The friction factor (f) for a shimmed bearing derived from both measurement methods (driving the TC shaft to rotate and measuring the breakaway torque) agree reasonably well at low loads ($W/(LD)$<20 kPa). However, the measurements from the two methods differ by 30% at $W/(LD)$~20 kPa due to surface wear from extensive testing.

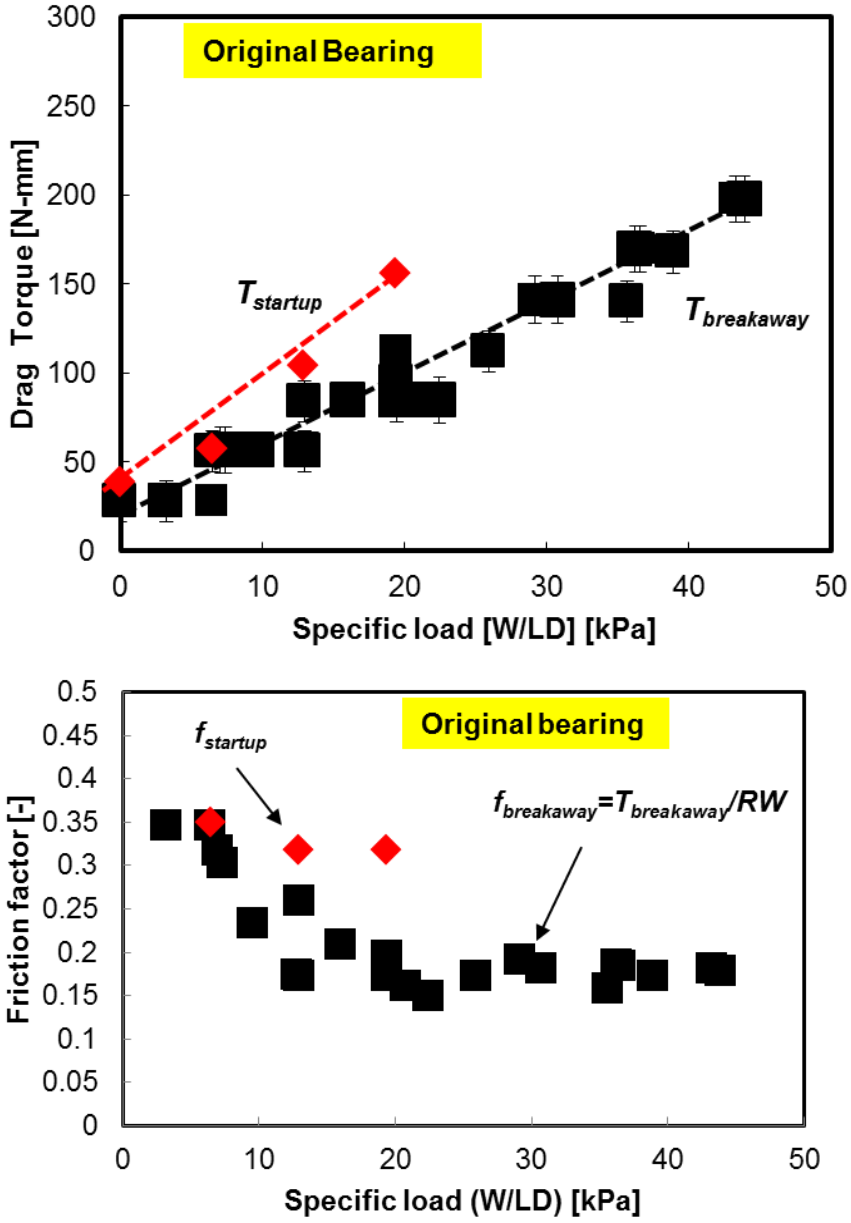

Figure 16. (top) Bearing drag torque(*T*) during speed startup and breakaway **torque ($T_{breakaway}$) and (bottom) friction factor calculated from the start up drag torque (*f*) and breakaway torque ($f_{breakaway}$) versus specific load (*W/(LD)*) for the original bearing (without shims).**

CHAPTER IV

IDENTIFICATION OF ROTORDYNAMIC FORCE COEFFICIENTS IN A BFB WITH AND WITHOUT SHIMS*

Bearing stiffness and damping coefficients largely determine the rotordynamic performance of BFB supported rotor-bearing systems. This section presents an experimental facility and parameter identification procedure for determining BFB force coefficients. A discussion follows on the effect of rotor speed (Ω), excitation frequency (ω), and on the force coefficients of a BFB assembled with various shim thicknesses (t_s).

Experimental facility

In 1966, Glienicke [29] develops the first "floating" bearing test rig to measure the stiffness and damping coefficients of various oil lubricated bearings (cylindrical, two-lobed, pocket bearings) as they operate on a spinning shaft (up to 10 krpm). The test rig features the ability to apply static (up to 5 MPa) and periodic (single frequency) dynamic loads (up to 5000 N in amplitude) simultaneously to the test bearing as it operates "floats" atop a spinning shaft. Load versus deflection curves are also obtained. The author presents a thorough comparison of the performance (stiffness, damping, film thickness, static load behavior etc.,) of 4 different types of oil lubricated bearings under various operating conditions (i.e., static load, excitation frequencies). The test rig described in Ref. [29] is the precursor and basis for the test rig used to conduct dynamic load tests in this work.

Figure 4 shows the experimental setup for the dynamic load tests. The test rig is the same as used in Ref. [30]. The rig consists of a ball bearing supported turbocharger (TC) capable of shaft speeds up to 80 krpm. The compressor impeller end of the turbocharger

* Portions reprinted with permission from " Measurement of drag torque and lift off speed and rotordynamic force coefficients in a shimmed BFB," by San Andrés, L., and Norsworthy, J., 2014, (Pennacchi P (Ed.): Proceedings of the 9th International Conference on Rotordynamics, Copyright (2015) Springer. All rights reserved).

is removed and replaced with an exposed over hanging shaft. A hollow journal (36.5mm OD) is press fit onto the shaft and secured with a nut. The test BFB is placed on the journal.

A squirrel cage, attached to a positioning table, supports the test bearing and helps to reduce misalignment of the bearing with the journal during loading. Two eddy current sensors record FB motions relative to the shaft, two accelerometers (mounted to the bearing cartridge) measure absolute acceleration, and dynamic loads cells record the excitation force. Two orthogonally positioned shakers (45° away from the vertical plane) apply sine sweep load excitations to the BFB and the resulting motions are recorded to extract dynamic force coefficients.

An in house computer data acquisition interface controls the dynamic load characteristics (amplitude and frequency) while recording bearing relative displacements, acceleration, and applied loads.

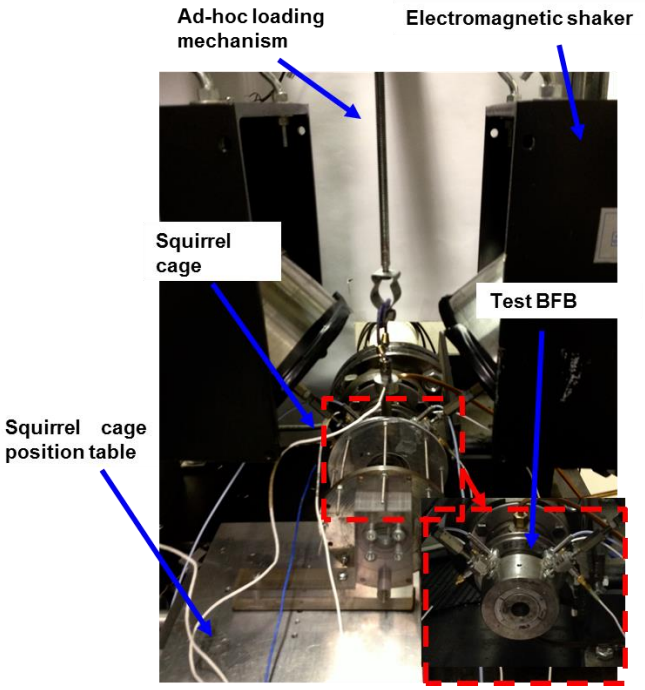

Figure 17. Experimental setup for dynamic load tests.

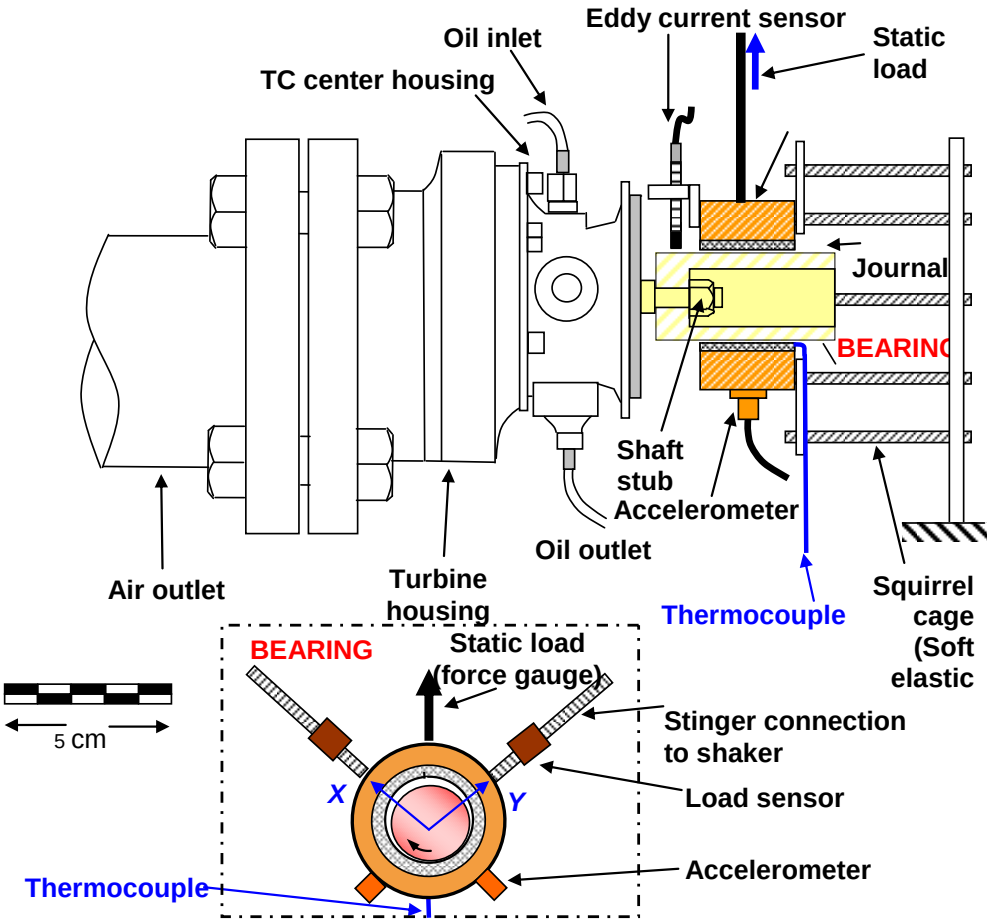

Figure 18. Schematic view of a test rig to apply dynamic loads to an airborne BFB [30].

In the various tests, three stainless steel shims, placed 120° apart from each other, are installed behind the bump foil strip and glued to the bearing inner diameter, as seen in Figure 4. One shim locates 45° from the fixed end top foil and acts as a reference for the position of the other shims. Each shim has an adhesive coating on one side that affixes it to the inner diameter of the bearing housing.

Parameter identification procedure

Figure 19 presents a schematic view of the test system used for parameter identification. The parameter identification methodology follows that advanced in Refs. [21,29], and is described below.

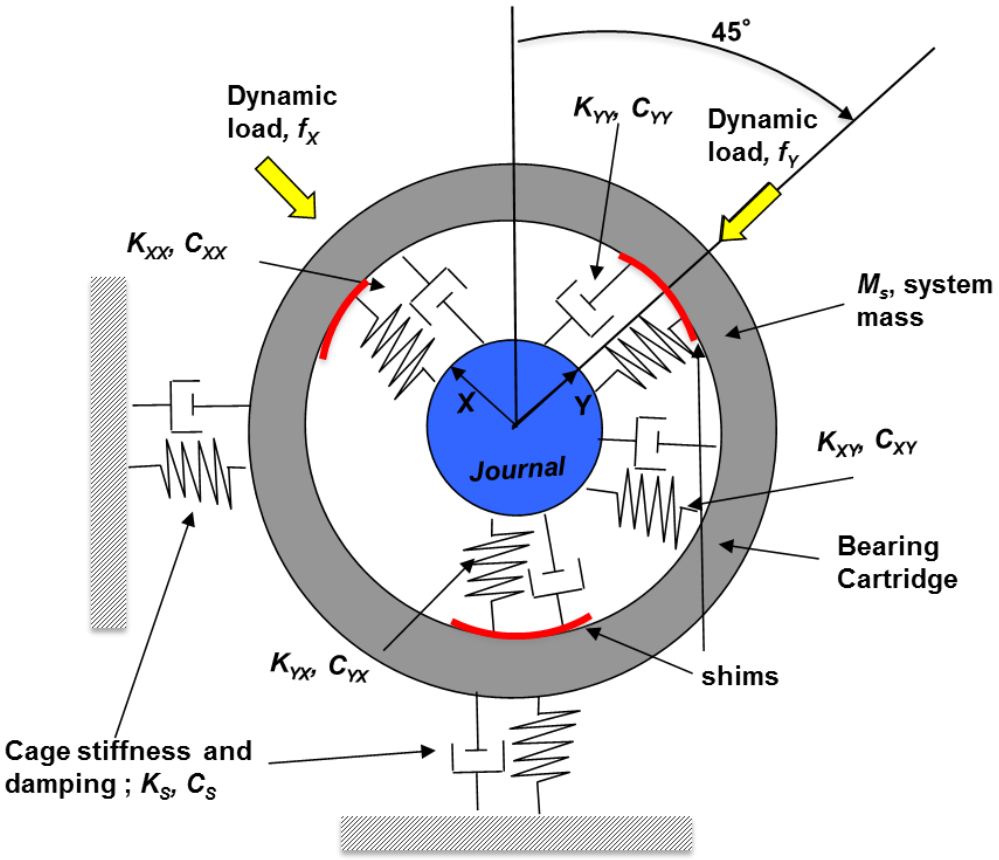

Figure 19.Schematic view representation of a BFB with idealized mechanical parameters [30].

Electromagnetic shakers apply dynamic loads with a sine sweep wave shape mathematically described as

$$F_{(t)} = [F_o + \Delta F\, t] \sin [(\omega_o + \Delta\omega\, t)\, t] \qquad (2)$$

where F_o is a steady load amplitude, ω_o is the initial excitation frequency, and $\Delta\omega$ and ΔF designate the rates of increase in frequency and dynamic load, respectively. The temporal changes in dynamic load (ΔF=375 N/s) and excitation frequency ($\Delta\omega$=943 rad/s/s) are user defined, selected to maintain a constant bearing displacement amplitude relative to the shaft [21,29]. Note also that $\Delta F/F_o$=3 1/s, and $\Delta\omega/\omega_o$=4.7 1/s, where F_o and ω_o are the initial dynamic load amplitude and initial excitation frequency, respectively (i.e., are constants in Eq.2) .

Electromagnetic shaker loads, F_X and F_Y, excite the test bearing producing its motion. The TC journal on the flexible shaft also displaces when a dynamic load is applied to the bearing. Define (x, y) and (x_j, y_j) as the absolute bearing and journal displacements, respectively. Hence, $(x', y') = (x, y) - (x_j, y_j)$ are the bearing displacements relative to the journal.

The effective system mass $(M_S)_{X,Y}$, cage stiffness $(K_S)_{X,Y}$ and cage damping coefficients $(C_{S_X})_{X,Y}$ are estimated from impact loads prior to the experiments. Consult Appendix D for details on the identification of the parameters.

The equation of motion for the bearing cartridge is

$$\begin{bmatrix} M_{S_X} & 0 \\ 0 & M_{S_Y} \end{bmatrix}\begin{Bmatrix} \ddot{x} \\ \ddot{y} \end{Bmatrix} + \begin{bmatrix} C_{S_X} & 0 \\ 0 & C_{S_Y} \end{bmatrix}\begin{Bmatrix} \dot{x} \\ \dot{y} \end{Bmatrix} + \begin{bmatrix} K_{S_X} & 0 \\ 0 & K_{S_Y} \end{bmatrix}\begin{Bmatrix} x \\ y \end{Bmatrix} + \begin{bmatrix} C_{XX} & C_{XY} \\ C_{YX} & C_{YY} \end{bmatrix}\begin{Bmatrix} \dot{x}' \\ \dot{y}' \end{Bmatrix} + \begin{bmatrix} K_{XX} & K_{XY} \\ K_{YX} & K_{YY} \end{bmatrix}\begin{Bmatrix} x' \\ y' \end{Bmatrix} = \begin{Bmatrix} F_X \\ F_Y \end{Bmatrix} \tag{3}$$

where $(K_{\alpha\beta}, C_{\alpha\beta})_{\alpha\beta=X,Y}$ are frequency dependent stiffness and damping coefficients.

The time domain excitation forces and resulting BFB motions are transformed into the frequency domain by applying the Discrete Fourier Transform (DFT), i.e.,

$$\bar{F}_{X(\omega)} = DFT\left(F_{X(t)}\right) \; ; \; \bar{x}'_{(\omega)} = DFT\left(x'_{(t)}\right) \; ; \; \bar{A}_{X(\omega)} = DFT\left(\ddot{x}_{(t)}\right) \tag{4}$$

and likewise for displacements and other variables along the Y direction. Recall that the DFT[$x'_{(t)}$]=$j\omega\,\bar{x}'_{(\omega)}$, where $j = \sqrt{-1}$.

Also

$$DFT\left[\dot{x}_{(t)}\right]=\frac{\bar{A}_{X(\omega)}}{j\omega},\ DFT\left[x_{(t)}\right]=-\frac{\bar{A}_{X(\omega)}}{\omega^2} \tag{5}$$

A frequency domain analysis of the equations of motion for the test bearing yields the direct and cross-coupled stiffness and damping coefficients. The frequency domain equation of motion is

$$\begin{bmatrix} K_{XX}+j\omega C_{XX} & K_{XY}+j\omega C_{XY} \\ K_{YX}+j\omega C_{YX} & K_{YY}+j\omega C_{YY} \end{bmatrix}\begin{bmatrix} \bar{x}'_{(\omega)} \\ \bar{y}'_{(\omega)} \end{bmatrix}=\begin{bmatrix} \bar{G}_{X(\omega)} \\ \bar{G}_{Y(\omega)} \end{bmatrix}$$
$$=\begin{bmatrix} \bar{F}_{X(\omega)} \\ \bar{F}_{Y(\omega)} \end{bmatrix}-\begin{bmatrix} M_{s_X}+C_{S_X}/j\omega-K_{S_X}/\omega^2 \\ M_{S_Y}+C_{S_Y}/j\omega-K_{S_Y}/\omega^2 \end{bmatrix}\begin{bmatrix} \bar{A}_{X(\omega)} \\ \bar{A}_{Y(\omega)} \end{bmatrix} \tag{6}$$

where $\left(\bar{x}'_{(\omega)},\bar{y}'_{(\omega)}\right)$ are the DFTs of the bearing displacements (x', y') relative to the journal, $\left(\bar{F}_{X(\omega)},\bar{F}_{Y(\omega)}\right)$ are the DFTs of the excitation forces, and $\left(\bar{A}_{X(\omega)},\bar{A}_{Y(\omega)}\right)$ are the DFTs of the bearing absolute accelerations.

The compact form of the equation of motion in the frequency domain equation is

$$\begin{bmatrix} H_{XX} & H_{XY} \\ H_{YX} & H_{YY} \end{bmatrix}\begin{bmatrix} \bar{x}'_{(\omega)} \\ \bar{y}'_{(\omega)} \end{bmatrix}=\begin{bmatrix} \bar{G}_{X(\omega)} \\ \bar{G}_{Y(\omega)} \end{bmatrix} \tag{7}$$

Where $\mathbf{H}_{(\omega_k)}=(\mathbf{K}+j\omega_k\mathbf{C})$ is the matrix of bearing impedance coefficients at the discrete excitation frequencies (ω_k).

Two independent (load) excitations are required to determine the eight frequency dependent force coefficients. In practice, the bearing is excited by loads of the form $\mathbf{F}^X=[F_X\ 0]^T$, and $\mathbf{F}^Y=[0\ F_Y]^T$, respectively. The equations for the two sets of dynamic load excitations become

$$\begin{bmatrix} H_{XX} & H_{XY} \\ H_{YX} & H_{YY} \end{bmatrix}\begin{bmatrix} \bar{x}'^{X}_{(\omega)} & \bar{x}'^{Y}_{(\omega)} \\ \bar{y}'^{X}_{(\omega)} & \bar{y}'^{Y}_{(\omega)} \end{bmatrix}=\begin{bmatrix} \bar{G}^{X}_{X(\omega)} & \bar{G}^{Y}_{X(\omega)} \\ \bar{G}^{X}_{Y(\omega)} & \bar{G}^{Y}_{Y(\omega)} \end{bmatrix} \tag{8}$$
$$\mathbf{H}\bar{\mathbf{z}}=\bar{\mathbf{G}}$$

The first column in the $\bar{\mathbf{z}}$ matrix contains the relative bearing displacements in the *X* and *Y* axis as an electromagnetic shaker apply dynamic loads along the *X* axis (superscripts),

while the second column is the bearing displacements as the electromagnetic shakers excite the *Y* axis.

At each frequency (ω_k), the bearing impedance coefficients are calculated as $\mathbf{K}_{(\omega_k)} + j\omega_k \mathbf{C}_{(\omega_k)} = \mathbf{H}_{(\omega_k)} = \overline{\mathbf{G}}_{(\omega_k)} \overline{\mathbf{z}}^{-1}_{(\omega_k)}$, and the bearing force coefficients are extracted from

$$\{K_{\alpha\beta}\}_{(\omega_k)} = \mathrm{Re}(\{H_{\alpha\beta}\}_{\omega_k}), \quad \{C_{(\omega_k)}\}_{\alpha\beta} = \frac{\mathrm{Im}(\{H_{\alpha\beta}\}_{\omega_k})}{j\omega_k} \quad \alpha\beta = X, Y \tag{9}$$

The bearing loss factor is derived by equating mechanical energy dissipated by the structure to energy dissipated via viscous forces i.e., $E_v = \oint_t^{t+T} \dot{\mathbf{z}}^{\mathbf{T}} \mathbf{C}\, \dot{\mathbf{z}}\, dt = E_m = \oint_t^{t+T} \dot{\mathbf{z}}^{\mathbf{T}} \frac{\gamma}{\omega} \mathbf{K}\, \dot{\mathbf{z}}\, dt$, where $\dot{\mathbf{z}}$ is a vector of bearing velocities, *T* is the period of motion, [18]. Note that the proportional structural damping model is $C\omega = \gamma K$ [18], where *C*, and *K* are damping and stiffness coefficients. The foil bearing loss factor (γ), evidencing mechanical energy dissipation, as developed in Refs. [21,30] for circular orbits is

$$\gamma = \frac{\omega\left(C_{XX} + C_{YY}\right)}{K_{XX} + K_{YY}} \tag{10}$$

Define a frequency averaged loss factor ($\bar{\gamma}$) as

$$\bar{\gamma} = \frac{1}{\omega_2 - \omega_1} \int_{\omega_1}^{\omega_2} \gamma \, d\omega \tag{11}$$

where ω_1 and ω_2 are arbitrary frequencies, respectively. The standard deviation of the frequency averaged loss factor (σ) is

$$\sigma = \sqrt{\frac{\sum (\gamma - \bar{\gamma})}{n-1}} \tag{12}$$

where *n* is the number of tests samples considered for the average process.

Data analysis

An in-house DAQ program generates ten load excitation waveforms each lasting 0.2 s, and records 4,096 data samples of force, bearing displacement, and acceleration. The sampling rate is 20,480/sec for each waveform, thus 40,960 data samples (for ten waveforms) are collected.

Computational software processes the BFB response motions, applies the DFT transforming the time domain data into the frequency domain, and extracts the force coefficients according to the above procedure.

Note that a coordinate transformation[9] is used to determine the force coefficients with respect to a coordinate system ($\underline{X}$, $\underline{Y}$) where $\underline{X}$ is parallel to the vertical plane (the static load direction) and $\underline{Y}$ is horizontal. The transformation allows the knowledge of the bearing force coefficients to be understood with respect to the direction of static load ($\underline{X}$).

Figure 20 presents the sine sweep load excitation waveforms (200-400Hz), applied along the *X* and *Y* directions. Note that more mechanical energy is required to produce the same displacement amplitudes at higher frequencies, thus the dynamic load is controlled (amplitude typically increases with excitation frequency) to maintain a constant bearing displacement amplitude (relative to the journal) across the excitation frequency range.

---

[9] For example, the stiffness matrix **K** for the *X*,*Y* coordinate system takes the form $\mathbf{K}=\mathbf{P}\underline{\mathbf{K}}\mathbf{P}^{T}$, where the coordinate transformation matrix $\boldsymbol{P}=\begin{bmatrix}\cos(\varphi) & \sin(\varphi)\\ -\sin(\varphi) & \cos(\varphi)\end{bmatrix}$, where φ is the angle from the $\underline{Y}$ axis to the *Y* axis. A similar method is employed in Ref. [30].

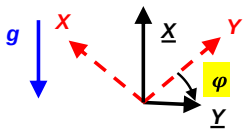

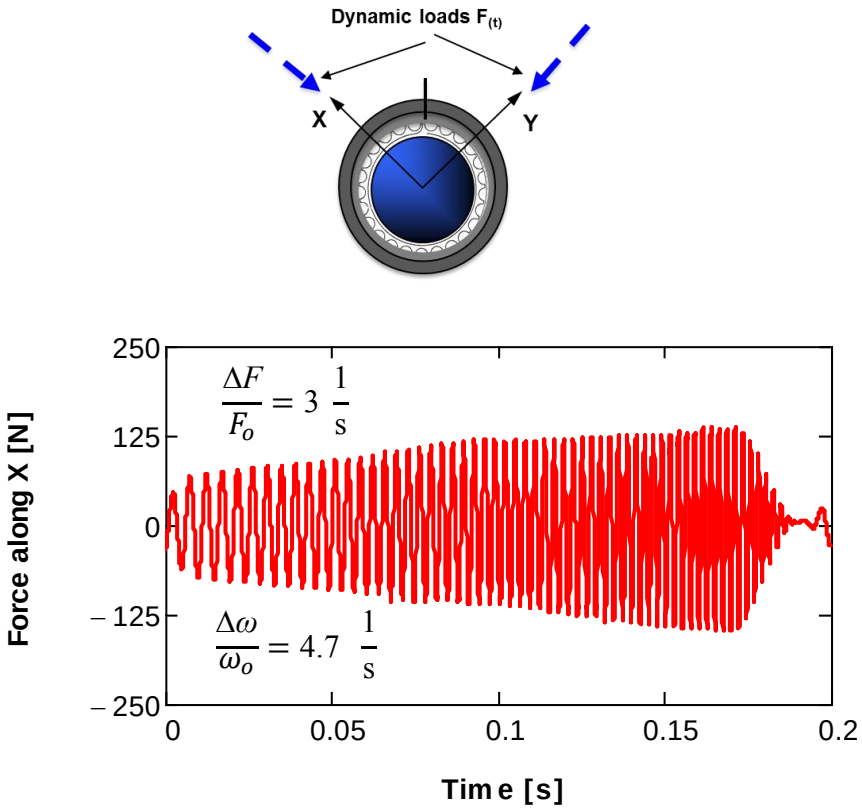

Figure 20. Typical dynamic excitation forces exerted along the *X* direction. Sine sweep loads 200-400Hz. Specific load ~ 14.3 kPa. Stationary journal.

Figure 21 presents the average (of 10 excitation waveforms) DFT amplitudes of the dynamic loads (*X* and *Y* directions) versus excitation frequency. The DFT amplitudes of the force are smaller than the time domain amplitudes. The DFT amplitude of the excitation forces is reduced in magnitude because a full period (at each frequency) is not sampled [30]. In a sine sweep wave form, the excitation frequency increases before a full period of motion is recorded. Note that Ref. [30] reports similar results.

Note, in Figure 21, that the amplitudes of the forces along the *X* and *Y* directions are not equal. To maintain a given displacement amplitude, a larger force is typically applied along the *X* axis than along the *Y* axis. This is due to differing bearing stiffness $K_{YY} \neq K_{XX}$.

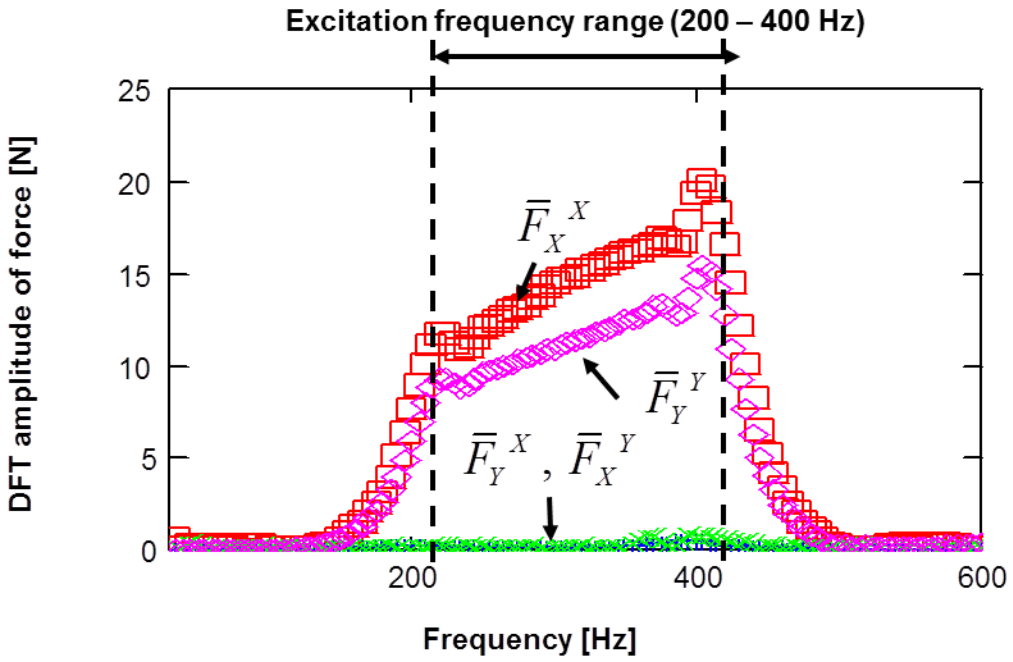

Figure 21. DFT amplitude of applied forces versus frequency. Sine sweep 200-400Hz. Average of 10 excitations. Stationary journal.

Figure 22 shows the bearing displacements relative to the shaft, *X* and *Y* directions, due to the applied dynamic loads. The ($\bar{x}'^X$, $\bar{y}'^Y$) bearing displacements are maintained at ~20 μm, while the cross directional displacements ($\bar{x}'^Y$, $\bar{y}'^X$) are ~7 μm, due to the motion of the flexible rotor supporting the bearing. For completeness Appendix E presents the bearing motion measurements with journal rotation at 50 krpm.

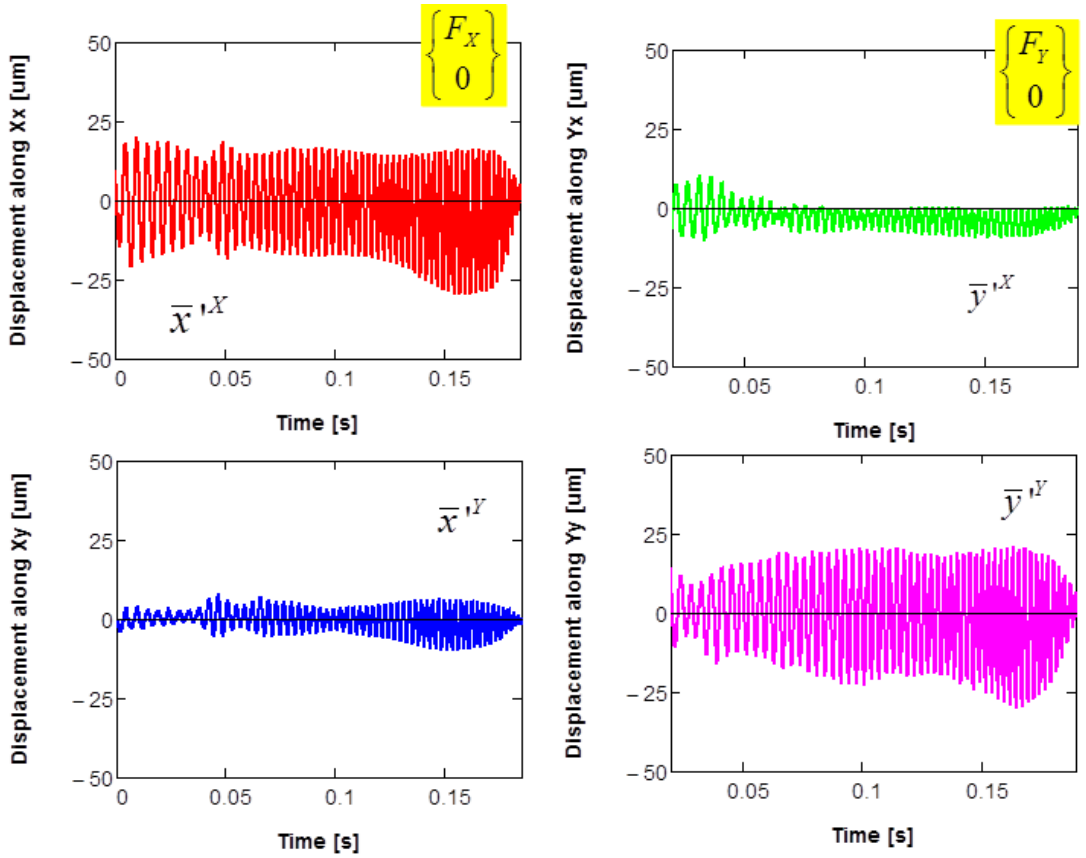

(a) F_X, F_Y=0 **(b) F_X=0, F_Y**

Figure 22. Direct (top) and cross directional (bottom) bearing relative displacements along *X* and *Y* directions. Applied specific load *W/(LD)*~ 27 kPa. Stationary journal.

Figure 23 shows the DFT amplitudes of the bearing displacements (relative to the journal). The direct displacements ($\bar{x}'^X$, $\bar{y}'^Y$) are approximately constant over the excitation frequency range (200-400 Hz). Note that the time domain direct displacements amplitudes ($\bar{x}'^Y$, $\bar{y}'^X$) are ~20 μm, while the frequency domain displacement amplitudes are ~3 μm.

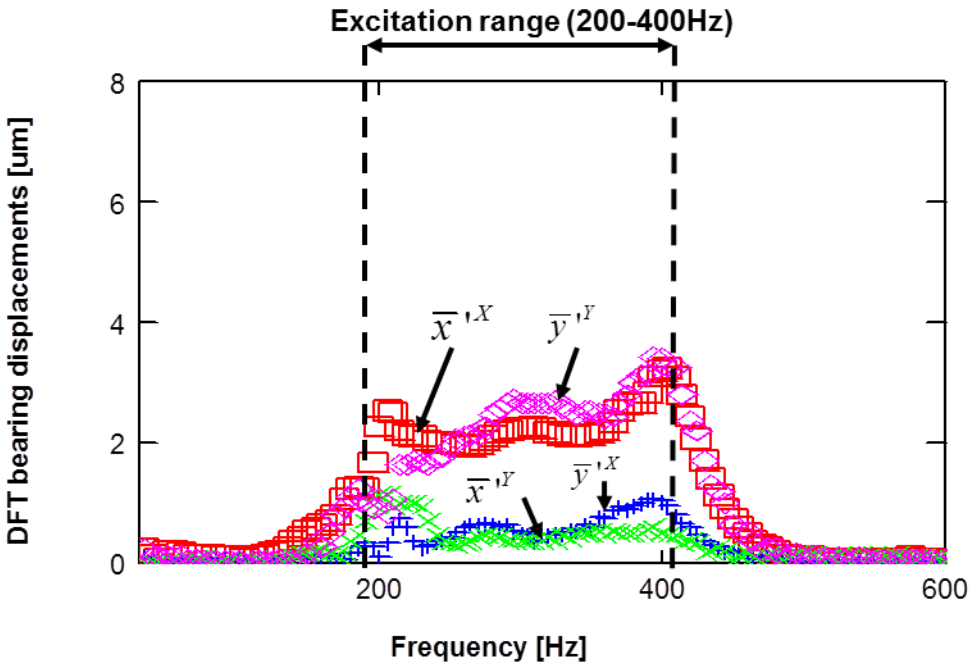

Figure 23. Average DFT amplitude of bearing displacements versus frequency. Sine sweep 200-400 Hz. Average of 10 excitations. Stationary journal. Specific load ~ 27 kPa.

Figure 24 shows the DFT amplitude of the bearing accelerations, X and Y directions. The bearing accelerations $(\bar{A}_X^X,\ \bar{A}_Y^Y)$ increase with excitation frequency in similar fashion to the dynamic excitation forces. Note that the cross accelerations $(\bar{A}_X^Y,\ \bar{A}_Y^X)$ are small.

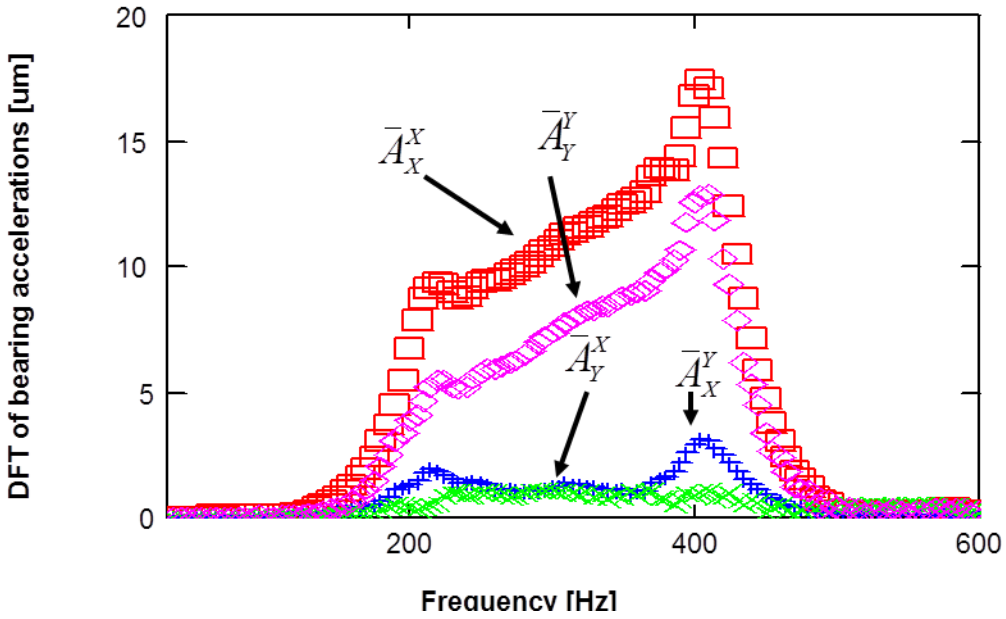

Figure 24. Average DFT amplitude of bearing absolute accelerations versus frequency. Sine sweep 200-400Hz. Average of 10 excitations. Stationary journal. Specific load of 27 kPa.

Force coefficients for the original BFB (without shims)

During full gas film operation (with journal speed), the force coefficients of the gas film act in series with the bump foil structure. This section discusses the force coefficients of a BFB, without shims and with shims, with a stationary journal and then operating with a journal speed of ~50 krpm. Over the course of a 30s test, the temperatures of the bearing cartridge and test shaft rise ~ 30°C. Once the gas film forms, separating the shaft from the top foil, the bearing cartridge and test shaft temperatures[10] stabilize around 48°C and cease to increases further.

Note that as the temperature of the gas lubricant increases so does its viscosity. Ref. [13] shows that the BFB stiffness decreases with large increases in the bearing temperature (up to 188°C) due to a reduction in the elastic modulus of the bump foil and

[10] The shaft and bearing cartridge temperatures are measured via an infrared thermometer (uncertainty: ±0.5°C).

top foil strips. Note that the test shaft experiences thermal and centrifugal growth which decreases the bearing clearance, thereby affecting the bearing force coefficients, as well.

All experimental results reported in this section correspond to a dynamic displacement amplitude of 20 μm and under a static specific load $W/(LD)$~ 14.3 kPa.

Figure 25 shows the stiffness coefficients (direct and cross coupled) for the original bearing, without journal rotation and with journal rotation (~50 krpm, 833 Hz). The cross coupled stiffness coefficients ($\underline{K}_{XY}$, K_{YX}) are small for both conditions, with and without journal rotation. The direct stiffnesses ($\underline{K}_{XX}$, $\underline{K}_{YY}$) increase with excitation frequency and are largely the same for operation without or with journal rotation. The ~30°C temperature rise has a minimal effect on the bearing stiffness coefficients, as these coefficients are largely the same for operation with and without journal rotation. Ref. [17] reports the structural stiffness (no journal rotation) due to increasing static loads for the original bearing. At a static deflection of ~ 20 μm, Ref. [17] reports a structural stiffness of ~ 1.01 MN/m, which is in good agreement with K_{XX} ~1 MN/m at 250 Hz as estimated from the dynamic load tests. The presence of a gas film has little effect on the BFB stiffnesses; thus indicating that the stiffness of the bump foil structure dominates the bearing stiffness. The stiffness along the direction with a static load ($\underline{X}$) is only slightly higher than the stiffness along the $\underline{Y}$ i.e., $\underline{K}_{XX} \geq \underline{K}_{YY}$.

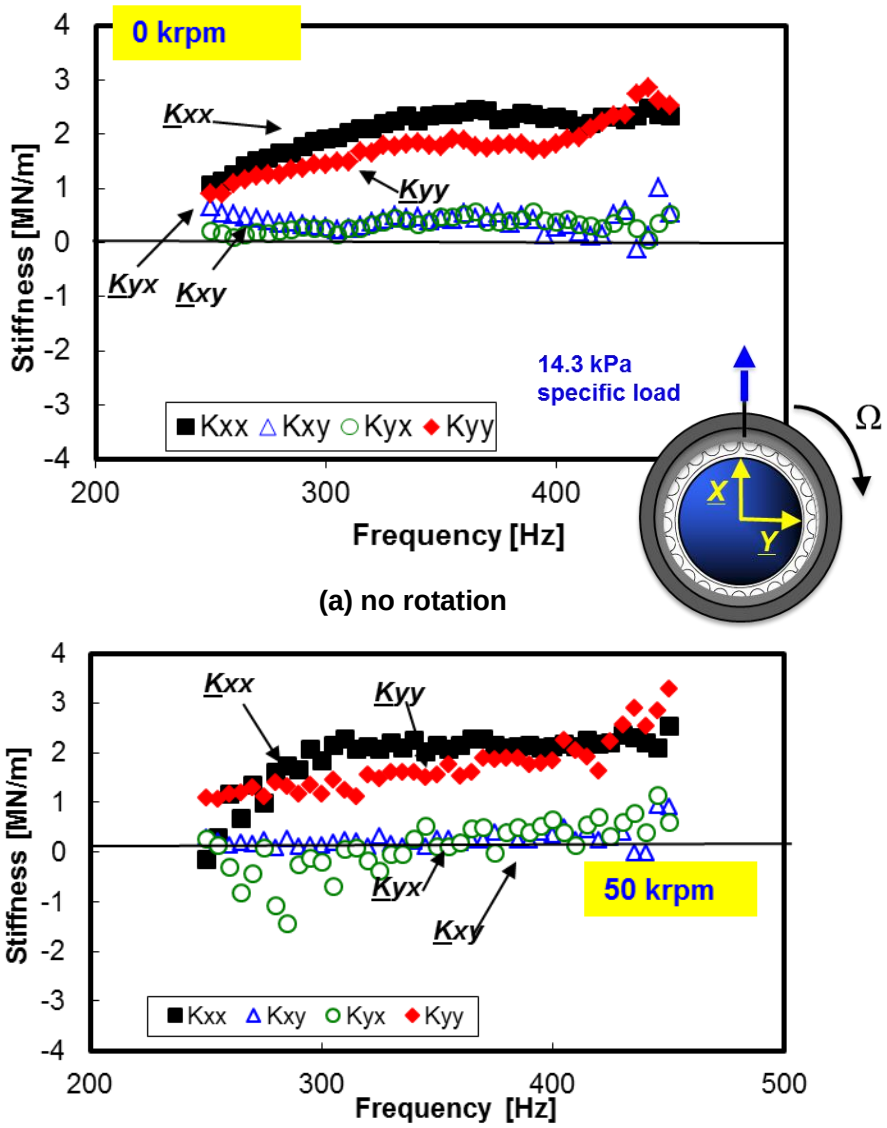

Figure 25. Stiffness coefficients $(\underline{K}_{\alpha\beta})_{\alpha\beta=\underline{X},\underline{Y}}$ versus excitation frequency for the original bearing (without shims). Operation under a specific load *W/(LD)*~14.3kPa. (a) no journal rotation and (b) with journal rotation (50 krpm) and. Dynamic sine sweep loads from 200-450Hz inducing a displacement amplitude of ~20 μm.

Figure 26 shows the viscous damping coefficients for the bearing without shims (a) stationary and (b) operating at 50 krpm. Interestingly, rotor speed has little effect on $\underline{C}_{XX}$,

while $\underline{C}_{YY}$ drops when the rotor spins (50 krpm). Note that the cross coupled damping coefficients ($\underline{C}_{XY}$, $\underline{C}_{YX}$) are lower than the direct ones, and decrease for conditions with journal rotation. Note the steep drop in $\underline{C}_{XX}$ with frequency below 300 Hz and recall that the viscous damping coefficient are inversely proportional to frequency [15], i.e., diminishing with frequency. Damping in the direction of the static load ($\underline{C}_{XX}$) decreases with increasing excitation frequency, while $\underline{C}_{YY}$ increases with frequency.

Figure 27 presents the loss factor (γ) versus excitation frequency for the original bearing operating without journal speed and with journal speed at 50 krpm (833 Hz). The bearing loss factor varies little with frequency above 300 Hz. At frequencies below 300 Hz, the large loss factor (γ>1) is due to the small stiffness coefficients (see Figure 24) arising from a displacement amplitude below 20 μm at frequencies ~200 Hz. The variation in the loss factor with frequency is due to the force coefficients which also vary with frequency. The bearing loss factor is averaged over frequencies ranging from 300 Hz to 400 Hz. The arbitrary frequency range selected for the average excludes large loss factors (>1) around 200-250 Hz. The average loss factor ($\bar{\gamma}$~0.47, σ=0.07) for the original bearing operating with journal speed is 23% lower than when the shaft is stationary ($\bar{\gamma}$~0.61, σ=0.07). Incidentally, the current tests show that the loss factor (γ) with shaft rotation is slightly lower than that without journal rotation, indicating that the bump foil structure dissipates less energy during full film operation.

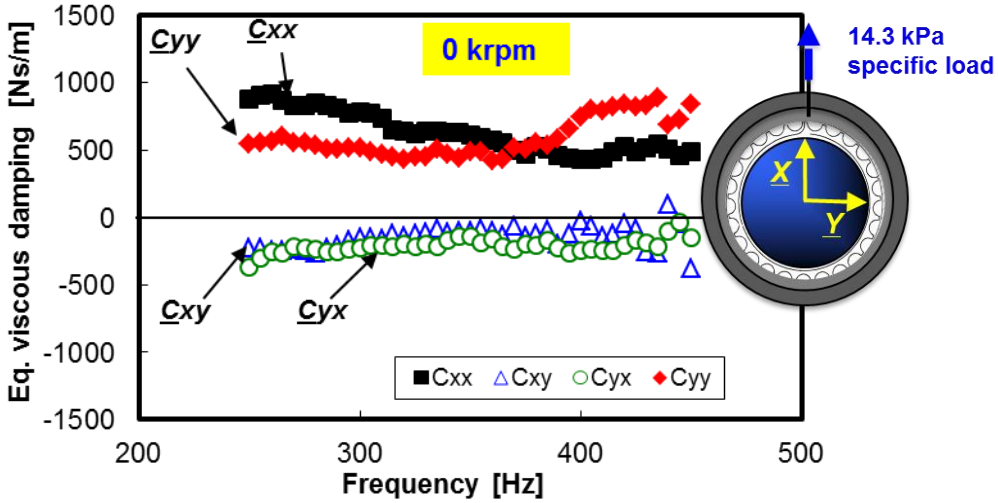

(a) no rotation

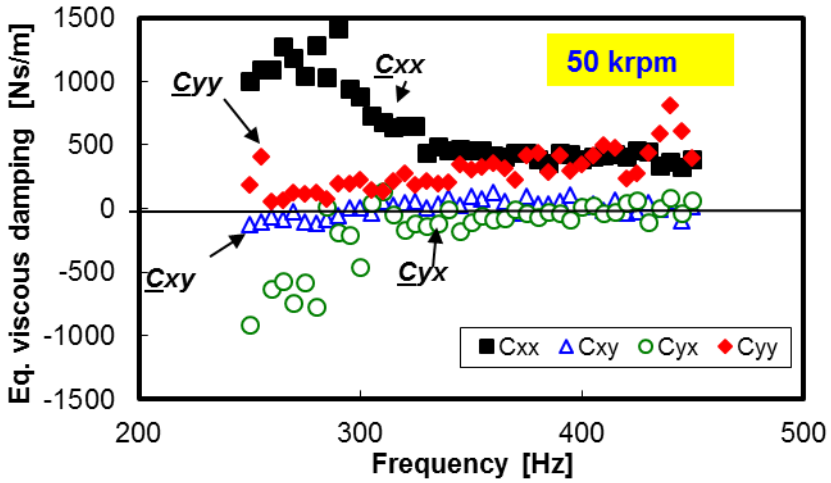

(b) 50 krpm (833 Hz)

Figure 26. BFB viscous damping coefficients ($(\underline{C}_{\alpha\beta})_{\alpha\beta=\underline{X},\underline{Y}}$) versus excitation frequency for the original bearing (without shims). (a) no journal rotation and (b) with journal rotation (50 krpm). Results for sine sweep loads from 200-450 Hz, displacement amplitude~ 20 μm, and a specific load *W/(LD)*~14.3kPa.

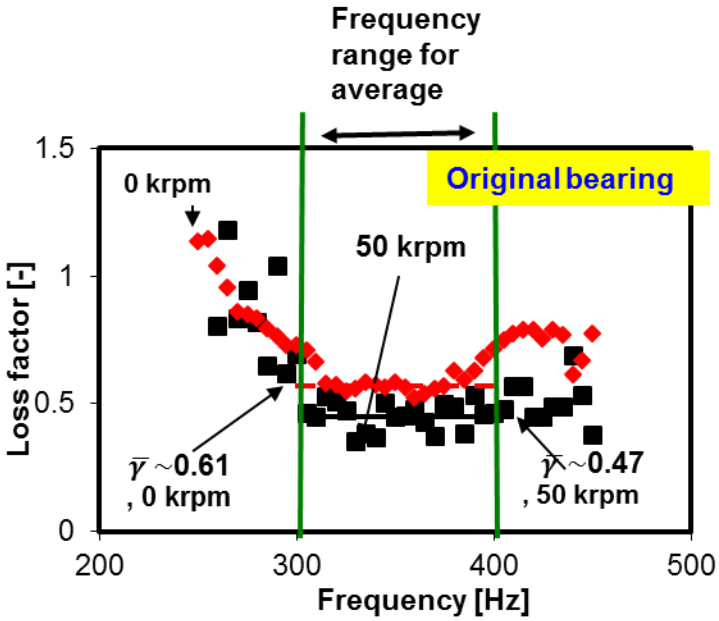

Figure 27. BFB material loss factor (γ) versus excitation frequency for the original bearing (without shims). No journal rotation and with journal rotation (50 krpm). Results for sine sweep loads from 200-450 Hz, displacement amplitude~ 20 μm, and a specific load *W/(LD)*~14.3kPa. Average loss factor calculated from 300 - 400 Hz

Ref. [17] presents a loss factor for the same bearing operating without journal rotation and under cyclical static loading (cycles of push and pull static loads). The loss factor obtained from the static loads (γ~0.07) is much lower than that of the bearing under dynamic loading (γ~0.61, σ= 0.07).

Under static loading, the bump foil strip deflects[11] up to 60 μm, at which the bump structure ceases to deflect further (essentially becoming rigid) and shows little material hysteresis (mechanical energy dissipation). The dynamic displacement amplitude during dynamic loading (~ 20 μm) is smaller than the maximum bump deflection due to static

[11] The static load results in Ref. [17] evidence the clearance region. At displacements larger than the bearing clearance, the bump foil strip deflects. Thus the deflection of the bump foil strip is estimated as the displacement minus the bearing clearance.

loads. Note from the loss factor formulation[12] due to static loads [17] that $\gamma \sim 1/X^2$ where X is the maximum bump deflection. Also note that the loss factor is derived from assuming circular motion orbits, while during the static load tests, the bearing motion is collinear with the applied static load.

In theory [31], the loss factor for a simple mechanical system is a unique structural property, and $\gamma \sim f$ or a static coefficient of friction μ.

Note that the dynamic displacement amplitude (20 μm) is small compared to the bearing radial clearance (120 μm). The force coefficients shown serve as a benchmark to determine the effect of shimming on the BFB force coefficients. The uncertainty in the bearing stiffness and damping coefficients is 0.08 MN/m and 80 Ns/m, respectively Consult Appendix C for details on the uncertainty analysis.

Force coefficients for a shimmed BFB

Figures 27 through 30 show the bearing force coefficients (stiffness and damping) for the BFB configured with shim thicknesses equal to 30 μm and 50 μm, and for operation with a stationary journal and with journal rotation at 50 krpm (833 Hz).

[12] Recall that for static loading $\gamma = E_{dis}/(\pi K_s X^2)$ [17], where E_{dis} is the dissipated mechanical energy, X is the displacement amplitude, and K_s is the bearing stiffness..

Figure 28 shows the stiffness coefficients for the bearing with 30 μm shims. The magnitudes of $\underline{K}_{XX}$ are comparable for operation with or without journal rotation, while $\underline{K}_{YY}$ is larger when the journal is stationary than when the journal is spinning. This indicates that rotational speed has a minimal effect on the $\underline{K}_{XX}$. However journal rotation reduces $\underline{K}_{YY}$. Note also that the stiffness coefficients of the BFB with 30 μm shims are roughly the same magnitude as those of the original bearing and show the same trend with respect to excitation frequency. Interestingly, $\underline{K}_{YY}$ of the bearing with 30 μm (stationary journal) is larger (15%) than that of the original bearing. The cross-coupled stiffnesses ($\underline{K}_{XY}$, $\underline{K}_{YX}$) are smaller than the direct stiffnesses and increase with shim thickness.

When there is no journal rotation and below 325 Hz, $\underline{C}_{YY} \approx \underline{C}_{XX}$.. Above 325 Hz, $\underline{C}_{YY} \geq \underline{C}_{XX}$. However, when there is journal rotation (50 krpm) and below 370 Hz, $\underline{C}_{YY} \leq \underline{C}_{XX}$. And above 370 Hz, $\underline{C}_{YY} \approx \underline{C}_{XX}$. $\underline{C}_{YY}$ drops more when there is journal rotation than without. Clearly rotor speed significantly lowers the damping along the horizontal axis ($\underline{Y}$). The direct damping coefficients of the bearing with 30 μm are slightly larger than those of the original bearing (operating at 50 krpm). Note that $\underline{C}_{YY}$ for the bearing with 30 μm shims (stationary journal) is 30% larger than that of the original bearing.

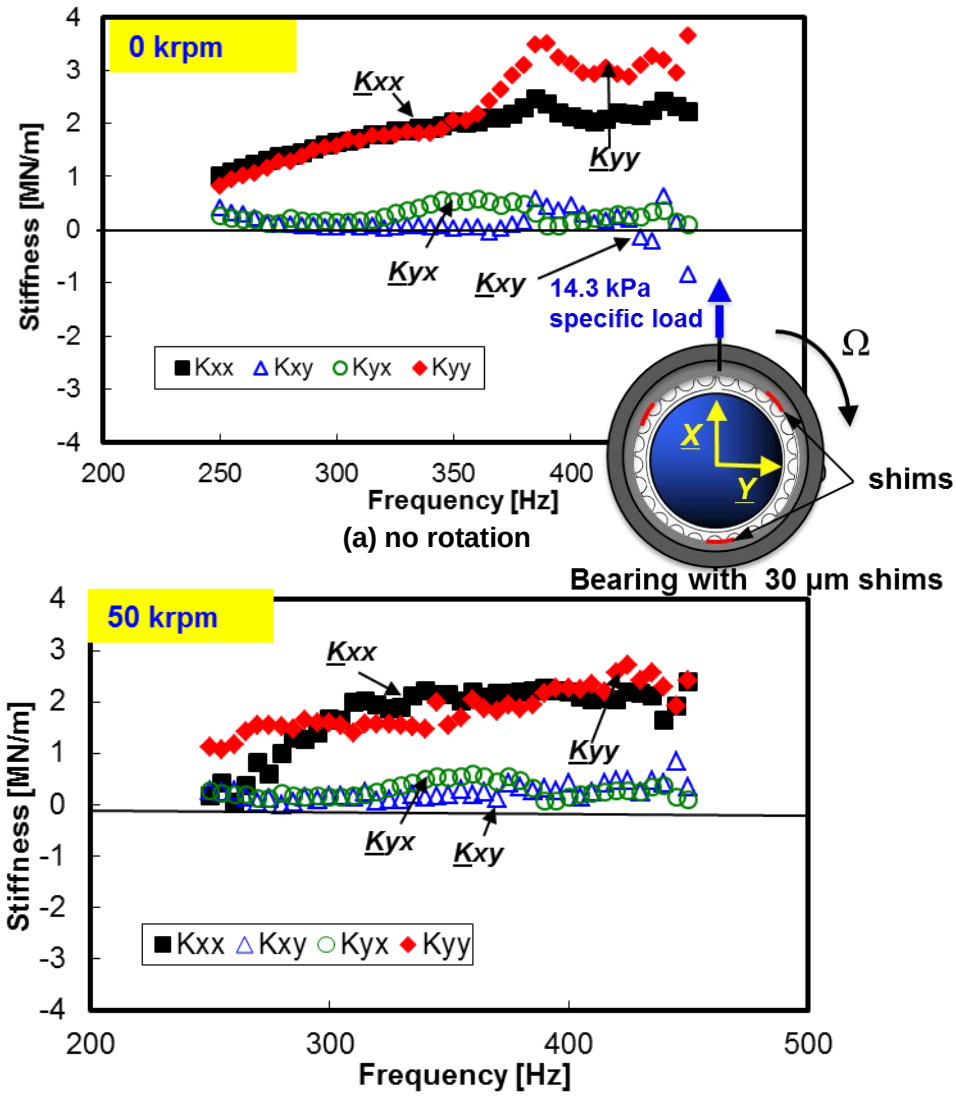

(a) no rotation

(b) 50 krpm (833 Hz)

Figure 28. BFB stiffnesses ($(\underline{K}_{\alpha\beta})_{\alpha\beta=\underline{X},\underline{Y}}$) versus excitation frequency for a bearing with 30 μm shims. (a) no journal rotation and (b) with journal rotation (50 krpm). Results for sine sweep loads from 200-450Hz, displacement amplitude~20 μm, and a specific load *W/(LD)*~14.3 kPa.

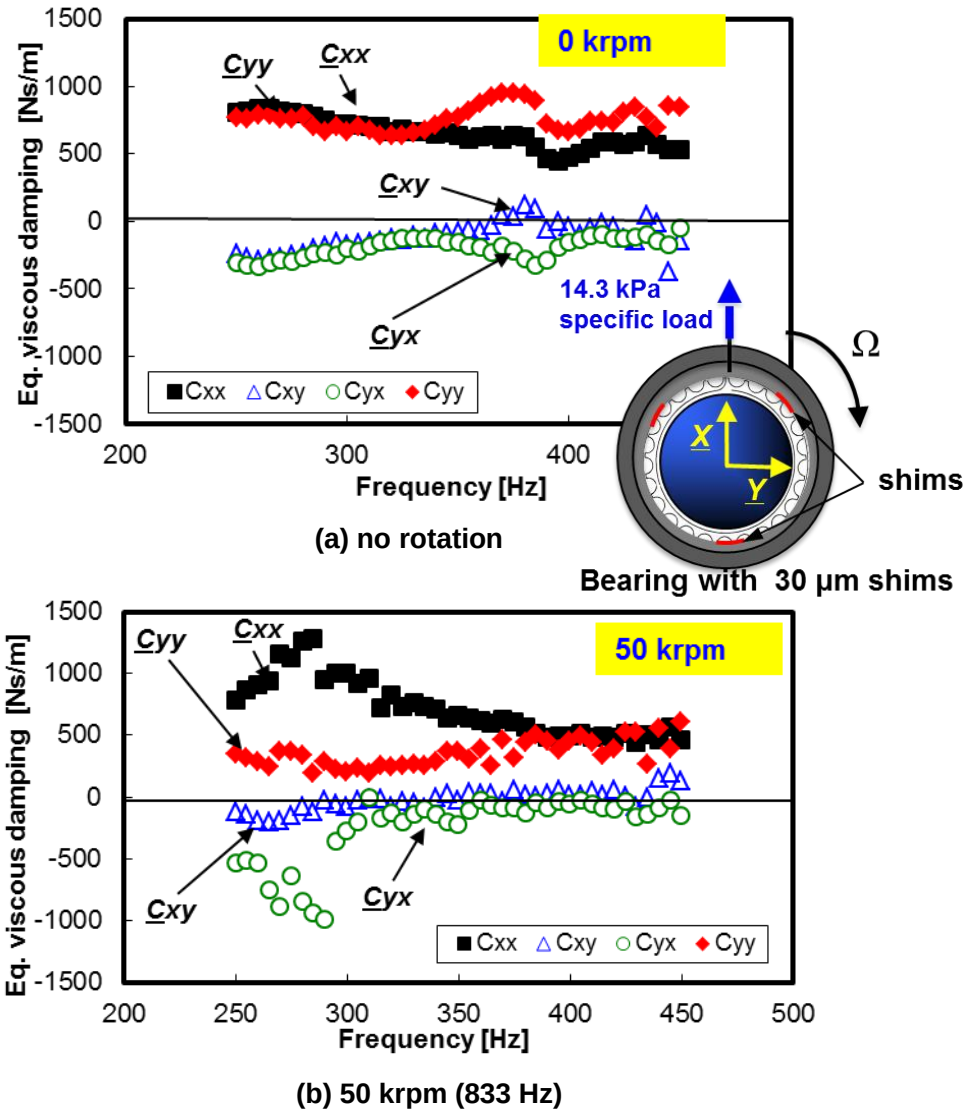

Figure 29. BFB damping coefficients ($\underline{C}_{\alpha\beta})_{\alpha\beta=\underline{X},\underline{Y}}$ versus excitation frequency for a bearing with 30 μm shims. (a) no journal rotation and (b) with journal rotation (50 krpm). Results for sine sweep loads from 200-450 Hz, displacement amplitude~20 μm, and a specific load *W/(LD)*~14.3 kPa.

The stiffness coefficients of the bearing with 50 μm shims (Figure 30) have similar magnitudes as those of the bearing with 30 μm shims. Note that $\underline{K}_{YY} \approx \underline{K}_{XX}$ across the excitation frequency range (stationary journal and with journal rotation). The direct stiffness coefficients are reduced slightly for operation at 50 krpm as oppose to when the

journal is stationary. When there is no journal rotation and below 370 Hz, $\underline{C}_{YY} \leq \underline{C}_{XX}$. Above 370 Hz, $\underline{C}_{YY} \approx \underline{C}_{XX}$, note that $\underline{C}_{XX}$ of the bearing with 50 μm shims is larger than that of the original bearing, while $\underline{C}_{YY}$ and the cross-coupled stiffness of the bearing with 50 μm shims are unremarkably different from those of the original bearing.

Figures 31 and 32 present the structural bearing loss factor (γ) versus excitation frequency for the BFB, without shims and with shims of thickness 30 μm and 50 μm, operating with and without journal speed. Table 2 presents the frequency averaged loss factor ($\bar{\gamma}$) and its standard deviations (σ) for a bearing without shims and with shims of 30 μm and 50 μm shims. The loss factor is averaged over an arbitrary frequency range from 300-400 Hz, thus delivering a representative loss factor $\bar{\gamma}$. The maximum variability in the bearing loss factor (γ) is ±0.05 (±10%).

Over a frequency range from 300-400 Hz and for dynamic motions of amplitude of 20 μm, the bearing with 50 μm shims offers an average loss factor ($\bar{\gamma}$) ~ 25% larger than that of the original bearing for operation with journal speed, and ~ 6% larger for operation without journal speed (see Table 2 for values).

Note that the loss factor for the bearing with 50 μm shims (operating at 50 krpm) shows large scatter which is reflected in its standard deviation (σ). Despite the large σ, the bearing with 50 μm shims operating at 50 krpm has a $\bar{\gamma}$ equal to or greater than that of the original bearing. The shimmed bearings have larger $\bar{\gamma}$ than the original bearing indicating that a shimmed BFB dissipates more mechanical energy. The increase in $\bar{\gamma}$ is likely due to an increase in the relative motion of the bumps against the top foil and bearing cartridge. The material loss factor for a shimmed BFB drops for operation with journal speed as opposed to conditions without journal speed.

Ref. [17] reports a loss factor γ~0.13-0.20 for the bearing with 50 μm shims (operating on a stationary journal) due to multiple cycles of static loading. The loss factor under static loading is much smaller (less than half) than the loss factor from dynamic loading. The differences in $\bar{\gamma}$ maybe due differences in the extent of deflection in the bump foil strip for the dynamic (~20 μm) and static load tests (~ 60 μm), and also

the differences in the bearing motion assumed for the calculation of the loss factor from static (collinear motion along the static load path) and dynamic (circular orbits) tests.

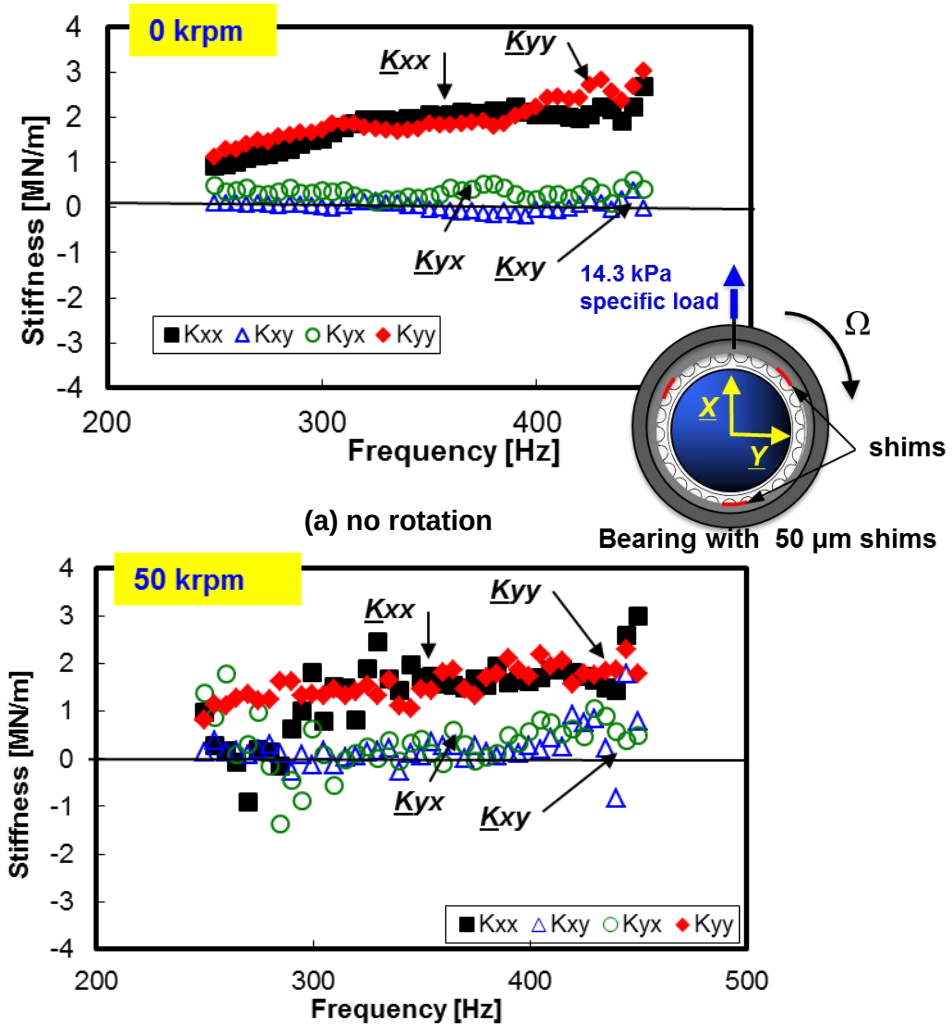

Figure 30. BFB stiffnesses ($(\underline{K}_{\alpha\beta})_{\alpha\beta=\underline{X},\underline{Y}}$) versus excitation frequency for a bearing with 50 μm shims. (a) no journal rotation and (b) with journal rotation (50 krpm). Results for sine sweep loads from 200-450Hz, displacement amplitude~ 20 μm, and a specific load *W/(LD)*~14.3kPa.

Also note that the dynamic load tests are conducted at a static vertical load of *W/(LD)*~14.3 kPa i.e., static and dynamic loads are applied to the test bearing. Thus the bump foil strip is compressed prior to the application of the dynamic loads. This is not the case for the static load tests as only static loads are applied to the test bearing.

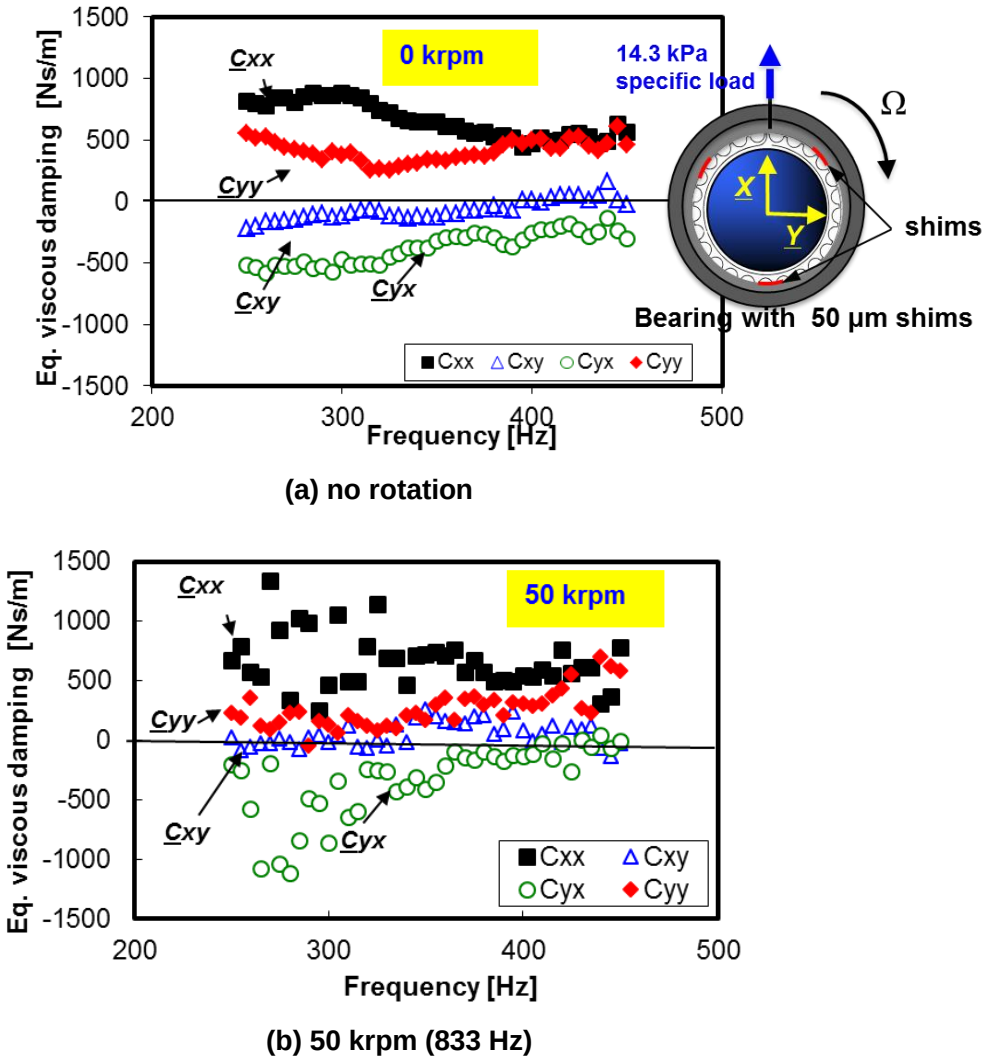

Figure 31. BFB viscous damping coefficients ($(\underline{C}_{\alpha\beta})_{\alpha\beta=\underline{X},\underline{Y}}$) versus excitation frequency for a bearing with 50 μm shims. (a) no journal rotation and (b) with journal rotation (50 krpm). Results for sine sweep loads from 200-450Hz, displacement amplitude~ 20 μm, and a specific load *W/(LD)*~14.3kPa.

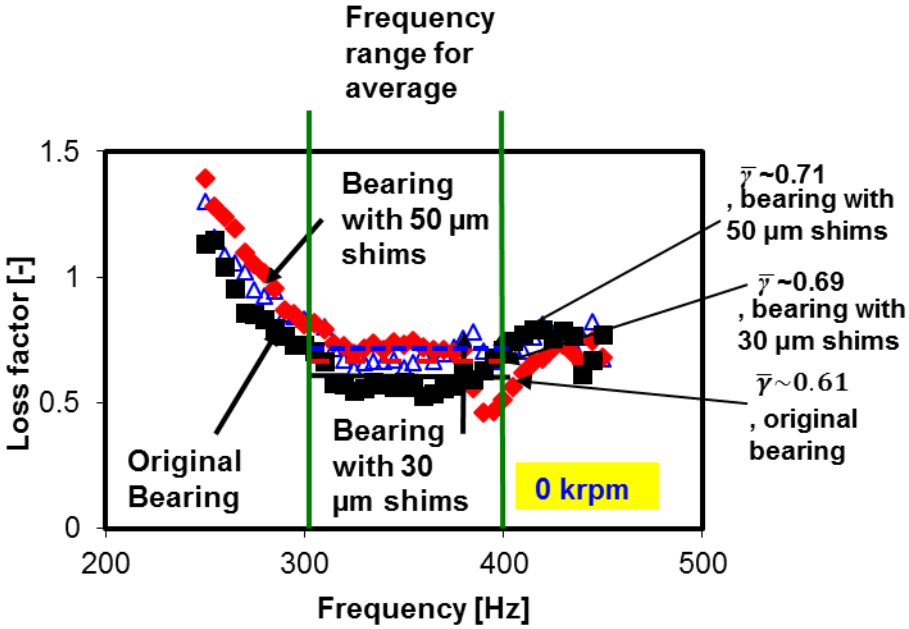

Figure 32. BFB material loss factor (γ) versus excitation frequency for the original bearing (without shims) and a bearing with shims of thickness 30 µm and 50 µm. Results without journal rotation, sine sweep loads from 200-450 Hz, displacement amplitude~ 20 µm, and a specific load *W/(LD)*~14.3kPa. Average loss factor shown for an arbitrary frequency range 300-400 Hz

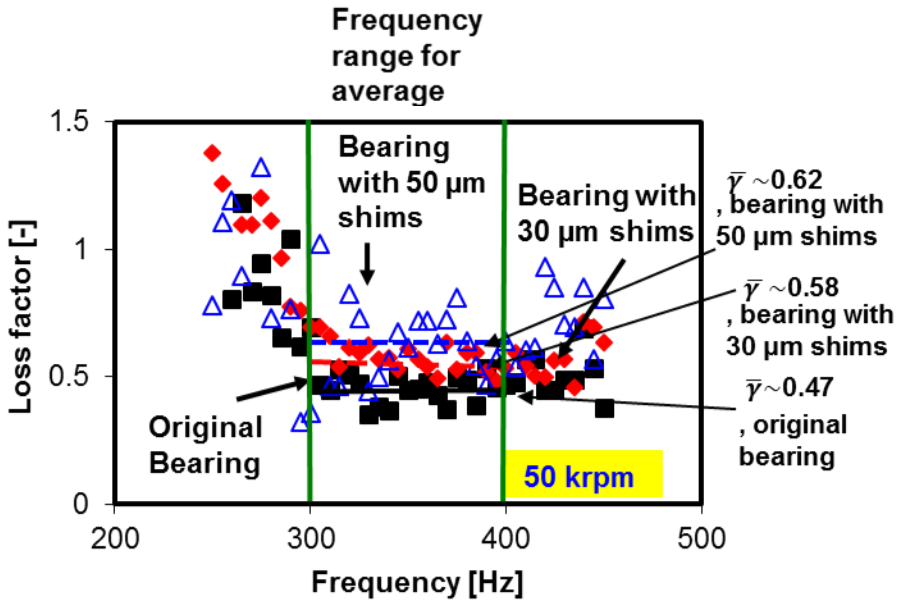

Figure 33. BFB material loss factor (γ) versus excitation frequency for the original bearing (without shims) and a bearing with shims of thickness 30 µm and 50 µm. Results with journal rotation (50 krpm), sine sweep loads from 200-450 Hz, displacement amplitude~ 20 µm, and a specific load *W/(LD)*~14.3kPa. Average loss factor shown for an arbitrary frequency range 300-400 Hz.

Table 2. Frequency averaged loss factor ($\bar{\gamma}$) for the original bearing (without shims) and a bearing with shims of thickness 30 *µ*m and 50 *µ*m operating with a stationary journal and rotor speed (50 krpm). Averaged from 300-400 Hz.

Bearing Configuration		Loss Factor, $\bar{\gamma}$	Standard deviation, σ
0 krpm	Original	0.61	0.070
	30 µm shims	0.69	0.090
	50 µm shims	0.71	0.056
50 krpm	Original	0.47	0.070
	30 µm shims	0.58	0.056
	50 µm shims	0.62	0.150

Prior literature [3-5, 27] suggests that shimming increases the force coefficients (stiffness and damping) in both generation I and generation II BFBs. However, the

results presented above evidence that for a dynamic displacement amplitudes ~20 μm, shimming has only a minimal effect on the bearing stiffness coefficients, while increasing the bearing direct damping coefficients (at frequencies above 300 Hz, and operating at 50 krpm), thus increasing the bearing loss factor ($\bar{\gamma}$).

Comparison of experimentally identified force coefficients with predictions

This section compares the experimentally estimated force coefficients to force coefficients predicted from a computational tool described in Ref. [33]. The bearing force coefficients are predicted at a shaft speed of 50 krpm and over an excitation frequency range of 200 Hz - 500 Hz for the bearing dimensional parameters described in Table 2. A specific load (*W/(LD)*~14.3 kPa) is applied along the vertical axis ($\underline{X}$ axis). The bearing structural loss factor (γ) is 0.5 [13] for all predictions. The structural stiffness of the original bearing (without shims) as estimated from the computation tool (~2.01 MN/m) agrees well with the stiffness derived from experiment with no journal speed (~ 2 MN/m). The gas temperature is ~50°C as per the ~ 30 °C temperature rise (from ambient ~ 20 °C) observed in the bearing cartridge and shaft during the experiments. Air is naturally drawn into the bearing.

[13] The bearing structural loss factor for the force coefficient predictions (γ~0.5) is selected as per the loss factor estimated from experiment for the original bearing operating at 50 krpm (see Figure 31).

Table 3 Nominal dimensions and specifications for the test bearing.

Parameters	**Magnitude**
Shaft diameter, D_s	36.5 mm
Bearing axial length, L	38.10 mm
Top foil thickness (Inconel X750), t_T	0.1 mm
Foil length , $2\pi D_I$	110 mm
Elastic modulus, E	209 GPa
Poisson's ratio, v	0.29
Number of bumps, N_B	26
Bump foil (Inconel X750)	
Thickness, t_B	0.112 mm
Pitch, s_0	4.5 mm
Length, l_B	2.1 mm
Height, h	0.50 mm
Elastic modulus, E	209 GPa
Poisson's ratio, v	0.29
Shim (AISI 4140)	
Length	38.1 mm
Thickness, t_s	0.050, 0.030 mm
Width	7.87 mm
Angular extent	12°
Elastic modulus, E	209 GPa
Poisson's ratio, v	0.29
Nominal FB radial clearance, c_{nom}	0.060 mm
Free end bump foil stiffness, K_{ff}	14.8 GN/m^3
Fixed end bump foil stiffness, K_{fp}	28.4 GN/m^3
Applied specific load (*X axis*)	27 kPa
Lubricant supply temperature	50°C
Excitation frequency range	200-450 Hz

The bearing radial clearance used for the predictions is ~110 μm. Centrifugal and thermal expansion of the rotor result in a smaller bearing clearance which must be accounted for. The test shaft (made of AISI 4140) is hollow with inner radius R_i ~ 6 mm and outer radius $R_o=D_o/2$ ~ 18.3 mm. As previously, mentioned a 30°C temperature rise is observed during dynamic load experiments. Table 4 presents the dimensions and mechanical properties of the journal (rotor).

Table 4 Nominal dimensions of the test journal.

Parameters	Magnitude
Outer d iameter, D_O	36.5 mm
Inner diameter, D_I	12.0 mm
Elastic modulus, E_s	200 GPa
Poisson's ratio, v	0.29
Linear Thermal Expansion coefficient (α)	12.3 x 10^{-6} 1/°C
Density (AISI 4140) (ρ)	7800 kg/m^3

The material properties of the AISI 4140 are found at Ref. [34]

Appendix F presents the formulation for centrifugal expansion of the shaft (r_g) as developed in Ref [35] and utilized in Ref. [36]. The expansion of the shaft radius due to centrifugal forces (r_g) at ~ 50 krpm is small, ~ 2 μm.

The formulation for the thermal expansion of the rotor (~ 7 μm) is also presented in Appendix F. Evidently, as the rotor operates at 50 krpm and experiences a temperature rise ~ 30°C, thermal expansion of the shaft is more significant than centrifugal expansion. The total increase in the shaft diameter due to thermal and centrifugal expansion is ~ 9 μm. Thus the bearing clearance decreases by 4.5 μm (radially) due to the combination of thermal and centrifugal effects. The bearing radial clearance used for the predictions (~110 μm) is in accordance with the bearing geometry and reductions due to thermal and centrifugal expansion of the shaft.

Tables 5 and 6 presents the journal static eccentricities, minimum film thickness and drag torque of a bearing without shims and with shims of thickness 30 μm and 50 μm predicted by the tool in Ref. [33]. Note that the bearings with shims operate with an eccentricity smaller than that of the original bearing, indicating that increased hydrodynamic pressure shifts the rotor to a more centered position. The minimum film thickness decreases for a shimmed bearing as the clearance reduces and as a result the drag torque increases due to increases in viscous shearing.

Table 5 Predicted minimum film thickness, and drag torque for a bearing with and without shims.

	Eccentricity µm	Attitude angle deg	Minimum film [µm]	Torque N-mm
Original bearing	96.0	24.8	16.1	2.90
Bearing with 30 µm shims	89.9	37.9	14.6	3.57
Bearing with 50 µm shims	80.4	39.0	10.3	4.16

Table 6 Predicted journal eccentricity for a bearing with and without shims.

	e_structure µm	ex µm	ey µm
Original bearing	122.4	87.2	40.3
Bearing with 30 µm shims	94.7	70.9	55.3
Bearing with 50 µm shims	76.2	62.5	50.6

Figure 34 through 37 present the experimentally identified force coefficients and predicted force coefficients versus excitation frequency for a bearing without shims and with shims of thickness equal to 30 µm and 50 µm. At frequencies above 300 Hz, the predicted $\underline{K}_{XX}$ is roughly half that of the experimentally identified $\underline{K}_{XX}$, while the predicted $\underline{K}_{YY}$ is 65% lower than that experimentally identified (uncertainty in the measured stiffness coefficients is ±0.08 MN/m, ±10%). Predicted $\underline{K}_{YX}$, and $\underline{K}_{XY}$ agree with their experimentally derived values. Also note that the model predicts the stiffness with journal speed to be much lower than the structural stiffness indicating that the gas film must have a low stiffness (perhaps due to the large clearance). In any case, the experimental results show that the direct stiffness with and without journal speed is approximately equal, indicating that the gas film stiffness is very high.

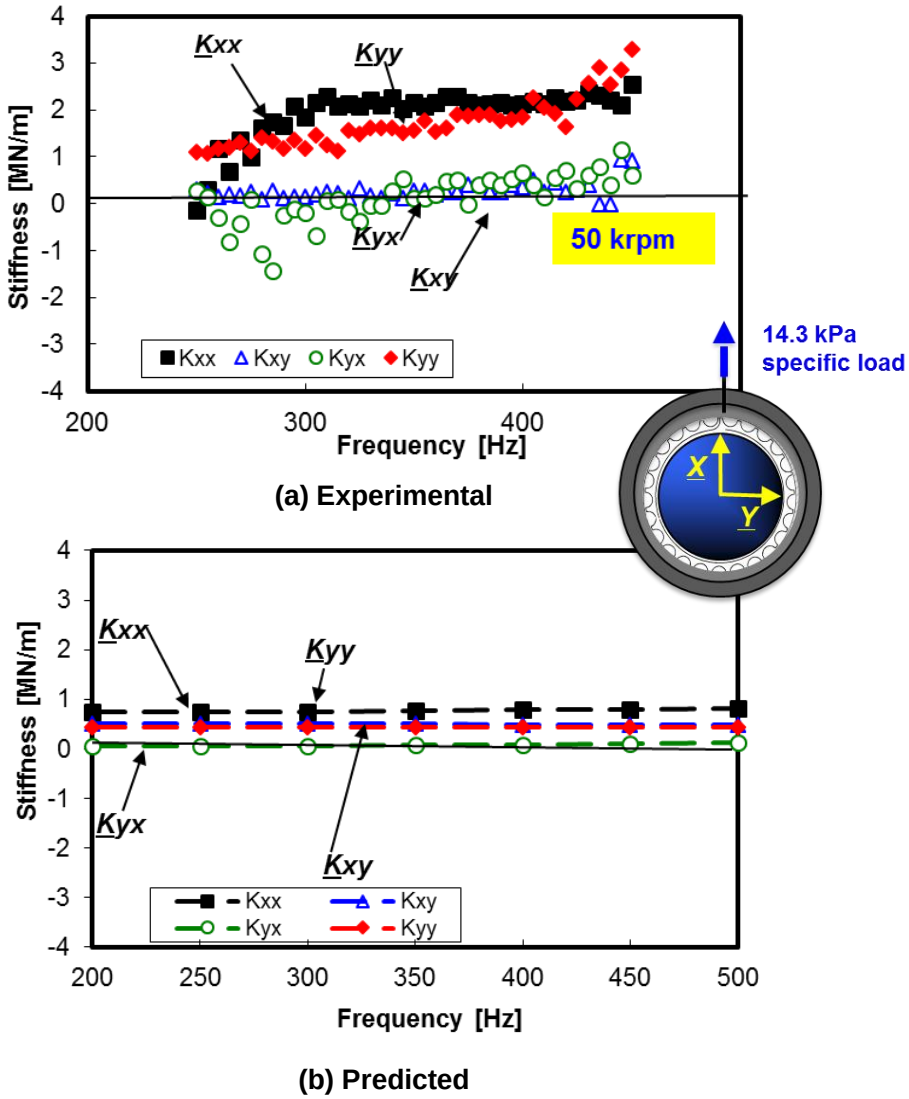

Figure 34. Stiffness coefficients versus frequency (a) measured and (b) predicted for the original bearing. Displacement amplitude~20 μm. Results for journal rotation (50 krpm) and sine sweep loads of 200-450Hz and a static load *W/(LD)* ~14.3 kPa. Predictions are carried out with a static load *W/(LD)* ~ 14.3 kPa.

The predicted direct damping coefficients ($\underline{C}_{XX}$, $\underline{C}_{YY}$) are but a small fraction of the experimentally estimated direct damping coefficients and change little with frequency. The predicted cross coupled damping coefficients agree with the measured cross coupled damping coefficients over the excitation frequency range.

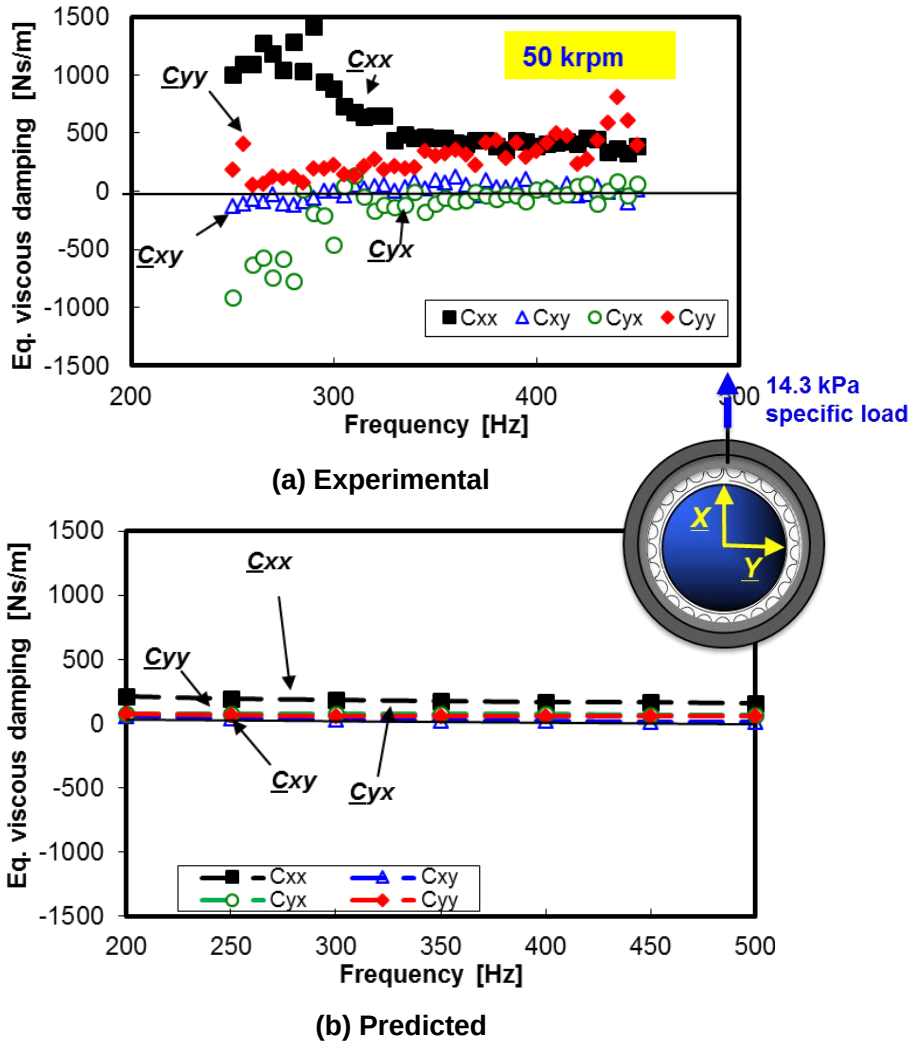

Figure 35. Damping coefficients versus frequency (a) measured and (b) predicted for the original bearing. Displacement amplitude~20 μm. Results for journal rotation (50 krpm) and sine sweep loads of 200-450Hz and a static load *W/(LD)* ~14.3 kPa. Predictions are carried out with a static load W/(LD) ~ 14.3 kPa.

The predicted $\underline{K}_{XX}$, and $\underline{K}_{YY}$ for the bearing with 30 μm shims are 11% larger the predicted $\underline{K}_{XX}$, and $\underline{K}_{YY}$ for the original bearing however still much lower than the experimentally identified $\underline{K}_{XX}$, and $\underline{K}_{YY}$ for the bearing with 30 μm shims. The predicted $K_{XY} > 0$ while $K_{YX} < 0$ (at low frequencies; 200-250 Hz).

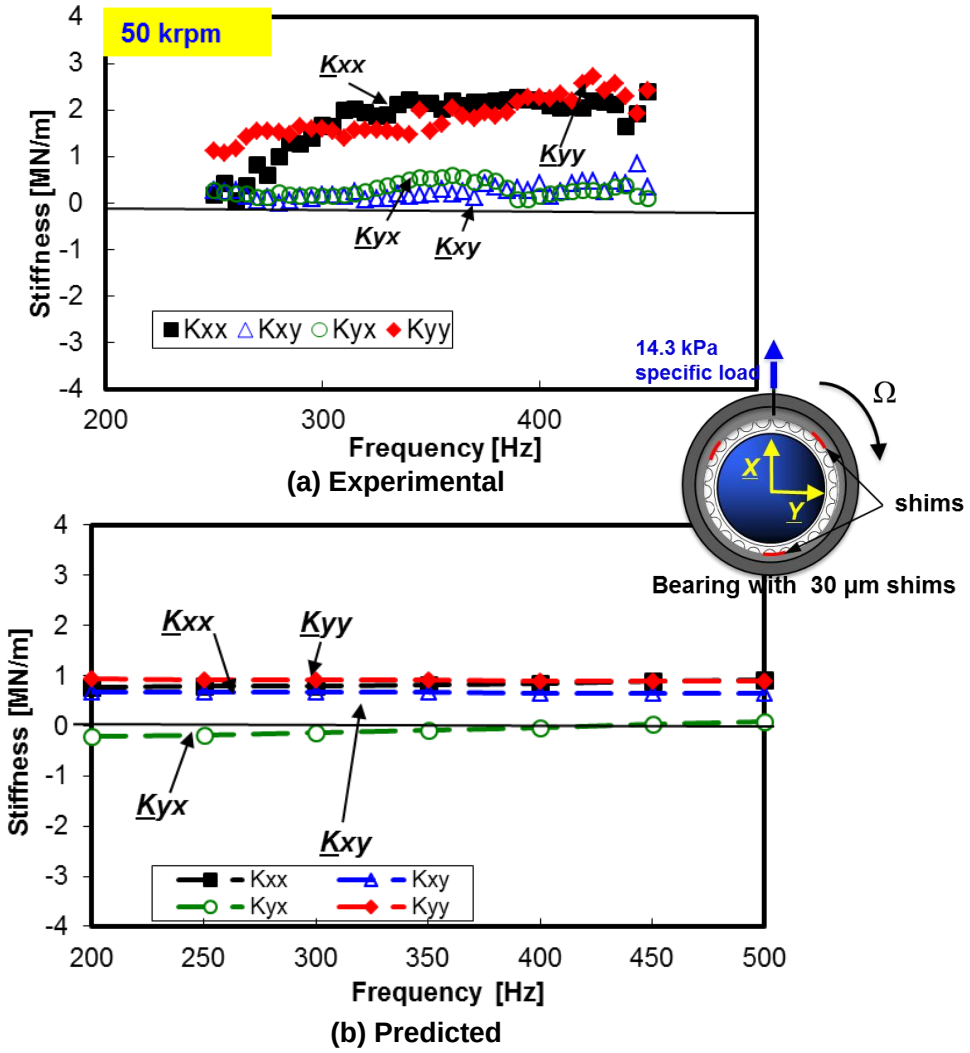

Figure 36. Stiffness coefficients versus frequency (a) measured and (b) predicted for a bearing with 30 μm shims. Experimental displacement amplitude~ 20 μm. Results with journal rotation (50 krpm) and a static load W/(LD) ~14.3 kPa. Predictions are carried out with a static load W/(LD) ~ 14.3 kPa.

In general the computational model under predicts the direct damping coefficients along the $\underline{X}$ axis of the bearing with 30 μm shims. Predicted direct damping along the $\underline{Y}$ axis is also undepredicted, however it agrees modestly with the estimated damping.

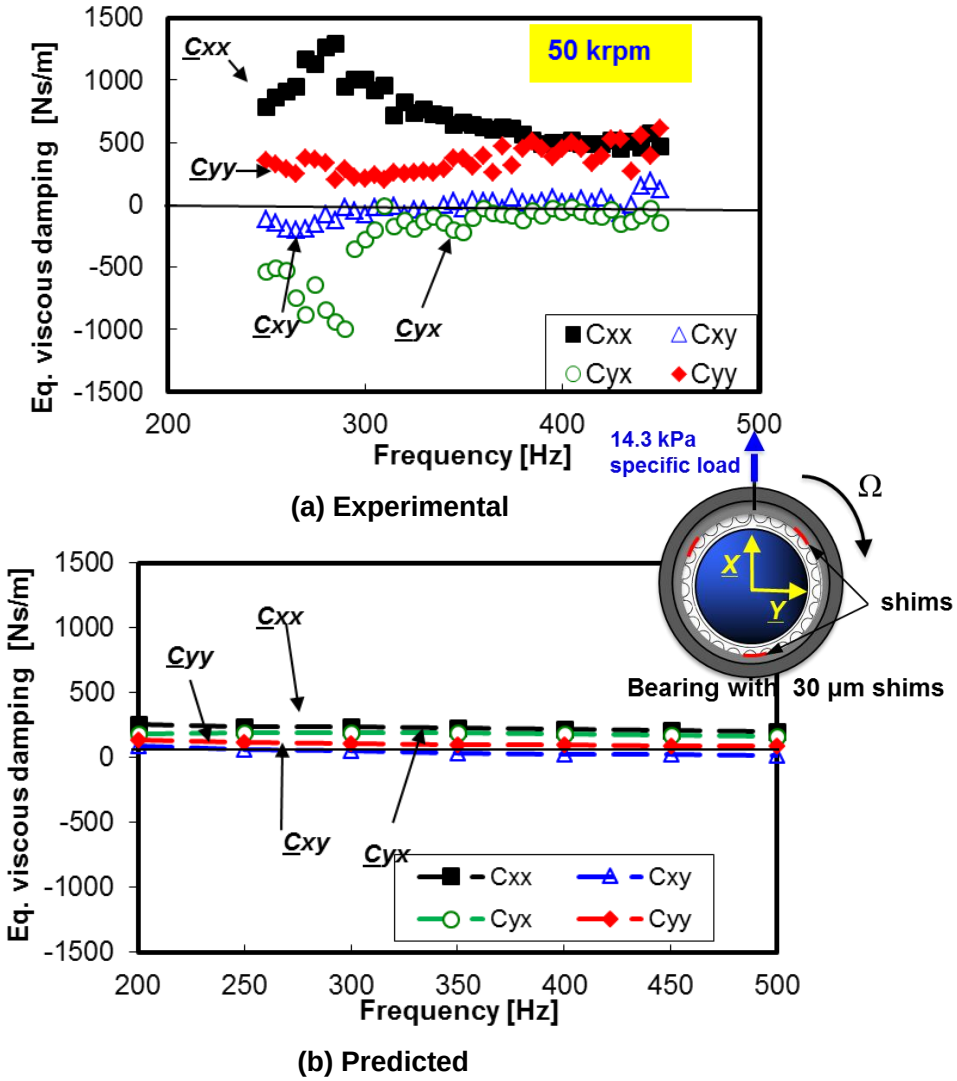

Figure 37. Damping coefficients versus frequency (a) measured and (b) predicted for bearing with 30 μm shims. Experimental displacement amplitude~ 20μm. Results for journal rotation (50 krpm) and a static load W/(LD) ~14.3 kPa. Predictions are carried out with a static load W/(LD) ~ 14.3 kPa.

Figures 36 and 37 present the predicted and measured stiffness and damping coefficients for a bearing with 50 μm shims. The predicted direct stiffness coefficients of the bearing with 50 μm shims are 42% lower than the experimentally identified force coefficients. While $\underline{K}_{XY}$ >0 and $\underline{K}_{YX}$ < 0 evidencing significant destabilizing hydrodynamic forces.

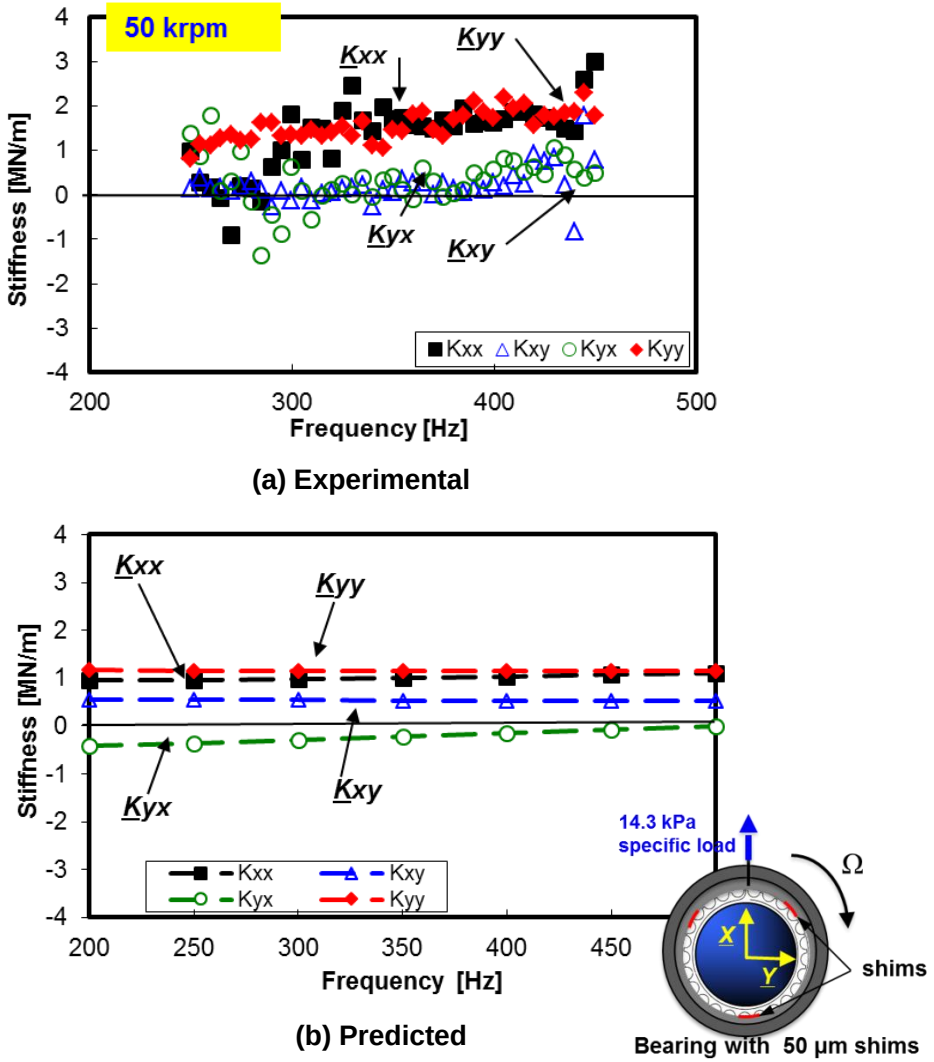

Figure 38. Stiffness coefficients versus frequency (a) measured and (b) predicted for a bearing with 50 μm shims. Experimental displacement amplitude~ 20μm. Results for journal rotation (50 krpm) and a static load W/(LD) ~14.3 kPa. Predictions are carried out for a static load *W/(LD)* ~ 14.3 kPa.

The predicted direct damping coefficients for the bearing with 50 μm shims remain (at most) half that of the measured direct damping values. Note, however that the model predicts that the shimmed bearings have larger (by 33%) direct damping coefficients than those of the original BFB.

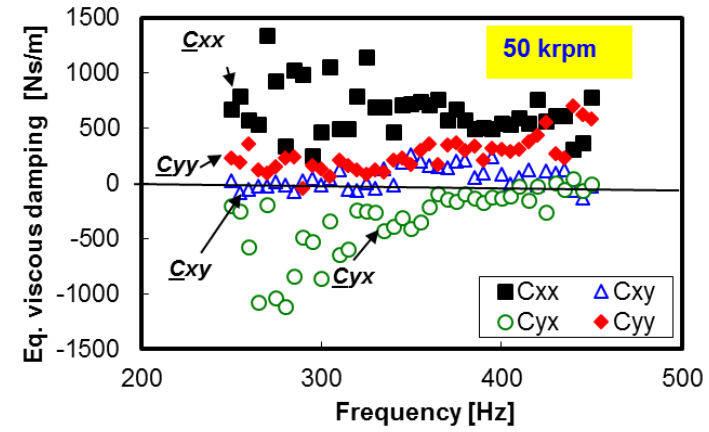

(a) Experimental

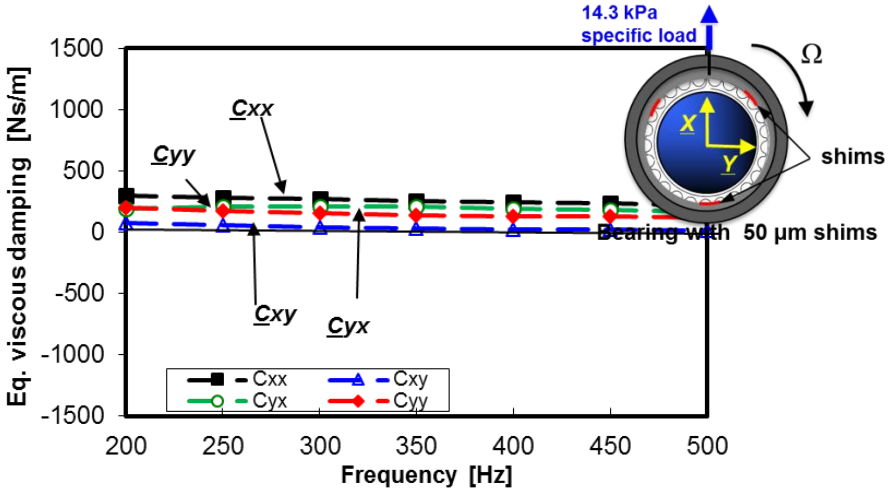

(b) Predicted

Figure 39. Damping coefficients versus frequency (a) measured and (b) predicted for bearing with 50 μm shims. Displacement amplitude~ 20 μm. Results with journal rotation (50 krpm). Results for sine sweep loads of 200-450Hz and a static load W/(LD) ~14.3 kPa. Predictions are carried out for a static load *W/(LD)* ~ 14.3 kPa.

The model predicts that the bearing with 50 μm shims will be 27% stiffer with 33% more damping as the original bearing. However the predictions for the direct stiffness and damping show only limited agreement with the corresponding experimental values. The model predicts destabilizing cross coupled stiffness and damping coefficients in the bearings with shims which is not reciprocated in the experimental results.

Figure 40 shows the gas film pressure (P/Pa) at the bearing centerline versus circumferential location. Note how the presence of the shims changes the pressure field in the BFB. The peak pressure (P/Pa) increases for a bearing with 50 μm shims (due to the decrease in the bearing clearance (c). The pressure in the original bearing drops to ambient at 250°. For the bearing with 50 μm shims, note the emergence of pressures (P/Pa>1.2) over a larger bearing surface area. The bearing with 30 μm shims shows only one region of hydrodynamic pressure generation while the bearing with 50 μm shims (and the smallest clearance) shows two regions of pressure generation. The minimum film thickness typically identifies the location of significant pressure generation in gas foil bearings [1]. Interestingly, the model predicts that the bearing with 30 μm shows no increased pressure generation due to the shims. The largest pressure is generated in the direction of the static load. Note that the bearing with 50 μm shims has a steeper, narrower (occurring over a shorter angular distance) pressure peaks at the bearing centerline than either the original bearing or the bearing with 30 μm shims.

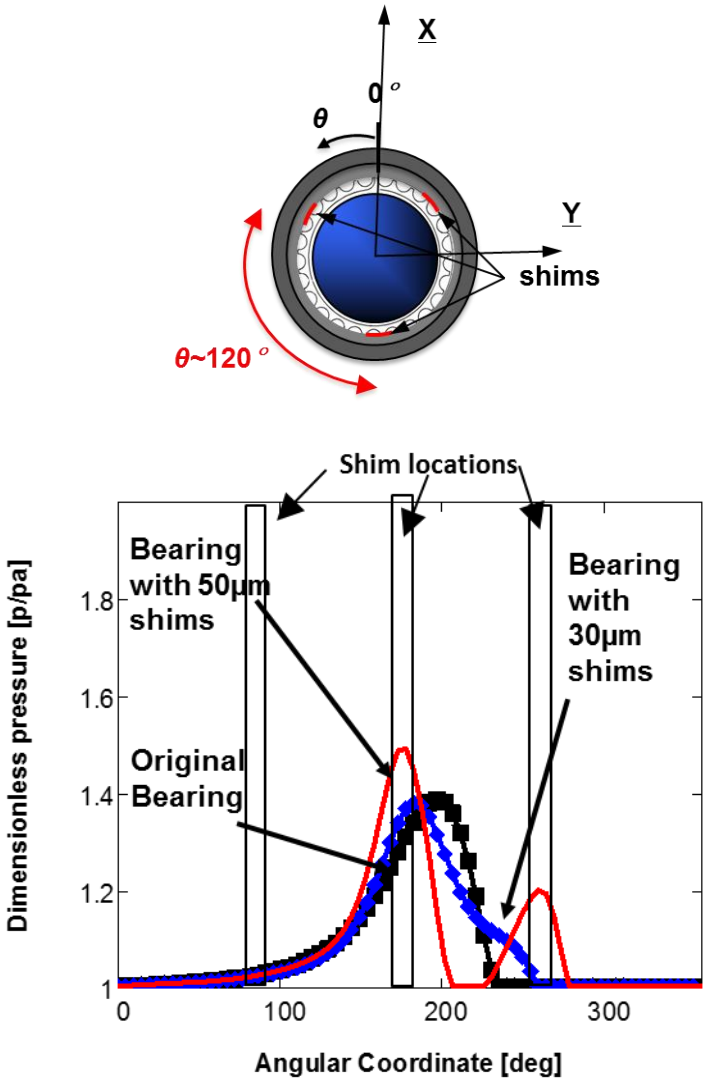

Figure 40. Predicted dimensionless pressure (P/Pa) at the bearing midplane along the circumferential coordinate. Results for a bearing without and with shims (30 µm and 50 µm). Specific load of 14 kPa in the *X* axis.

CHAPTER V

WATERFALL PLOTS OF TC JOURNAL VIBRATION

Two eddy current sensors placed as shown in Figure 41 enable the measurement of the BFB response relative to the rotating journal at a constant speed (Ω~50 krpm) for a bearing with and without shims via. The TC journal is manually accelerated to 50 krpm. Rotor vibration are recorded for all three regimes of rotor operation (startup, constant speed, and coast down) however only rotor vibration at a constant speed hold meaningful data.

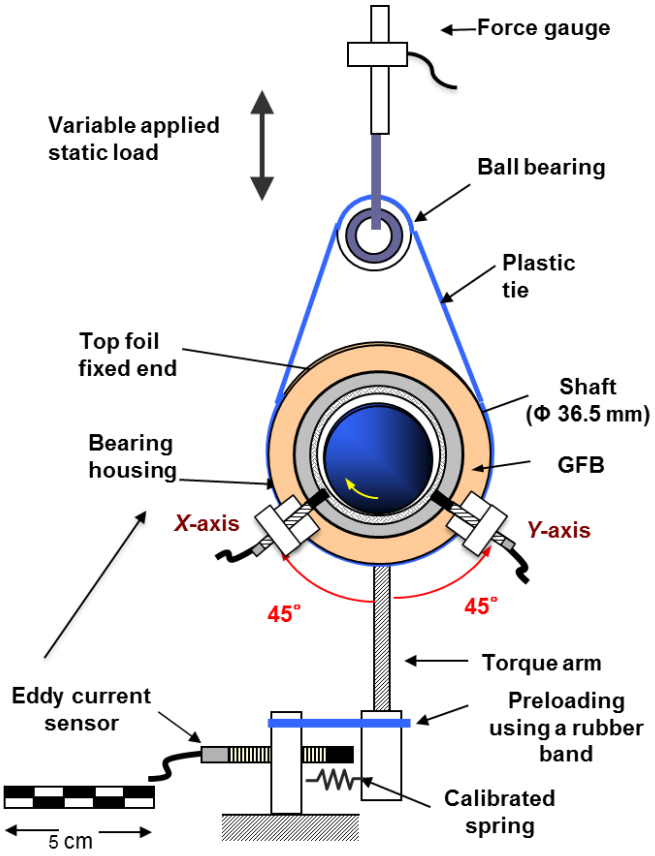

Figure 41. Schematic view of the test rig used to measure bearing drag torque and rotor vibration.

Figure 42 shows the waterfall plots of the rotor vibration for the original bearing and the same bearing with shims under a static vertical load, *W/(LD)*~0 kPa. The vibration amplitude upon rotor acceleration (run up and coast down) is small, however at a constant speed (~50 krpm) both synchronous and subsynchronous vibration amplitudes persist. Note also that the subsynchronous vibration amplitudes are much larger than the synchronous amplitudes and persist at ~200 Hz and are associated to rotor whirl. The whirl frequency ratio (WFR~ω_s/Ω_s) for the bearing without shims based on the waterfall plots of the rotor response is ~ 0.25. Note that ω_s is the whirl excitation frequency and Ω_s is the journal rotation frequency.

The subsynchronous vibration amplitudes (at 200 Hz) of the TC shaft when supported on the bearing with 30 μm shims are halved, while the synchronous response doubles. This result is likely due to the short duration over which the shaft maintains a constant speed 50 krpm. As a result, no conclusions are drawn about the synchronous vibration amplitudes of the shaft when supported on the shimmed BFB. Indeed shaft acceleration may ameliorate the vibration amplitudes. The bearing with 50 μm shims shows no subsynchronous whirl motion, and indeed the synchronous response is less than when the shaft is supported on the bearing with 30 μm shims. Despite no significant change in the bearing stiffness, and the large nominal clearance (120 μm), the bearings with shims successfully reduce the subsychronous whirl motions exhibited by the TC shaft.

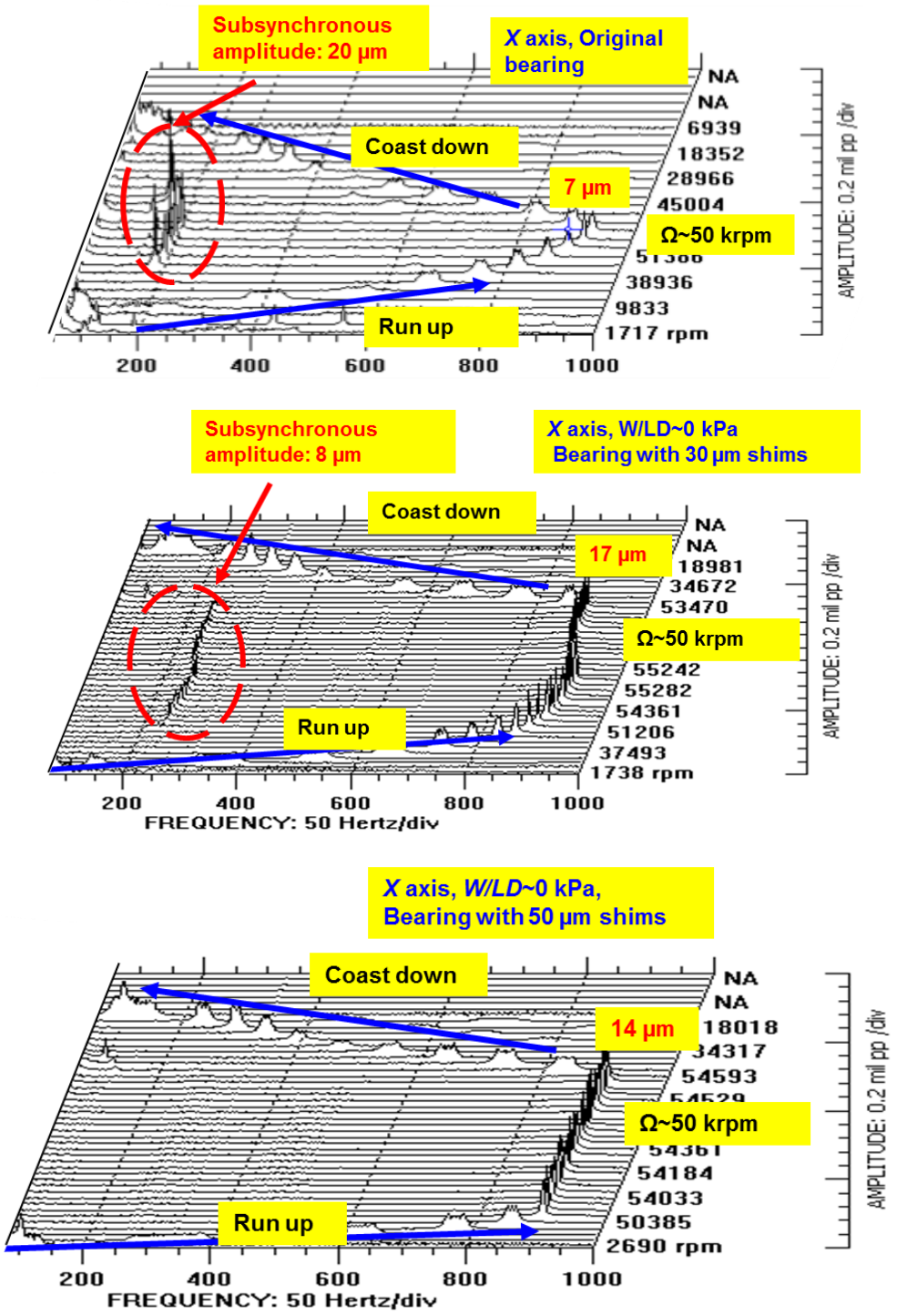

Figure 42. Waterfall plots of the rotor vibration for the (top) original bearing, (middle) a bearing with 30 µm and (bottom) 50 µm shims,(*W/(LD)* ~0 kPa).

CHAPTER VI

CONCLUSIONS

In conclusion, this report provides an experimental assessment of the performance of a shimmed BFB (L=38.1 mm, D= 36.5mm). The bearing is tested with two shim configurations featuring shims of thickness 30 μm and 50 μm. Two types of experiments are conducted on the test bearing; measurements of drag torque from rotor startup (where dry friction sliding is prevalent) to bearing lift off, to full gas film airborne operation, and estimation of frequency dependent force coefficients (with and without journal speed and with a static specific load of 14.3 kPa acting against gravity). The analysis brings to light design characteristics, such as the shim thickness to clearance ratio, which may affect the BFB force coefficients. The same experimental analysis should be conducted on other shimmed BFB with larger shim thicknesses, different patterns (4 and 5 shims), and with more strenuous loading condition (higher static specific loads, and larger displacement amplitudes) to provide a more comprehensive understanding of shimmed BFB performance. Also this thesis makes no analysis or assessment of the nonlinear nature of the bump foil structure and suggests this topic for future research. The major observations derived from the analysis of the results are:

From drag torque measurement of a bearing without shims,

(a) The breakaway friction factor ($f=T/(RW)$) decreases for $W/(LD)$ < 20 kPa and subsequently remains constant (~0.20) with respect to $W/(LD)$ (see Figure 9).

(b) The friction factor derived from the startup drag torque of the bearing without shims is ~0.30 and changes little with increasing load ($W/(LD)$) (see Figure 15).

(c) Measurements of the startup friction factor (with journal rotation), and derivation of the friction factor agree reasonably well with breakaway torque using a calibrated torque screwdriver for low loads. However at high loads ($W/(LD)$=20 kPa) the friction factor upon rotor startup is 30% higher than the breakaway friction factor. The discrepancy is likely related to top foil wear (see Figure 16).

(d) The rotor lift off speed increases linearly with specific load (see Figure 14).

From drag torque measurement of a shimmed bearing,

(e) The bearing friction factors derived from both the startup torque and the breakaway torque increase up to 40% for bearings with shims thickness (up to a 50 μm shim thickness (see Figure 14).

(f) The lift off speed for the bearing with 30 μm shims is approximately equal to that of the original bearing while the lift off speed for the bearing with 50 μm shims is higher than that of the original bearing for all loads (see Figure 15).

(g) The friction factor (while airborne) of the shimmed bearings is within 15% (at *W/(LD)*~20 kPa) of the friction factor for the original bearing. Interestingly, the difference between the friction factor of the shimmed bearings and the original bearing decreases as the load increases (*W/(LD)*) (see Figure 13).

(h) Ultimately, adding a mechanical preload through shimming increases the bearing friction factor upon a rotor speed startup procedure, hence leading to higher drive torque requirements and an increased power loss (see Figure 15).

From the force coefficients of a bearing with and without shims with a 14.3 kPa load (flexibly applied)

(i) The force coefficients (stiffness and damping) slightly decrease for operation with journal speed due to the two spring elements being in series (bump foil stiffness and gas film stiffness).

(j) The results show that the stiffness of a BFB without shims is approximately equal to a BFB with shims (for conditions with and without journal speed). However the direct damping (for operation at 50 krpm) increases by ~30% (over an arbitrary narrow frequency range, 300 Hz -400 Hz) for a bearing with shims.

(k) The ~ 30 °C temperature rise observed during the dynamic load tests has a minimal effect on the bearing force coefficients, as the stiffness coefficients with and without journal speed are largely the same.

(l) Below 300 Hz, the bearing loss factor (γ) is large (~1), dropping dramatically with frequency. Above 300 Hz, γ varies little with frequency.

(m) Over a narrow, arbitrarily selected frequency range from 300 Hz to 400 Hz, and for dynamic motions of 20 μm amplitude, the bearing with 50 μm shims offers a loss factor, $\bar{\gamma}$~0.62 , σ=0.15, up to 25% larger than that for the original bearing, with $\bar{\gamma}$~0.47, σ=0.07. The standard deviation (σ) of the $\bar{\gamma}$ for the bearing with 50 μm shims operating at 50 krpm is twice as large as the σ of the original bearing. Despite the large σ, the bearing with 50 μm shims has a $\bar{\gamma}$ equal to or larger than that of the original bearing (while operating with and without journal speed).

Comparison of experimentally identified force coefficient with predictions

(n) The computational tool predicts the bearing direct stiffness with journal speed to be significantly lower (60%) than when the journal is stationary (structural), evidencing that the gas film significantly affects the bearing stiffness. The experimental results suggest the opposite; suggesting that the presence of the gas film has a minimal effect on the bearing force coefficients (stiffness and damping).

(o) The model dramatically under predicts both the direct stiffness and damping at all frequencies (by ~50-60%) for all bearing configurations when compared to experimental results.

(p) Interestingly enough, the computational tool predicts the bearing with 50 μm to have 27% higher stiffness with 33% more damping than the predictions for the same bearing without shims. However the results of the predictions do not agree with experimental results, which shows no increase in stiffness but a 30% increase in damping (at >300Hz) for a bearing with 50 μm shims over that of the original bearing.

From the waterfall plots of the TC journal vibration

(q) The TC journal shows subsychronous whirl motions when supported on a BFB without shims.

(r) The TC journal shows lower subsynchronous motion amplitudes when supported on a BFB with shims than when supported on a BFB without shims. Indeed the shaft supported on a BFB with 50 μm shims shows no subsychronous whirl motion.

(s) No conclusions are advanced on the synchronous vibration amplitudes of the TC shaft.

REFERENCES

[1] DellaCorte, C., 2011, "Stiffness and Damping Coefficient Estimation of Compliant Surface Gas Bearings for Oil-Free Turbomachinery," STLE Tribol. Trans., **54** (4), pp.674-684.

[2] Chen, H.M., Howarth, R., Geren, B., Theilacker, J.C., and Soyars, W.M., 2001, "Application of Foil Bearings to Helium Turbocompressors," Proceedings Of 30th Turbomachinery Symposium, Houston, TX., September 22-25, 2001.

[3] DellaCorte. C., Radil, K.C., Bruckner, R.J., and Howard, S.A., 2008, "Design, Fabrication, and Performance of Open Source Generation I and II Compliant Hydrodynamic Gas Foil Bearings," STLE Tribol. Trans., **51**, pp. 254-264.

[4] Kim, T. H., and San Andrés, L., 2009, "Effects of a Mechanical Preload on the Dynamic Force Response of Gas Foil Bearings - Measurements and Model Predictions," STLE Tribol. Trans., **52**, pp. 569-580.

[5] Lee, Y-B., Suk, B.K., Kim, T.H., and Sim, K., 2013, "Feasibility of an Oil-Free Turbocharger Supported on Gas Foil Bearings via On-Road Tests of a Two-Liter Class Diesel Vehicle," ASME J. Eng. Gas Turbines Power, **135**, p. 052701-1.

[6] Sim, K., Lee, Y-B., Kim, T.H., and Jangwon L., 2012,"Rotordynamic Performance of Shimmed Gas Foil Bearings for Oil-Free Turbochargers", ASME J. Tribol.,**134**, p. 031102.

[7] Blok, H., and van Rossum, J. J., 1953, "The Foil Bearing – A New Departure In Hydrodynamic Lubrication," Lubr. Eng., December, pp. 316-320.

[8] Heshmat, H., Shapiro, W., and Gray., S, 1982, "Development of Foil Journal Bearings for High Load Capacity and High Speed Whirl Stability," ASME J. Tribol., 104, pp. 149-156.

[9] Heshmat, H., 1994, "Advancements in the Performance of Aerodynamic Foil Journal Bearings: High Speed and Load Capacity," ASME J. Tribol., **116**, pp. 287 - 295.

[10] Bruckner, R.J., and Puleo, B.J., 2008, "Compliant Foil Journal Bearing Performance at Alternate Pressures and Temperatures," ASME Paper No. GT2008-50174. pp.587-594

[11] DellaCorte, C, and Valco, M., 2000, "Load Capacity Estimation of Foil Air Journal Bearing for Oil-Free Turbomachinery Applications," STLE Tribol. Trans., **43**(4). pp. 795-801.

[12] DellaCorte, C., and Bruckner, R., 2011, "Remaining Technical Challenges and Future Plans for Oil-Free Turbomachinery," ASME J. Eng. Gas Turbines Power, **133**, p. 042502-1.

[13] Kim, T.H., Breedlove, A.W., and San Andrés, L., 2009, "Characterization of a Foil Bearing Structure at Increasing Temperatures: Static Load and Dynamic Force Performance," ASME J.Tribol., **131**, p. 041703-1.

[14] Rubio, D., and San Andrés, L., 2006, "Bump-Type Foil Bearing Structural Stiffness: Experiments and Predictions," ASME J. Eng. Gas Turbines Power, **128**, pp. 653-660.

[15] Rubio, D., and San Andrés, L., 2007, "Structural Stiffness, Dry-Friction Coefficient and Equivalent Viscous Damping in a Bump-Type Foil Gas Bearing," ASME J. Eng. Gas Turbines Power, **129**, pp. 494-502.

[16] Iordanoff, I., 1999, "Analysis of an Aerodynamic Compliant Foil Thrust Bearing: Method for a Rapid Design," ASME J. Tribol., **121**, pp. 816–822.

[17] San Andrés, L., and Norsworthy, J., 2013,"Identification of Structural Stiffness and Material Loss Factor in a Shimmed (Generation One) Bump-Type Foil Bearing," TRC-B&C-04-13, Annual Progress Report to the Turbomachinery Research Consortium, May. Mechanical Engineering, Texas A&M University, College Station, TX.

[18] Ginsberg, J., 2001, *Mechanical and Structural Vibrations-Theory and Applications*, Wiley, New York, Ch. 3. pp. 137-138.

[19] Matta, P., Arghir, M., and Bonneau, O., 2009, "Experimental Analyses of a Cylindrical Air-Bearing Dynamic Coefficients," STLE Tribol. Trans., **53**,pp. 329- 339.

[20] Rudloff, L., Arghir, M., Bonneau, O., and Matta, P., 2011, "Experimental Analyses of a First Generation Foil Bearing: Startup Torque and Dynamic Coefficients," ASME J. Eng. Gas Turbines Power, **133**, p. 092501.

[21] Chirathadam, T. A., and San Andrés, L., 2012, "A Metal Mesh Foil Bearing and a Bump- Type Foil Bearing: Comparison of Performance for Two Similar Size Gas Bearings," ASME J. Eng. Gas Turbines Power, **134**, p. 102501.

[22] Conlon, M.J., Dadouche, A., Dmochowski, W.D., and Bédar, J.-P., 2010, "A Comparison of the Steady-State and Dynamic Performance of First- and Second Generation Foil Bearings," ASME Paper No. GT2010-23683. pp. 453-462

[23] Radil, K.C., and DellaCorte, C., 2009, "A Three-Dimensional Foil Bearing Performance Map Applied to Oil-Free Turbomachinery," STLE Tribol. Trans., **53**, pp. 771- 778.

[24] Kim, T.H., and San Andrés, L. 2008, "Forced Nonlinear Response of Gas Foil Bearing Supported Rotors," Tribol. Int., **41**,pp. 704-715.

[25] Kim, T.H., Rubio, D., and San Andrés, L., 2007, "Rotordynamic Performance of a Rotor Supported on Bump Type Foil Gas Bearings: Experiments and Predictions," ASME J. Eng. Gas Turbines Power, **129**, pp. 850-857.

[26] Sim, K., Koo, B., Lee, J.S., and Kim, T.H., 2014,"Effects of Mechanical Preload on the Rotordynamic Performance of a Rotor Supported on 3 Pad Gas Foil Bearings," ASME Paper No. GT2014-25849. pp. 224-235

[27] Schiffmann, F., and Spakovszky, Z.S., 2013, "Foil Bearing Design Guidelines for Improved Stability," ASME J.Tribol., **135**, p.011103.

[28] Chirathadam, T. A., Kim, T.H, Ryu, K., and San Andrés, L., 2010, "Measurements of Drag Torque, Lift-Off Journal Speed and Temperature in a Metal Mesh Foil Bearing," ASME J. Eng. Gas Turbines Power, **132**(11), p. 112503.

[29] Glienicke, J., 1966, "Paper 13: Experimental Investigation of the Stiffness and Damping Coefficients of Turbine Bearings and Their Application to Instability Predictions," Proceedings of the Institution of Mechanical Engineers Symposium, Nottingham, United Kingdom., September 1966., **181** pp 122-135.

[30] Chirathadam, T.A., 2012, "Metal Mesh Foil Bearings: Prediction and Measurement of Static and Dynamic Performance Characteristics," Ph.D Dissertation, Texas A&M University, College Station, TX.

[31] James, J. F., 2002, *A Student's Guide to Fourier Transforms; With Applications in Physics and Engineering*, Cambridge, New York, **1** pp. 2-8.

[32] San Andrés, L., 2010, *Modern Lubrication Theory,* "Gas Film Lubrication," Notes 15, Texas A &M University Digital Libraries, http://repository.tamu.edu/handle/1969.1/93197 [3/7/2014].

[33] San Andrés, L., and Kim, T.H., 2006,"Computational Analysis of Gas Foil Bearings Integrating 1D and 2D Finite Element Models for Top Foil," TRC-B&C-01-06, Annual Progress Report to the Turbomachinery Research Consortium, May. Mechanical Engineering, Texas A&M University, College Station, TX.

[34] "Alloy Steel AISI 4140," eFunda, 2014,(accessed 6 August 2014), available from World Wide Web;
< http://www.efunda.com/materials/alloys/alloy_steels/show_alloy>

[35] Timoshenko, S. P. and Goodier, J. N., 1970, Theory of Elasticity, 3rd edition, McGraw-Hill, Singapore, pp. 80-83.

[36] Sim, K. H., 2007, "Rotordynamic and Thermal Analyses of Compliant Flexure Pivot Tilting Pad Gas Bearings," Ph.D Dissertation, Texas A&M University, College Station, TX.

APPENDIX A

DRAG TORQUE OF THE BALL BEARINGS

The drag torque from the ball bearings is identified for increasing static vertical loads prior to measuring the breakaway torque of the BFB. Figure A.1 shows a schematic view of the test rig used to measure the drag torque of the TC ball bearing.

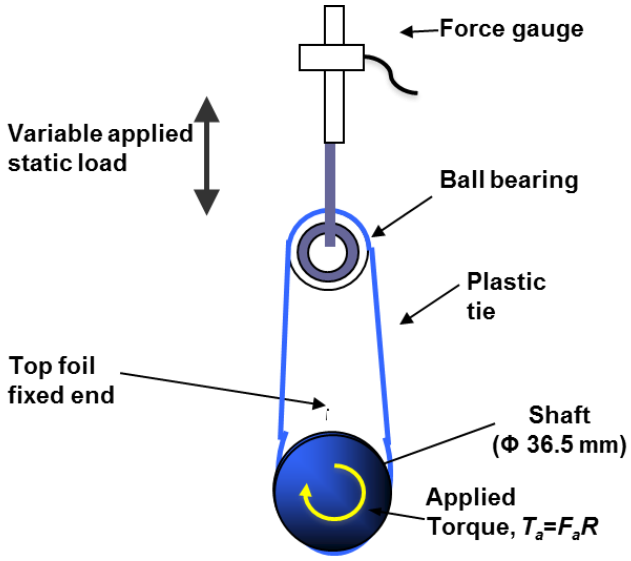

Figure A 1. Schematic view of the test rig to measure the TC ball bearing drag torque. Torque is applied to the TC shaft via a torque screwdriver

Figure A.2 presents the drag torque of the TC ball bearing versus static vertical load. The TC ball bearing drag torque increases linearly with static load. The presence of lubricant flow has a minimal effect on the drag torque of the TC ball bearing. During operation only a small amount of lubricant (at ambient temperature ~22°C) flows through the ball bearing, hence a small amount of lubricant does not affect the TC ball bearing drag torque. Also note that the highest load applied to the test bearing is 20 N thus the maximum ball bearing drag torque is <10 N-mm.

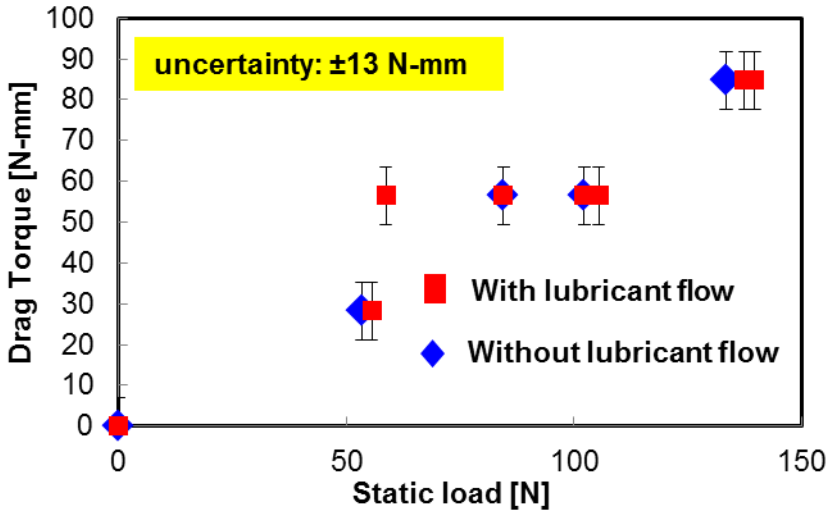

Figure A 2. TC ball bearing drag torque versus static vertical load with and without oil lubricant flow. Uncertainty ±28 N-mm.

APPENDIX B

POST TEST EQUIPMENT INSPECTION

100 start stop cycles are conducted on the rotor bearing system discussed in the main text. As previously discussed, wear on the rotor outer surface and bearing inner surface occurs due to rubbing between bearing and rotor surfaces upon start up and shut down. Figure B.1 shows pictures of the rotor and bearing surfaces before and after ~100 cycles of rotor start and stop. The rotor outer surface and bearing inner surface show wear from abrasion. The bearing suffers the most wear at the location where the static load forces the bearing and rotor to be in contact (largest contact pressure), which happens to be the location of the minimum film thickness, and the highest stiffness.

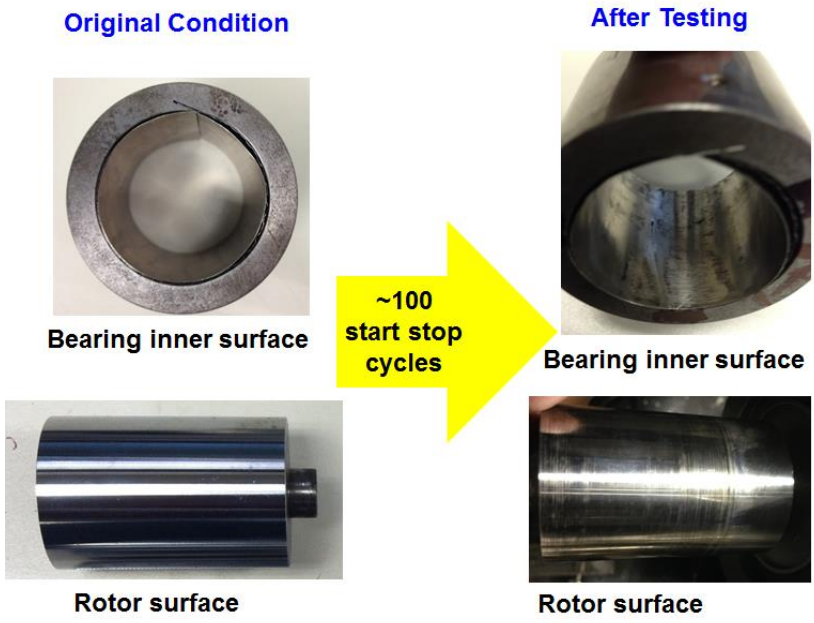

Figure B. 1. Photographs of the bearing and rotor inner surfaces before and after ~100 cycles of rotor start and stop.

APPENDIX C

UNCERTAINTY AND VARIABILITY

This section outlines the calculation of uncertainty and discussion of variability in the drag torque measurements and the experimentally identified BFB force coefficients. The instrument uncertainty of the accelerometers, load cells, and eddy current sensors is 1% linearity.

Uncertainty in the drag torque measurements

The uncertainty in drag torque ($T=\delta K_s L_T$) measurements is due to the uncertainty in the measurement of position (δ), the spring stiffness (K_s), and the measurement of the torque arm (L_T). The torque arm is measured with calipers, uncertainty~ ±.0001mm (U_L). The uncertainty in the position measurement is ±0.70 μm (U_x). The spring stiffness is estimated from load deflection tests. The spring stiffness is identified as the slope of the load deflection curve, which is linear. The uncertainty in the spring stiffness is (±0.33 N/mm). The Cline-McClintock method of evaluating measurement uncertainty delivers a general uncertainty formulation for a function of multiple variables ($r=f(x_1, x_2,\ldots\ldots,x_n)$). The general equation for the uncertainty of a function with multiple variables is

$$Ur = \sqrt{\left(\frac{\partial r}{\partial x_1}U_{x_1}\right)^2 + \left(\frac{\partial r}{\partial x_2}U_{x_2}\right)^2 + \ldots + \left(\frac{\partial r}{\partial x_n}U_{x_n}\right)^2} \qquad (1)$$

Using the above equation, the uncertainty of the drag torque (U_T) is identified from the following equation.

$$\left(\frac{U_T}{T}\right)^2 = \left(\frac{U_x}{x}\right)^2 + \left(\frac{U_K}{K}\right)^2 + \left(\frac{U_{L_T}}{L_T}\right)^2$$

From this equation the uncertainty in the measured drag torque is ±1 N-mm.

Variability in the drag torque measurements

Drag torque measurements are conducted for a bearing with i) no shims and ii) with shims (30 μm, and 50 μm). The bearing drag torque is recorded for rotor speeds up to 50 krpm. To determine the variability of the drag torque measurements, at least three tests are conducted for each test condition (static load, and shim thickness). Figure C.1 shows the drag torque results and their variability for three tests for a bearing with and without shims (*W/(LD)*~0 kPa). The maximum variability occurs for test conducted on the original bearing, ~ 60 N-mm. The drag torque results agree very well between individual tests and show very little variance, thereby demonstrating reliable repeatable results.

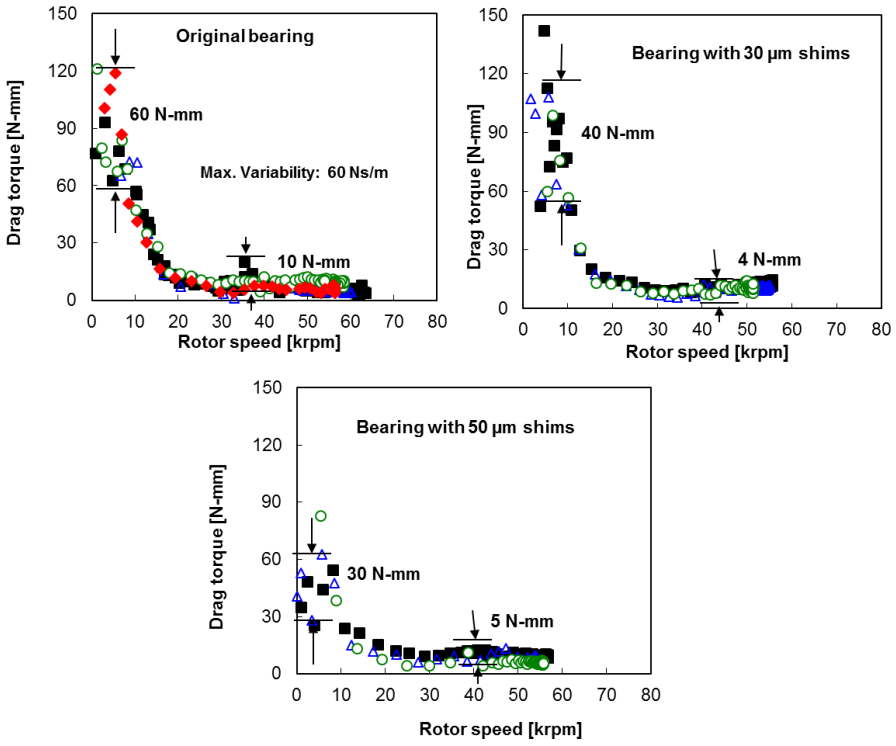

Figure C 1. Bearing drag torque (*T*) versus rotor speed (Ω) for a bearing with and without shims for a static load, *W/(LD)*~0 kPa. Results for at least three tests are shown

Uncertainty in the force coefficients

The uncertainty analysis of the bearing force coefficients follows a procedure used in Ref. [28]. Uncertainty in the bearing force coefficients arises from the instrumentation uncertainty in the measurements of bearing cartridge acceleration, bearing relative displacement and excitation force. The relationship between the measured signals and the bearing impedances ($H_{\alpha\beta} = K_{\alpha\beta} + j\omega C_{\alpha\beta}$; $\alpha, \beta = X, Y$) in the *X* direction is

$$H_{XX}\bar{x}'^{X} + H_{XY}\bar{y}'^{X} = \bar{G}_X{}^{X} = \bar{F}_X{}^{X} - \left(M_{S_X} + {C_{S_X}}/{j\omega} - {K_{S_X}}/{\omega^2} \right) \bar{A}_X{}^{X} \qquad (2)$$

Assuming the uncertainties of the two terms on the left hand side (LHS) of Eqn. are approximately equal, the uncertainty in H_{XX} is computed using Eqn. E.2

$$\left(\frac{U_{H_{XX}}}{H_{XX}} \right) = \frac{1}{\sqrt{2}} \sqrt{ \left(\frac{U_{G_X^X}}{G_X^X} \right)^2 + \left(\frac{U_{\bar{x}'^X}}{\bar{x}'^X} \right)^2 } \qquad (3)$$

The fractional uncertainties in the dynamic load ($\frac{U_F}{F}$), acceleration ($\frac{U_{A_X}}{A_X} = \frac{U_{A_Y}}{A_Y}$) and the excitation frequency ($\frac{U_\omega}{\omega}$) are less than 0.02, 0.01, and 0.05 respectively. The resulting maximum uncertainty in the stiffness and damping coefficients is ±0.08 MN/m and ± 80 Ns/m, respectively.

Variability in the force coefficients

A minimum of three tests are conducted for each test condition to asses and verify the repeatability of the identification process. Figures C.2 and C.3 show the bearing stiffness and damping coefficients for four repeated tests versus excitation frequency. The tests are conducted on a bearing without shims, with approximately 14.3 kPa load acting down (with gravity) on the bearing. Also note that these tests correspond to tests with no journal rotation.

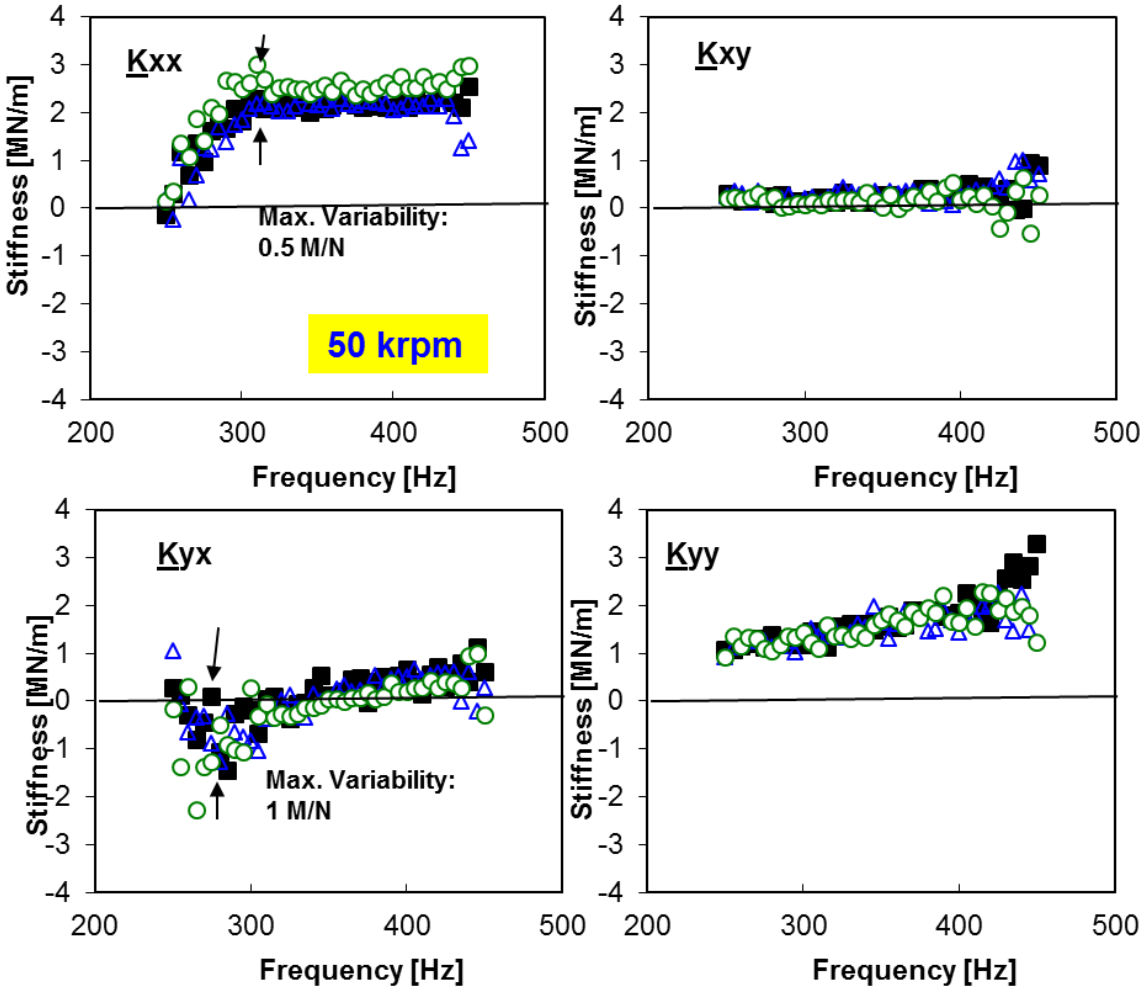

Figure C 2. Test sets 1 – 4: Identified BFB stiffness coefficients ($\underline{K}_{XX}$, $\underline{K}_{YY}$, $\underline{K}_{XY}$,$\underline{K}_{YX}$) versus frequency. Applied static load *W/(LD)* ~ 14.3 kPa. Journal spinning at 50 krpm.

The maximum variability in the K_{XX}, K_{XY}, K_{YX}, and K_{YY} are 0.4 MN/m, ~0.1 MN/m, 0.2 MN/m and ~ 0 MN/m respectively; while for C_{XX}, C_{XY}, C_{YX}, and C_{YY} are 200 Ns/m, 40 Ns/m, 200 Ns/m and 60 Ns/m, respectively. The test data indicates that there is considerable variability in the identified damping coefficients however the variability in the stiffness coefficients is quite low.

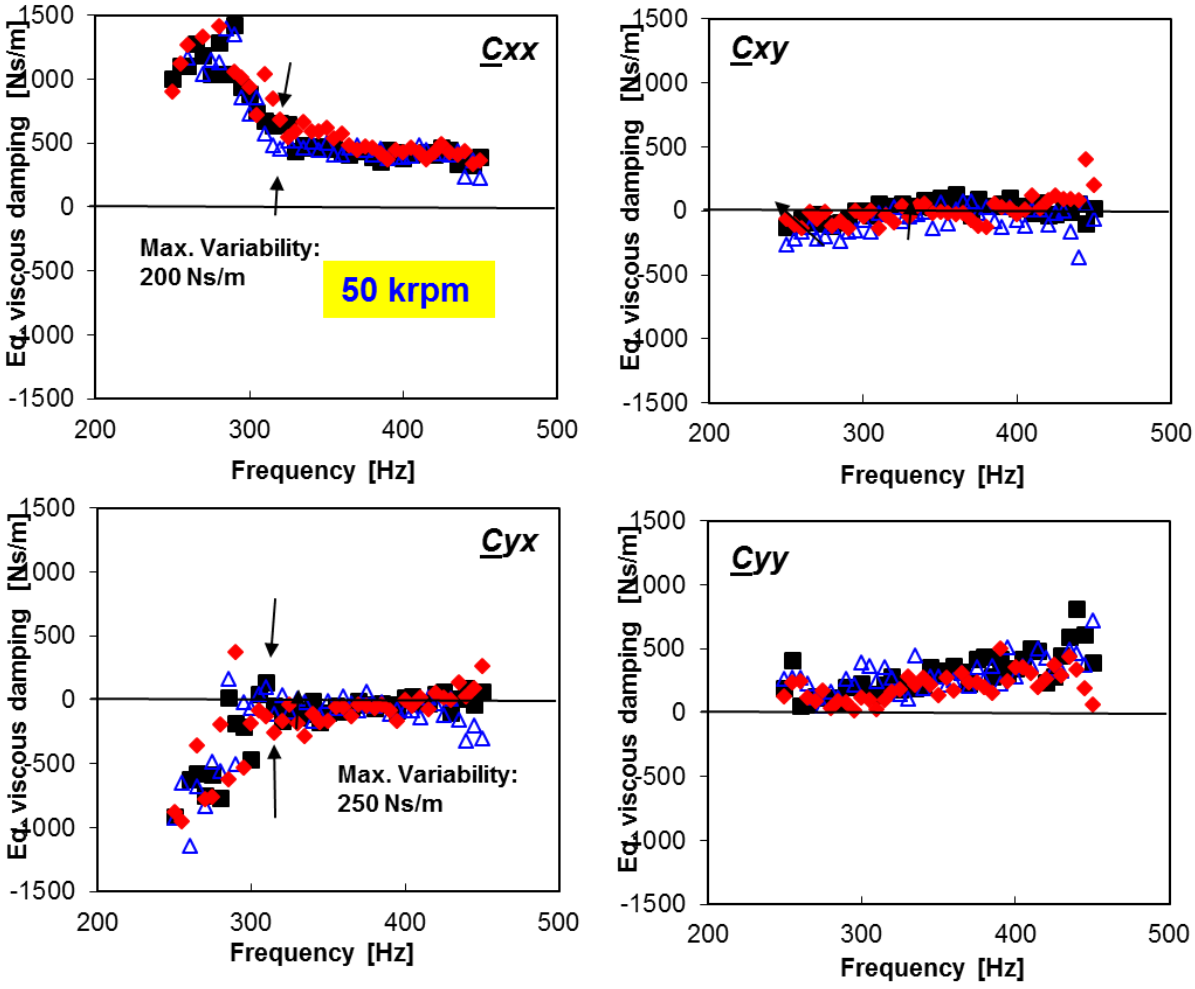

Figure C 3.Test sets 1-4: Identified BFB damping coefficients (CXX, CYY, CXY, CYX) versus frequency. Applied static load W/(LD) ~ 14.3 kPa. Journal spinning at 50krpm.

APPENDIX D

ESTIMATION OF THE SQUIRREL CAGE STRUCTURAL PARAMETERS

As note previously, the test BFB is held by a soft elastic structure (squirrel cage) comprised of 8 thin steel rods arranged in a circular pattern. The radial stiffness and damping coefficients of the elastic structure must be determined first. Figure D.1 shows a photograph of the squirrel cage and bearing to which impact loads are applied. Note that the bearing is not resting atop the rotor during impact tests.

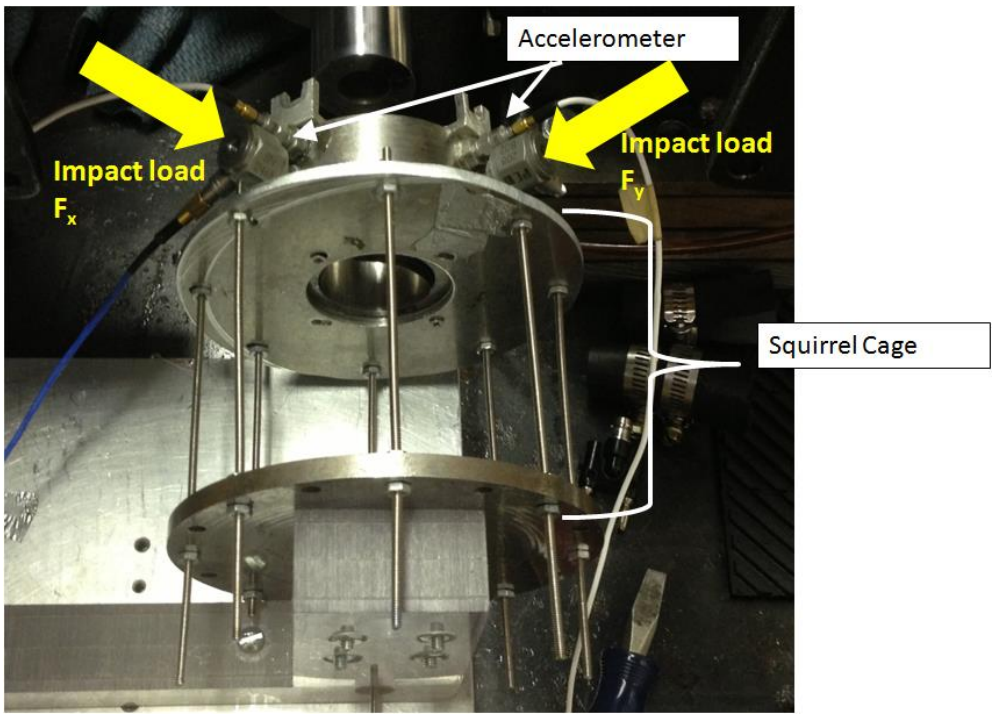

Figure D 1. Top view of the squirrel cage and bearing to be impact tested.

Figure D.2 shows the typical impact excitation loads (F_X, F_Y) exciting the FB and squirrel cage assembly and the resulting FB acceleration in the X and Y directions (a_X, a_Y). The excitations are applied orthogonal to each other. Figure D.3 shows the bearing

accelerations in the frequency domain. The results demonstrate a lightly damped system with a natural frequency at ~ 20 Hz. Results also evidence low structural cross coupling.

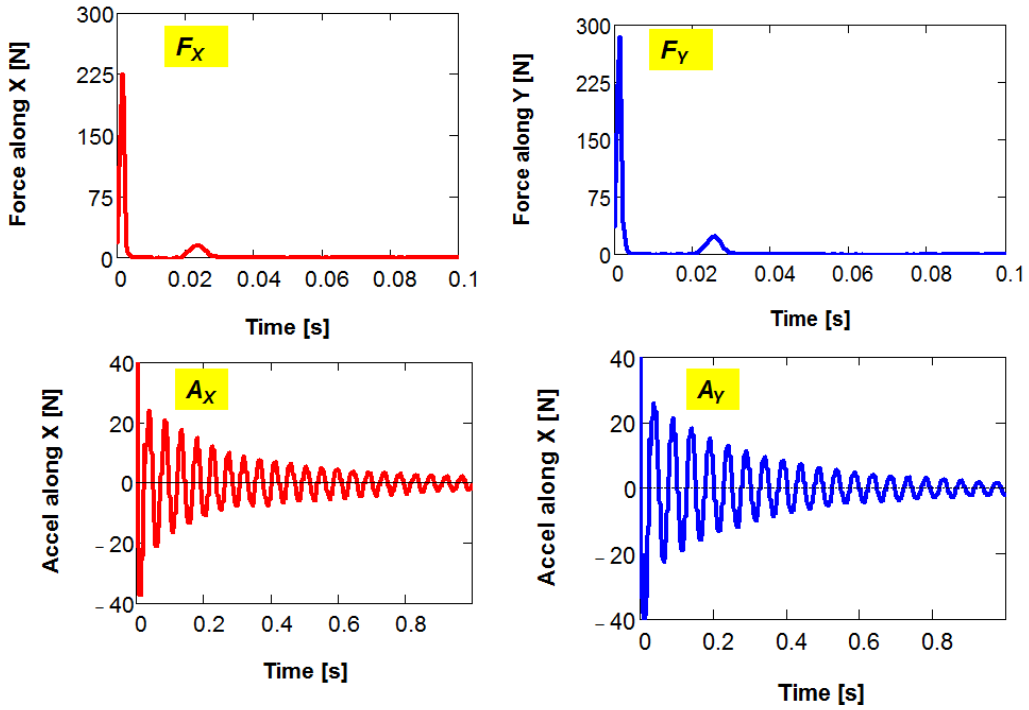

Figure D 2. (top) Impact loads and (bottom) recorded bearing accelerations, *X* and *Y* directions, versus time. No contact with journal.

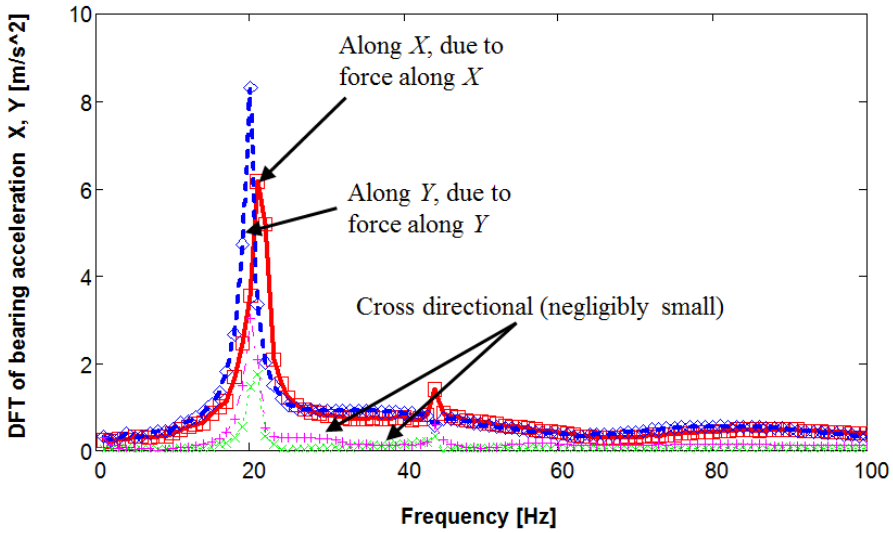

Figure D 3. Discrete Fourier Transform amplitudes of accelerations along *X* and *Y* directions due to impact loads on the bearing and elastic support structure assembly.

Since there is little structural cross coupling, the bearing and elastic structure behave as a single degree of freedom system along each direction. The system is characterized by a system mass (M_S), stiffness (K_S) and viscous damping (C_S) coefficients along each direction (X,Y). The measurements of acceleration and impact load are used to extract the structural parameters according to a nonlinear curve fit of the accelerance function. The accelerance function along the X direction is

$$\left\| \left[\frac{a_{X(\omega)}}{F_{X(\omega)}} \right] \right\| = \frac{\omega^2}{\left\{ \left(K_{S_X} - \omega^2 M_{S_X} \right)^2 + \left(\omega C_{S_X} \right)^2 \right\}^{1/2}} \qquad (1)$$

where ω denotes frequency. Figure D.4 shows the recorded accelerance function $\left| a_{X(\omega)} / F_{X(\omega)} \right|$ and its curve fit equation. The identified mass is M_{S_X} = 1.5 kg and includes the mass of the bearing, and the squirrel cage structure moved during excitation.

The identified structural stiffness K_{S_X} = 26 kN/m, and the damping coefficient C_{S_X} = 8.2 Ns/m. The goodness to fit is R^2 = 0.92 for the frequency range (0-300Hz).

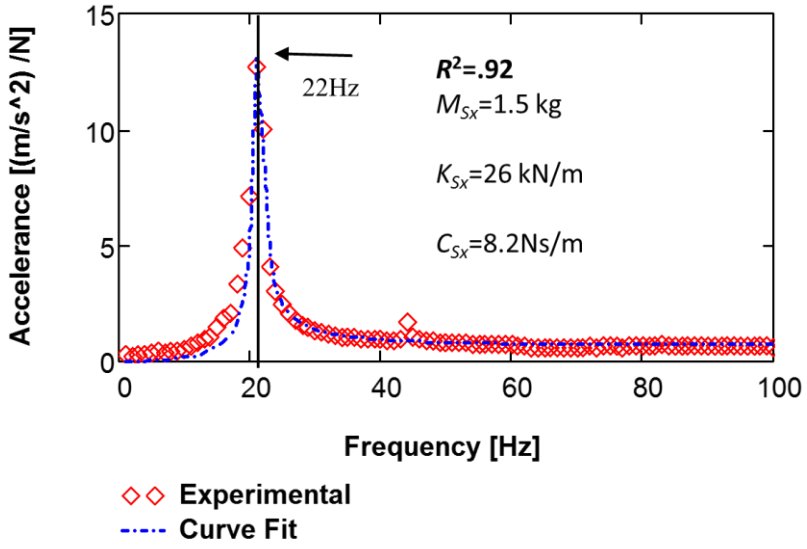

Figure D 4. Accelerance $|a_X/F_X|$ and curve fit to identify parameters of bearing elastic support structure.

Likewise Figure D.5 shows the recorded accelerance function $\left|a_{Y(\omega)}/F_{Y(\omega)}\right|$ and its curve fit equation. The identified parameters include the identified mass is M_{S_Y} = 1.7 kg .The identified structural stiffness K_{S_Y} = 26 kN/m, and damping coefficient C_{S_Y} = 3.2 Ns/m, and the goodness to fit is R^2 = 0.95 for the frequency range (0-300Hz).

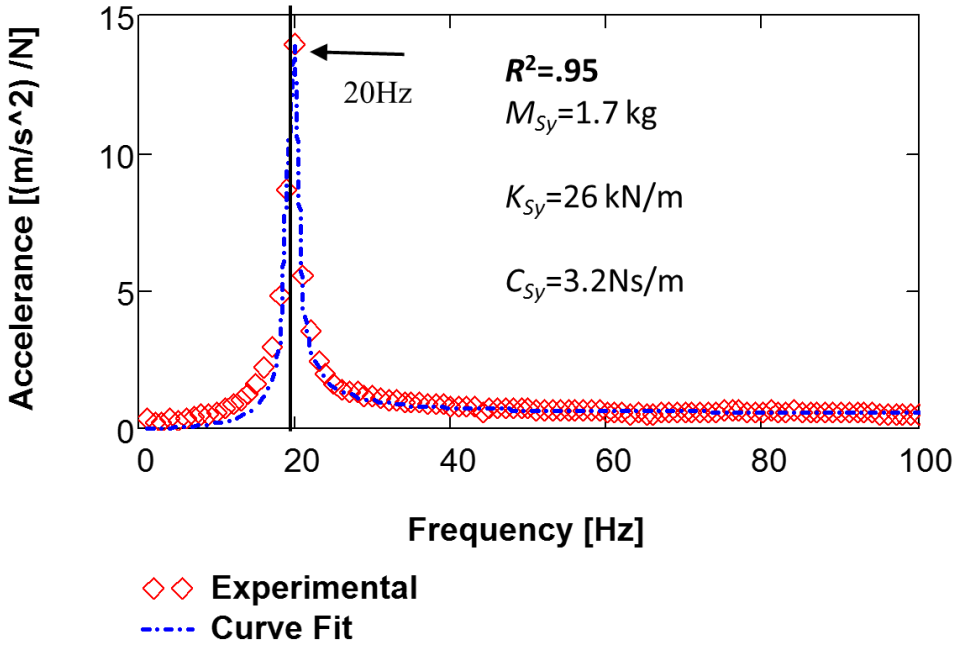

Figure D 5. Accelerance $|a_Y/F_Y|$ and curve fit to identify parameters of bearing elastic support structure.

The identified bearing structural coefficients along *X* and *Y* directions, listed in Table F.1, are similar however the system is not isotropic. The uncertainty in the identified parameters is due to the uncertainties in the load cell (1% linearity), and accelerometer (1% linearity). The variability (among three independent tests) in K_{S_Y}, C_{S_Y}, M_{S_Y} is 3.9 kN/m, 2 Ns/m, and 0.1 kg respectively. The variability in K_{S_X}, C_{S_X}, M_{S_X} is 6 kN/m, 1.9 Ns/m, 0.2 kg respectively (also among three independent tests). The mass of the bearing as measured from a scale is 1.2 kg. Note that the damping ratios identified are quite small especially for along the *Y* direction.

Table D 1. Measured mechanical parameters for bearing and elastic support structure.

	Y direction	*X* direction	
Stiffness, K_S	26±2	24±3	kN/m
Mass, M_S	1.7±0.1	1.5±0.05	kg
Damping, C_S	3.2±1	8.2±1	N.s/m
Natural frequency	20±0.5	22±0.5	Hz
Damping ratio	0.01	0.021	-
R^2	0.92	0.95	-

APPENDIX E

MEASUREMENTS OF BFB ACCELERATION AND DISPLACEMENT WITH ROTOR SPEED (50 KRPM)

Figures E.1 through E.3 show the bearing motions (time and frequency domain bearing relative displacements and frequency domain bearing absolute accelerations) versus excitation frequency for tests conducted on a bearing without shims under a specific load *W/(LD)*~14.3 kPa and for journal operation at 50 krpm.

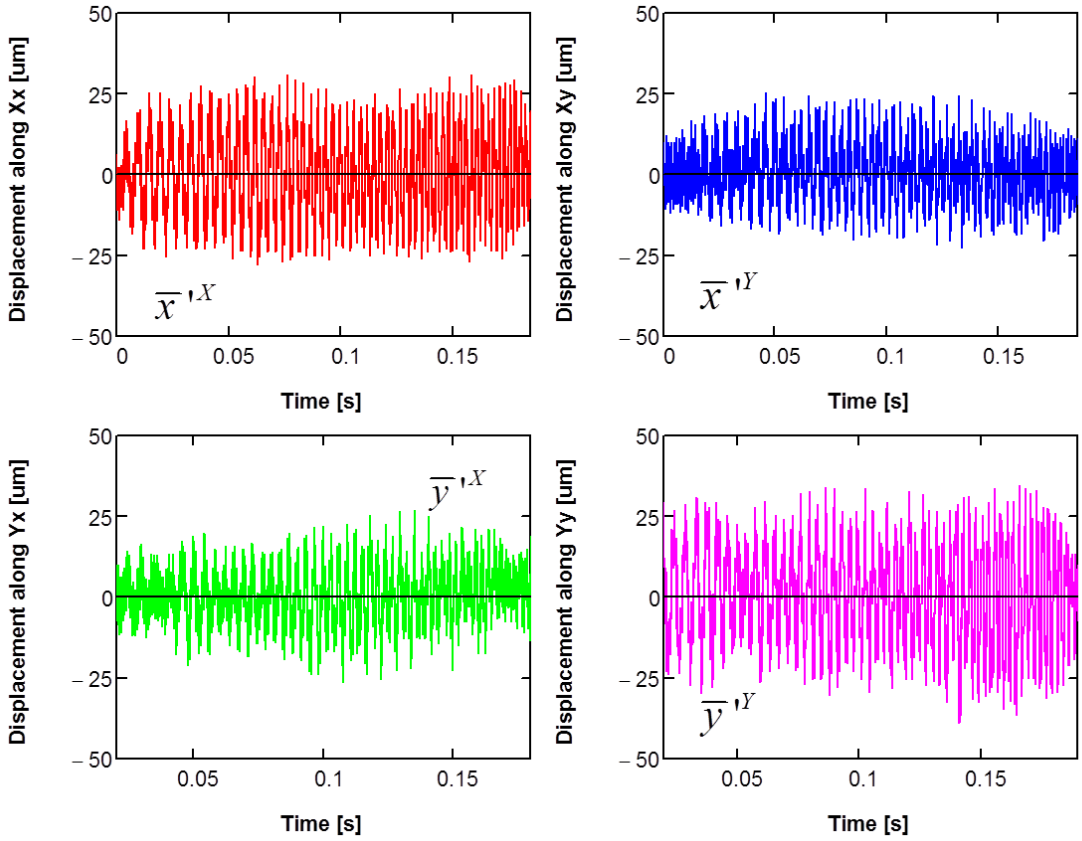

Figure E 1. Direct (top) and cross directional (bottom) bearing relative displacements along *X* and *Y* directions. Applied specific load W/(LD)~ 14.3 kPa. Journal spinning at 50 krpm

The direct bearing displacements are maintained at ~ 20 µm across the excitation frequency. The cross coupled bearing displacements are ~10 µm.

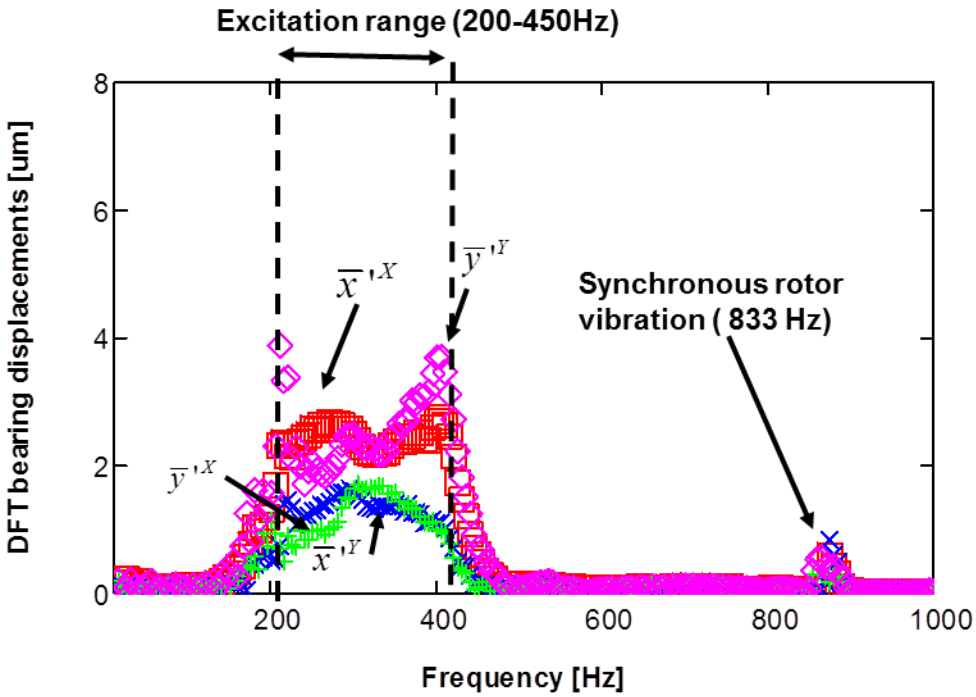

Figure E 2. Average DFT amplitude of bearing displacements versus frequency. Sine sweep 200-400Hz. Average of 10 excitations. Rotor speed ~ 50 krpm. Specific load ~ 14.3 kPa.

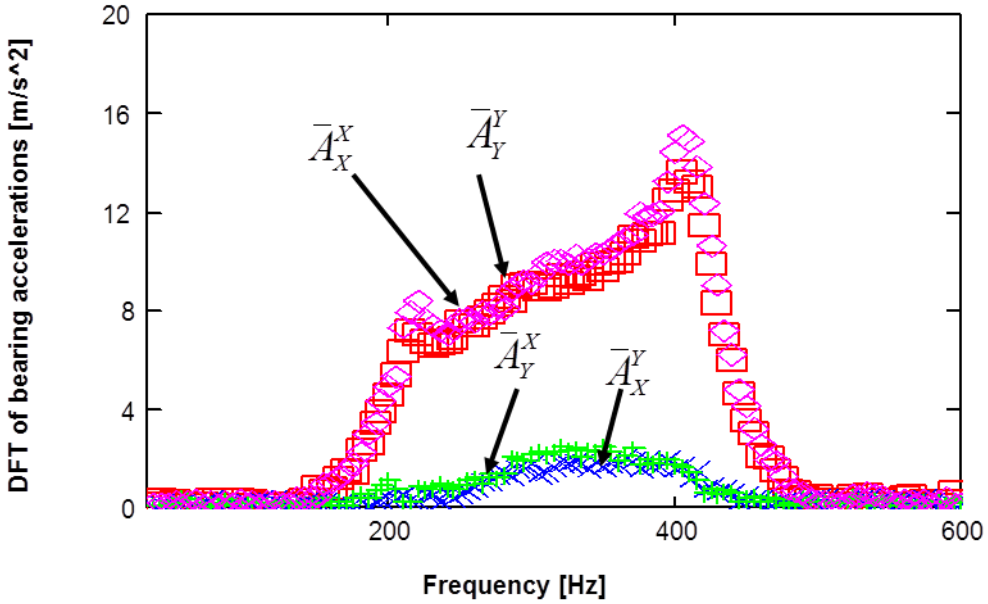

Figure E 3. Average DFT amplitude of bearing absolute accelerations versus frequency. Sine sweep 200-400Hz. Average of 10 excitations. Rotor speed ~ 50 krpm. Specific load of 14.3 kPa.

APPENDIX F

EXPANSION OF THE TEST SHAFT DUE TO THERMAL AND CENTRIFUGAL EFFECTS

As developed in Ref [35] and used in Ref. [36], the centrifugal expansion of the shaft (r_g) is

$$r_g = \frac{1}{E}\left[(1-\nu)R_o C_o - (1+\nu)\frac{1}{R_o}C_1 - \frac{(1-\nu^2)}{8}\rho\,\omega^2 R_o^3\right] \tag{13}$$

$$C_o = \frac{3+\nu}{8}\,\rho\,\omega^2\left(R_i^2+R_o^2\right) \text{ and } C_1 = -\frac{3+\nu}{8}\,\rho\,\omega^2 R_i^2 R_o^2$$

where E, ρ, ν, are the elastic modulus, density and Poison's ratio of the rotor, and ω is the rotation frequency in rad/s.

Thermal expansion of the rotor is assessed as

$$\Delta R = R_o \alpha\, \Delta T \tag{14}$$

where α is the linear coefficient of thermal expansion for AISI 4140 (listed in Table 4 on page 80), and the ΔT~30°C as experimentally observed. The ΔR~7 μm for the test shaft, subjected to a 30°C temperature rise.